NOVEL METAL ASSISTED ETCHING TECHNIQUE FOR ENHANCED LIGHT
MANAGEMENT IN BLACK CRYSTALLINE SI SOLAR CELLS

A THESIS SUBMITTED TO
THE GRADUATE SCHOOL OF NATURAL AND APPLIED SCIENCES
OF
MIDDLE EAST TECHNICAL UNIVERSITY

BY

FIRAT ES

IN PARTIAL FULFILLMENT OF THE REQUIREMENTS
FOR
THE DEGREE OF DOCTOR OF PHILOSOPHY
IN
MICRO AND NANOTECHNOLOGY

AUGUST 2016

Approval of the Thesis:

**NOVEL METAL ASSISTED ETCHING TECHNIQUE FOR ENHANCED
LIGHT MANAGEMENT IN BLACK CRYSTALLINE SI SOLAR CELLS**

submitted by **FIRAT ES** in partial fulfillment of the requirements for the degree of
**Doctor of Philosophy in Department of Micro and Nanotechnology, Middle East
Technical University** by,

Prof. Dr. Gülbin Dural Ünver
Dean, Graduate School of **Natural and Applied Sciences**

Assoc. Prof. Dr. Burcu Akata Kurç
Head of Department, **Micro and Nanotechnology**

Prof. Dr. Raşit Turan
Supervisor, **Department of Physics, METU**

Prof. Dr. Tayfun Akın
Coadvisor, **Department of Electrical and Electronics Engineering, METU**

Examining Committee Members:

Prof. Dr. Hasan Efeoğlu
Department of Electrical and Electronics Engineering, Atatürk Uni.

Prof. Dr. Raşit Turan
Department of Physics, METU

Prof. Dr. Canan Varlıklı
Department of Photonics, İzmir Institute of Technology

Assoc. Prof. Dr. Ali Çırpan
Dept. of Chemistry, METU

Assist. Prof. Dr. Ali Kemal Okyay
Department of Electrical and Electronics Engineering, Bilkent Uni.

Date: 23.08.2016

I hereby declare that all information in this document has been obtained and presented in accordance with academic rules and ethical conduct. I also declare that, as required by these rules and conduct, I have fully cited and referenced all material and results that are not original to this work.

Name, Last name: Fırat ES

Signature:

ABSTRACT

NOVEL METAL ASSISTED ETCHING TECHNIQUE FOR ENHANCED LIGHT
MANAGEMENT IN BLACK CRYSTALLINE SI SOLAR CELLS

ES, Fırat

Ph.D., Department of Micro and Nanotechnology

Supervisor: Prof. Dr. Raşit Turan

August 2016, 137 pages

Photovoltaic (PV) technology needs higher performance - lower cost materials and structures in order to catch the grid parity and become an everyday use power source. The most commonly used material in PV, crystalline silicon, suffers from low absorption due to its indirect band gap nature. In order to overcome this problem, several light trapping structures have been used that increase the path length of photons inside the absorbing body of the device. However, conventional light trapping schemes cannot be applicable to new device concepts based on thin crystalline or diamond cut wafers.

Metal assisted etching (MAE) is promising method to form micro and nano structures on the surface of the silicon wafer for optical management. As a top down method, it allows the control of the type and concentration of the dopants, material quality and crystal structure of the starting material. In addition, as a solution based method, it can be adapted to large scale industrial applications where nanoscale structuring can contribute to the development of high performing devices. A variety of structures

having desired geometry such as nanowires, nano-cones, micro-rods, etc., ranging from nanometer to micrometer sizes with random or periodic distribution can be obtained via MAE by adjusting process parameters comprised of initial geometry of catalytic metal species, acid concentration, oxidative concentration, and temperature, ambient light, etching duration, substrate resistivity and orientation.

In this study, MAE has been used to texture mono and multi crystalline silicon solar cells. Mono and multi crystalline Si solar cells with nano-wire texturing have been fabricated with Ag assisted electroless etching. After observation of poor efficiency despite very good optical performance, MAE with additional nitric acid (HNO$_3$) as an oxidative agent has been optimized to control surface structures and reflection. Applicability of this new chemical at various conditions that simulate industrial production environment was proven. Optimized recipe has been applied to mono and multi crystalline Si solar cells to prove the effectiveness of the method for both wafer types. In the end, together with necessary optimizations of cell production steps, enhancement of j$_{SC}$ and efficiency has been attained for both cases. This concludes that the new MAE method based on a new chemistry offers a promising alternative to conventional texturing methods for today's and future technology.

Keywords: crystalline silicon solar cells, metal assisted etching, black silicon, surface texturing, light trapping

ÖZ

SİYAH KRİSTAL Sİ GÜNEŞ GÖZELERİNDE GELİŞTİRİLMİŞ IŞIK YÖNETİMİ AMAÇLI YENİ BİR METAL DESTEKLİ AŞINDIRMA TEKNİĞİ

ES, Fırat

Tez Yöneticisi: Prof. Dr. Raşit Turan

Doktora, Mikro ve Nanoteknoloji Bölümü

Ağustos 2016, 137

Şebeke değerini yakalamak ve günlük kullanıma uygun bir güç kaynağı haline gelebilmek için, fotovoltaik (FV) teknolojisi, daha yüksek performanslı ve daha ucuz malzemelere ve yapılara ihtiyaç duymaktadır. FV'de en yaygın kullanılan malzeme olan kristal silisyum, dolaylı bant yapısı nedeniyle düşük ışık emilimi problemiyle karşılaşmaktadır. Bu problemi çözmek için, fotonların kristal içinde aldığı yolu artıran çeşitli "ışık hapsetme" yapıları kullanılmaktadır. Fakat yeni nesil ince ve elmas kesimli dilimlerde, geleneksel ışık hapsetme yöntemleri kullanılamamaktadır.
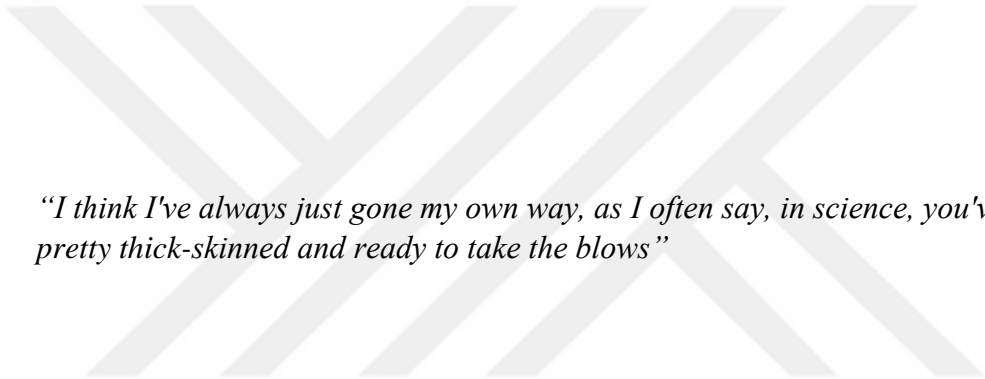
Metal destekli aşındırma (MDA), silisyum dilimlerde optik kontrol amaçlı mikro ve nano boyutlu yapılar oluşturmak için gelecek vaat eden bir yöntemdir. Yukardan aşağı bir yöntem olarak, katkılama miktarını ve tipini, malzeme kalitesini ve kristal yapısını, kontrol edilebilmesini olanaklı kılar. Bunula birlikte, çözelti temelli bir yöntem olduğu için, nano boyutta yapıların yüksek performanslı aygıtlar oluşturulasında

kullanılabileceği durumlarda, büyük ölçekli endüstriyel uygulamalara adapte edilebilir. MDA kullanarak ve başlangıç katalizör metal geometrisi, asit konsantrasyonu, oksitleyici konsantrasyonu, sıcaklık, ışık şiddeti, aşındırma süresi, alt taş direnci ve yönelimi gibi süreç parametrelerini ayarlayarak, nanometre' den mikro metre boyutlarına kadar değişen, nano-tel, nano-koni, mikro-teller vb. gibi farklı geometrideki yapılar oluşturulabilir.

Bu çalışmada, mono ve multi kristal silisyum güneş hücrelerinin yüzey yapılandırması için MDA yöntemi kullanılmıştır. Gümüş destekli aşındırma yöntemi ile mono ve multi kristal, nano-tel yapılandırmalı hücreler üretilmiştir. Yüksek optik performansa rağmen, düşük hücre verimleri elde edildiği için, kimyasal aşındırma yöntemi, yüzey yapılarını ve yansımayı kontrol etmek amacıyla nitrik asit (HNO_3) eklenerek optimize edilmiştir. Yöntemin farklı endüstriyel uygulamalara yatkınlığı test edilmiştir. Optimize edilmiş reçete, mono ve multi kristal Si güneş hücrelerine uygulanmıştır. Sonuç olarak, hücre üretiminde yapılan çeşitli optimizasyonlar ile birlikte, akım yoğunluğu ve verim değerlerinde artış gözlemlenmiştir. Böylece, çalışılan yöntemin, bugünün ve geleceğin FV teknolojisi için geleneksel yapılandırma işlemlerine bir alternatif olarak gelecek vaat ettiği gözlemlenmiştir.

Anahtar Kelimeler: Kristal silisyum güneş hücreleri, metal destekli aşındırma, siyah silisyum, yüzey yapılandırma, ışık hapsetme

"I think I've always just gone my own way, as I often say, in science, you've got to be pretty thick-skinned and ready to take the blows"

by *Barry Marshall*, who in July of 1984, drank a beaker of cloudy, brown liquid that was swimming with *Helicobacter Pylori* at once to prove that this bacterium is the cause of most peptic ulcers, rather than stress, spicy foods, and too much acid, bringing him the *Nobel Prize in Physiology or Medicine in 2005*.

ACKNOWLEDGMENTS

First of all, I would like to thank my advisor Prof. Dr. Raşit Turan for his support and guidance throughout my study. It has been a long and fruitful journey during my two years of M.Sc. and six years of Ph.D. studies with him. I have learnt and I'm still learning a lot from him not only about solar cells but also about all different aspects of professional life.

I would like to thank Dr. Mustafa Kulakcı first for giving the idea behind this thesis study and then for all his wholesome and blissful friendship for my years in GUNAM.

Next, I thank Prof. Dr. Tayfun Akın, Dr. Ali Çırpan and Dr. Ali Kemal Okyay for their guidance through this study. I would like to thank my co-authors for their support, and Sedat Canlı and Seçkin Öztürk for scanning electron microscopy imaging. Together with these, I would like to thank all GÜNAM family including all technical and administrative staff for their friendship and help for my studies.

Lastly, I would like to thank my family, especially my wife Selma for bearing me with all my troublesome mood throughout my thesis period.

TABLE OF CONTENTS

LIST OF TABLES

LIST OF FIGURES

CHAPTER 1

INTRODUCTION

'Be less curious about people and more curious about ideas.'

Marie Curie

1.1. Earth, energy and human

Energy has been defined in various ways for different disciplines. For a physicist, it is the conserved quantity for a system with a *'Lagrangian'* of time translational symmetry. For a chemist, it is a property of a substance that stems from its atomic or molecular structure that can generate or dissipate heat/light while reactions take place. For a biologist, it is the collection of chemical energies stored in ATP (adenosine triphosphate) for vital activities to continue. For an electrical engineer; it the capability of electric current for heating a resistive coil, for a chemical engineer; it is the required threshold for a reaction to start and for a mechanical engineer; it is the ability of a steam engine to compress a hydraulic cylinder. Despite different definitions and forms, all types of energy are actually convertible to each other by some means and the word itself originates from the Greek "enérgia" which was first used by Aristotle as a synonym for 'being at work'[1].

The two fundamental motives of living are survival and the transfer of the genes to next generations. However, human being as the most intelligent species of the world to our knowledge, reinforce the probability of its existence by extending the boundaries of the transfer from reproduction to culture and knowledge which

accumulate as a result of its collective activities. This way of living leads to a continuous demand to develop and to protect the civilization that himself set. Thus all of the activities dedicated to the survival of the human being from the very basic one i.e. need for food to maintain vital functions to very sophisticated ones e.g. a rocket fuel to send a satellite to the orbit for higher resolution imaging of enemy bases "in peace" require energy. Historical development of the daily energy consumption per capita is given in Figure 1.
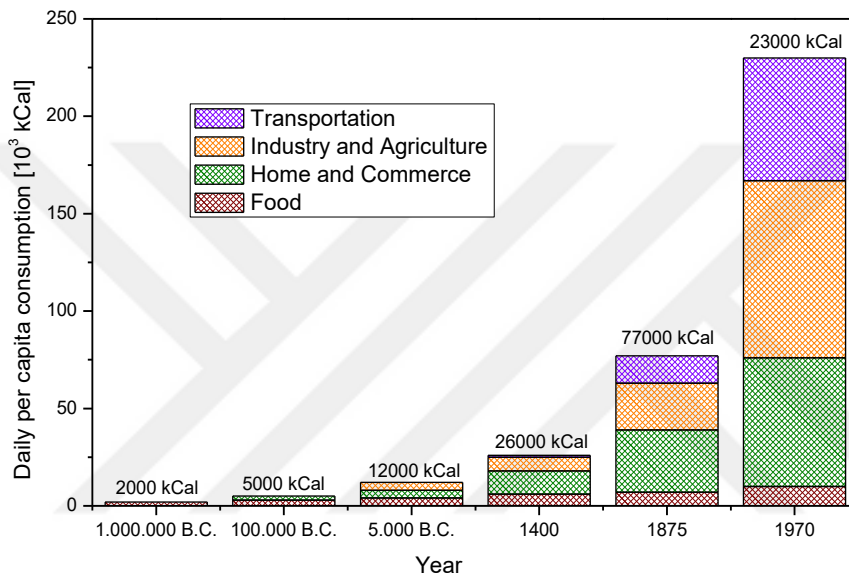
Figure 1 Daily per capita energy consumption history line[2].

It is clear that the consumption is increasing together with our population. Therefore, the total energy requirement is excessively getting higher. While the main source of energy had been biomass until the second half of the 19th century, carbon based coal, petroleum and natural gas have become dominant since then and variety has increased with the addition of nuclear and new renewables (other than biomass and water mills) after 1950's. However, this substantial dependency on extracted fossil fuels brings along some risks about the discontinuity of the supply due to scarcity of depletable resources; environmental safety and health and ultimately sustainability of the continuous development that human being dreams of. From the environmental perspective which is officially articulated in international documents, the domination

2

of carbon based energy sources has caused substantial emission of carbon compounds to the atmosphere which results in greenhouse heating (Figure 2). Although the direct and primary effects of the climate change on human being are cared about more, the indirect effects through the ecological change may be much more devastating.
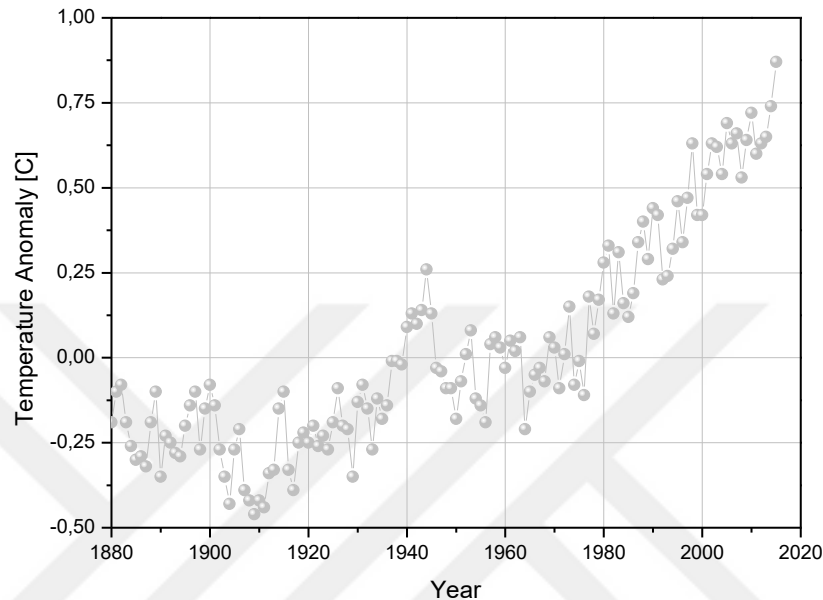
Figure 2 Global change in surface temperature for the last century[3].

Figure 2 shows that due to the increasing trend after 1960's, 1°C increase in global temperature till 2020 is expected. The solubility of oxygen decreases in water with increasing temperatures. As the oxygen levels go down, the population of the aerobic species in the oceans start to diminish along with 'anoxia'[4]. Subsequently, decomposition of the dead species results in further carbon and sulfide based gas emission which then accelerates the termination of the aerobic species as an avalanche process. Consequently, this may result in global extinction events such as 'Permian-Triassic; through which 96% of marine species, 70% of earth plants and 57% of insect families were extinct.

As a result, with the increase in need for energy and supplying of this energy by means of dirty sources, the global warming danger seems to be faced in the near future. One way of responding to this increasing demand without using the dirty sources is

harvesting solar energy. As the amount of energy reaching a square meter of Earth is approximately 1000 W/m^2, the daily energy need of 1 person can be supplied from a 3.5m^2 area if 30% of the solar energy was converted. Alternatively, 30% of the total energy reaching the 1/8th of the Earth's surface can supply the energy required for a population of 2x10^{13}, 3000 times more than today's population.

1.2. Photovoltaics

In 1839, French physicist Edmund Becquerel on his famous article (Figure 3), referred to his experiment "*Action of Radiation on the Metal Blades*" with the following conclusion; *"In summary this dissertation reveals the following facts. 1. When rays that accompany the most refrangible rays of sunlight are encountering with metal blades immersed in a liquid, such action results in electrical effects which cannot be attributed to a heat source"* [5].

MÉMOIRES LUS.

Mémoire sur les effets électriques produits sous l'influence des rayons solaires; par M. Edmond Becquerel.

§ 1re. *Action de la radiation sur les lames métalliques.*

« Dans le dernier Mémoire que j'ai eu l'honneur de présenter à l'Académie, dans sa séance du lundi 29 juillet 1839, je me suis attaché à mettre en évidence, à l'aide des courants électriques, les réactions chimiques qui ont lieu au contact de deux liquides, sous l'influence de la lumière solaire. Le procédé que j'ai employé nécessitait l'emploi de deux lames de platine, en relation avec les deux extrémités du fil d'un multiplicateur très sensible et qui plongeaient chacune dans une des dissolutions superposées. Or comme ces deux lames éprouvaient elles-mêmes les effets de la radiation, il a dû en résulter des phénomènes composés, dont je vais m'occuper dans ce nouveau Mémoire. On sera à même ensuite de faire la part de chacun des effets produits.

Figure 3 An image from E. Becquerel's original article 'Dissertation on electrical effects produced under the influence of sunlight'[5].

This, being the first known observation of PV electricity generation, comes more than 2500 years after the use of solar energy as a tool for lighting fires by human beings via concentrating lenses. Soon after, in 1873, Willoughby Smith, an English technician,

realized that the electrical conductivity of selenium bars would change under the influence of solar radiation, being the first one observing photoconductivity [6]. Later on, two additional studies on Se verified the PV effect consecutively [7,8]. However it was not until 1954, when the first silicon PV cell with a p-n junction of 6% efficiency was fabricated at Bell laboratories [9]. Until then, scientists and engineers have managed to fabricate solar cells that can convert up to 46%[1] of solar energy into electricity via employing differentiated techniques [10]. Timeline for solar cell efficiency development according to the highest efficiency is given in Figure 4[11][12]. If the linear trend is followed, 42% efficiency for one sun illumination can be expected by the year 2020.
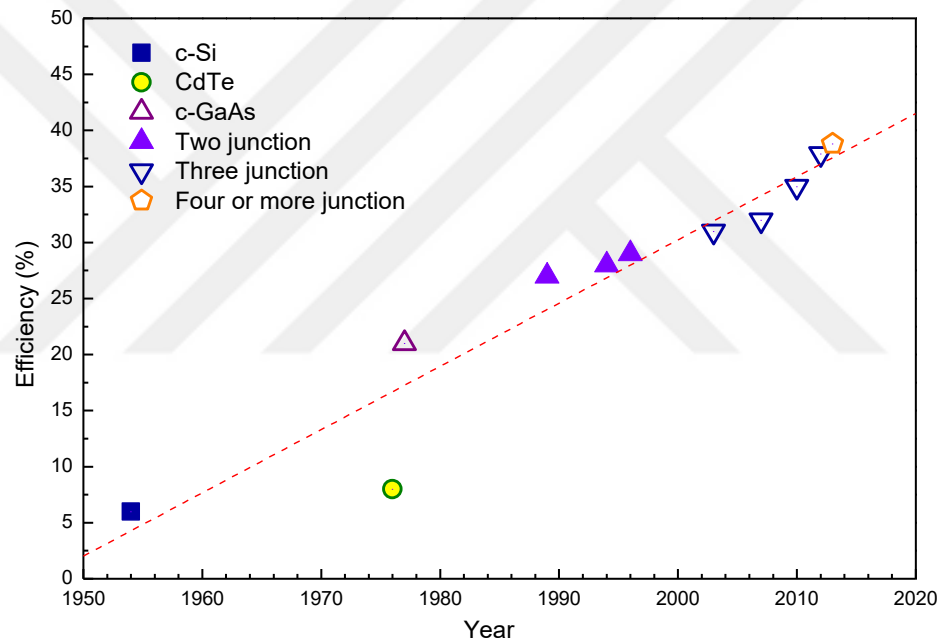
Figure 4 Timeline for non-concentrated PV efficiency development adapted from NREL best research cell efficiencies graph.

---

[1] Including concentrated illumination

On the other hand, commercially available PV modules' efficiencies range from 8 to 23%, while for lab type or on cell base, range is wider; from 8 to 39%. Figure 5 shows the historical development trend for the efficiency of PV modules[10,13–58].
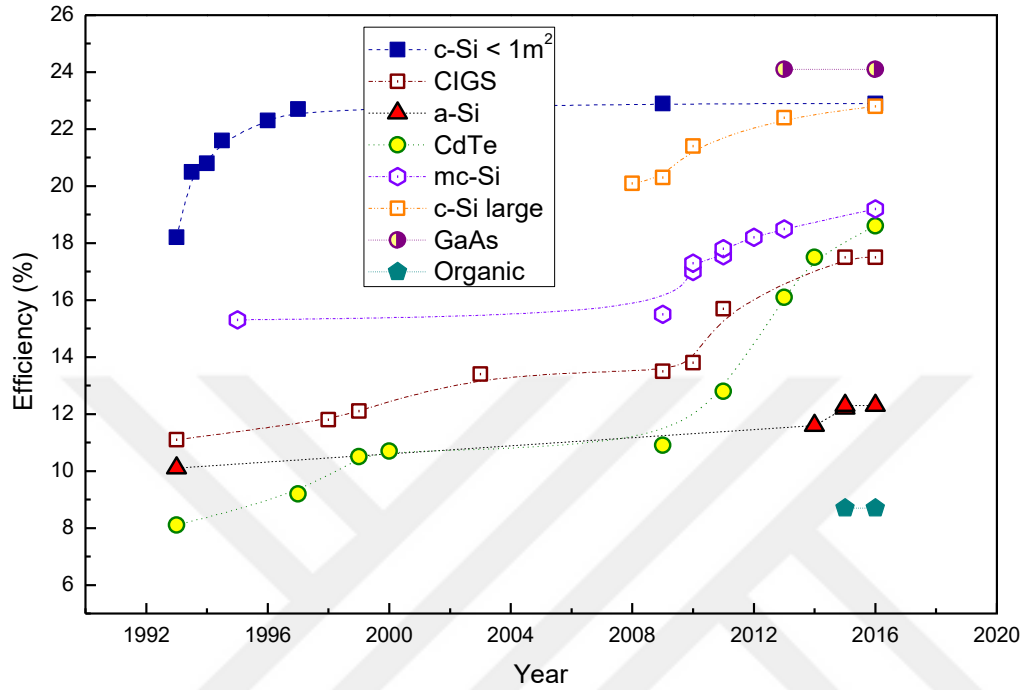
Figure 5 Timeline for commercially available PV module efficiencies.

It is observed that c-Si reaches a plateau around 23% while large area c-Si (larger area modules) catches up the same value in less than 10 years. Meanwhile, mc-Si follows a similar increasing trend which basically depends on the improvements in the quality of the material that has been enabled by means of high performance mc wafer growth techniques[59]. It is also worth noting that after the year 2009, a non-negligible increase in the efficiency of thin film devices has been recorded. On the other hand, Table 1 shows the highest efficiency modules available in the market for each basic technology today[10]. Ranking in the table depends on the maximum power output of the modules which highlights the module size as a performance parameter as well.

6

Table 1 Commercially available modules with highest efficiencies

Technology	Efficiency (%)	Area (m^2)	P$_{MAX}$ (Watt)	Company /Institute
c-Si	22,8	1,57	358	SunPower
mc-Si	19,2	1,51	290	Trina Solar
a-Si/nc-Si tandem	12,3	1,43	176	TEL Solar
CdTe (thin Film)	18,6	0,70	131	First Solar
GaAs (thin Film)	24,1	0,09	21	Alta Devices
CIGS	17,5	0,08	14	Solar Frontier
Organic	8,7	0,08	7	Toshiba

As seen from the tables and figures above, today's PV market is comprised of a variety of technologies which make use of a large portion of periodic table; elementally or in compound forms, while early devices were fabricated using only a few number of elements such as Se, Cu, Pt (Figure 6).

Figure 6 Periodic table of elements. Colored elements are used directly in the solar cell structure by PV industry and/or research labs.

1.3. Crystalline Silicon PV

The diversity in materials enabled improvements in optical and electrical properties which then led to the variety of efficiencies in final devices. C-Si dominates the PV market today with a share of 90% [60]. The reason for this domination can be

explained with its ability to form a stable oxide which makes it desirable for semiconductor processing as well as being a non-toxic abundant material by far. Further advantage of c-Si is high minority carrier lifetimes which allow high efficiencies to be achieved with this material[61].

Many efforts have been focused on increasing the efficiency of c-Si cells while keeping the production and material costs as low as possible. Concepts for increasing the efficiency include 'Selective Emitter (SE)', 'Passivated Emitter and Rear Cells (PERC)', 'Passivated Emitter Rear Locally Diffused Cells (PERL)', 'Passivated Emitter Rear Totally Diffused Cells (PERT)' and, 'Interdigitated Back Contact Cells (IBC)'[62]. These designs aim higher efficiencies with improved passivation, doping and metallization schemes through advanced production techniques. Therefore, since the increase in the efficiency reflects to the production costs, a decrease in cost per watt-peak is not an easy task to be attained. The cross sectional structure of state of the art c-Si PV devices with the brief descriptions about their advantages and dis – advantages are given below. All schematics are drawn for p type bases while n type counterparts are also producible in case of high efficiency requirements.

1.3.1. Full Area Back Surface Field Cells

Full area back surface field p type solar cells, called as Al:BSF cells, constitutes the major part of the c-Si PV market today. As obvious from the cross sectional structure, it has a homogeneously doped emitter and back surface field; a passivation layer on top of the emitter which also acts as an anti-reflective coating and front/back metallization (Figure 7). The homogeneous doping of emitter and BSF is its main technological advantage arising from process simplicity. On the other hand, the requirement of low resistance Si-metal contacts entails a high doping concentration in the emitter which results in high front surface recombination losses. In addition, full area back contacts cause high back surface recombination velocities. As a result, the device has an easy to fabricate structure that suffers from high surface recombination losses. Same structure with n type base is also produced where emitter is p doped and BSF is formed by n doping. However, the simplicity is somewhat sacrificed since n

8

type base requires single side diffusion on the back side which is not necessary for its p base counterpart where BSF is spontaneously formed by liquid phase epitaxy of Al on Si which leads to p+ doping.
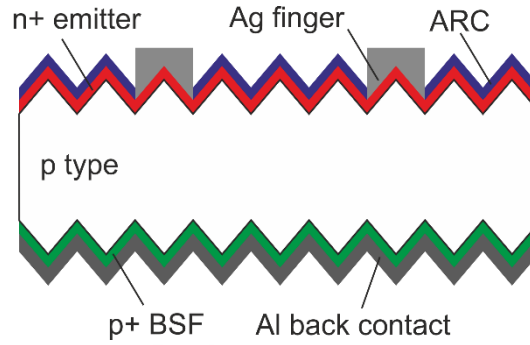
Figure 7 Full area back surface field solar cell structure

1.3.2. Selective Emitter Cells

In order to prevent high recombination in the emitter region while keeping low contact resistance, an inhomogeneous doping of the emitter is used for which the regions under the contacts are highly doped while the rest of the emitter is lowly doped (Figure 8). Though the cells give higher blue response, selective doping of the emitter is a technological problem in terms of production complexity when compared to homogeneous emitter cells.
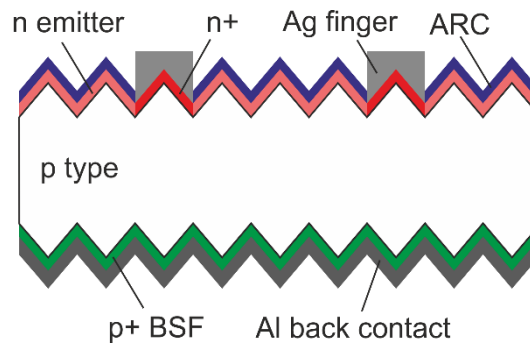
Figure 8 Selective emitter solar cell structure

9

1.3.3. Passivated Emitter Rear Cells (PERC)

In order to further decrease the recombination losses, in this technology, back surface of the cells is passivated (Figure 9) by SiOx/AlOx-HfOx/SiNx stacks. However, since the passivation maintained by this insulator stack prevents current flow, local openings are formed on the dielectric film to enable contacts to the silicon surface. The competition between FF and Voc due to resistive losses and recombination losses respectively is optimized by providing a certain metal fraction on the back surface. Today's PERC cells have efficiencies as much as 22.1% for p type material[63] with an increasing market share due to the developments in production technology such as single side etching and laser structuring.
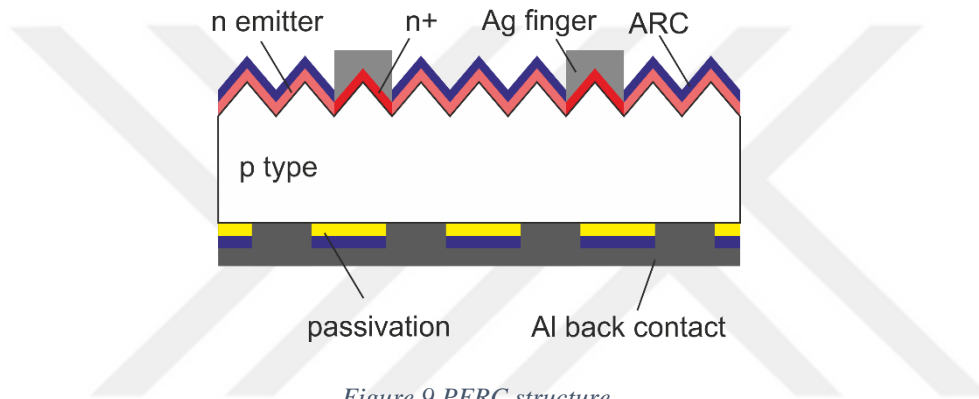
Figure 9 PERC structure

1.3.4. Passivated Emitter Rear Locally Diffused Cell

Although the PERC cell has a good back surface passivation, the contacting between the metal and the base material causes high resistive losses since the doping level of the base is usually kept low. To solve this problem, the back surface of the cell is locally doped with high concentrations through the dielectric openings. Thus the metal-Si contact attains a lower resistance and the local doping acts as an electrical mirror to keep minority carriers away from the surface (Figure 11). Efficiencies as high as 25% have been reported for this kind of structure[63].
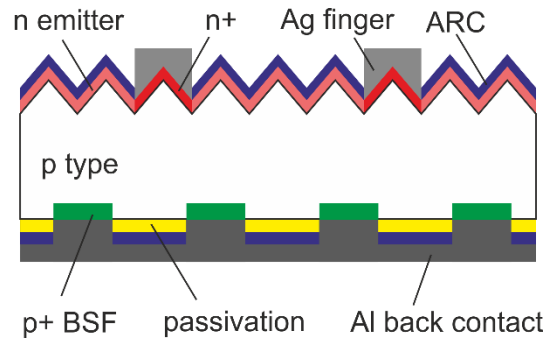
Figure 10 PERL structure

1.3.5. Passivated Emitter Rear Totally Diffused Cell – Bifacial Cells

When the back surface of the cells is diffused totally (Figure 11), the lateral conductivity will be enhanced that gives a chance to increase the distance between local back contacts with efficiencies as high as 22.5% [63]. PERT structure allows the possibility of having bifacial structure since high pitch fingers can be formed on the back side which will let diffuse illumination through (Figure 12). The bifacial structure can increase the energy production up to 20% by special positioning of modules in the field[64].
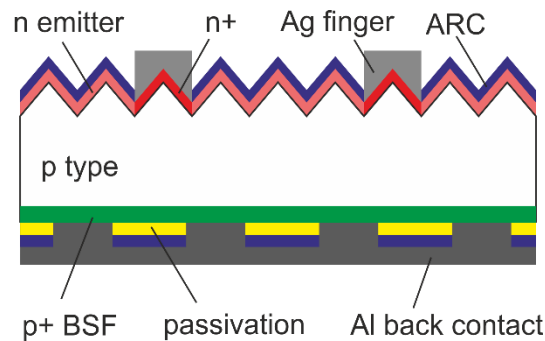
Figure 11 PERT structure
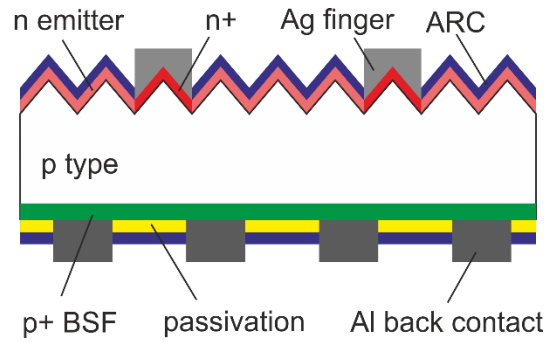
Figure 12 Bifacial PERT structure

1.3.6. Interdigitated Back Contact Solar Cells (IBC)

In order to get rid of the shadowing losses due to front side metallization, all contacts and therefore the p-n junction are placed to the rear side of the cell. This process not only helps to get higher current from the cell but also allows very large cross sectional area metallization which reduces series resistance losses (Figure 13). Despite these advantages, requirement for very high quality surface passivation, high bulk lifetimes and complicated back surface structuring are the technological handicaps of this structure. Efficiencies as high as 25.2% have been reported for n type of c-Si IBC solar cells[63].
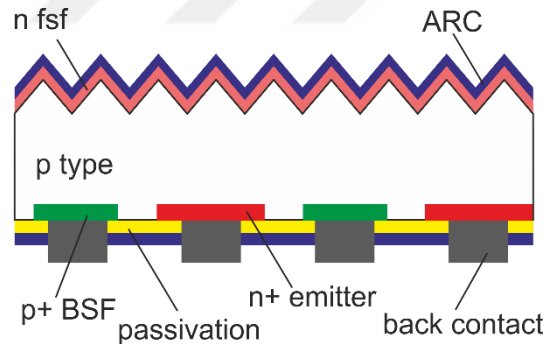
Figure 13 IBC structure

1.4. Low Cost Routes in Crystalline Si PV Technology

Another approach is to decrease the material cost while keeping efficiency in reasonable levels. 'Multi-Crystalline Silicon Solar Cell (mc-Si)', 'Metallurgical Grade Silicon Solar Cell (MGS)' and 'Quasi Single Crystal Silicon Solar cell (QSC)' concepts takes the advantage of reducing cost of wafers that constitutes the 50% of the

module price[65–67]. However, as the material quality decreases collection efficiency is reduced with these new materials. Therefore a well optimized production scheme and material choice is crucial for high-efficiency low-cost solar cell production.

An option for decreasing the material usage while maintaining high efficiencies is using very thin crystalline silicon wafers for solar cell production[61,66,68–72]. Efficiencies of 20.1% for 43μm thick crystalline silicon cells have been reported while for 1μm thick cells, efficiencies are found to be less than 5% [56,68]. Very thin crystalline silicon holds the advantage of permitting low minority carrier lifetimes and low material usage but suffers from low absorption due to indirect band gap nature of c-Si.

In terms of optical properties, absorption of photons is the most crucial step of PV energy conversion. For absorption to occur, incident photons should have energies greater than or equal to the band gap of the semiconductor used as the active material. The energy of the photon is transferred to an electron in valance band and this electron moves to conduction band to maintain the conservation of energy. For the case of c-Si, a band gap energy of 1.12 eV is present so photons with wavelengths shorter than 1100nm will be absorbed by the material. However, since Si is an indirect band gap material, absorption process should also conserve momentum. Conservation of momentum in crystals requires absorption or emission of phonons. Therefore, for a transition from valance to conduction band, both energy and momentum conservation, in other words both photon and phonon absorption-emission processes should occur simultaneously. Since each emission-absorption process takes place with some probability, having photon and phonon absorption-emission processes simultaneously will reduce the probabilities of these processes. This multiplication of two probabilities makes absorption processes for indirect band gap smaller than that for direct band gap material. Figure 14 shows some common PV materials' absorption coefficients and a calculation based on minimum thickness needed to absorb 99% of photons at a wavelength of 600nm.
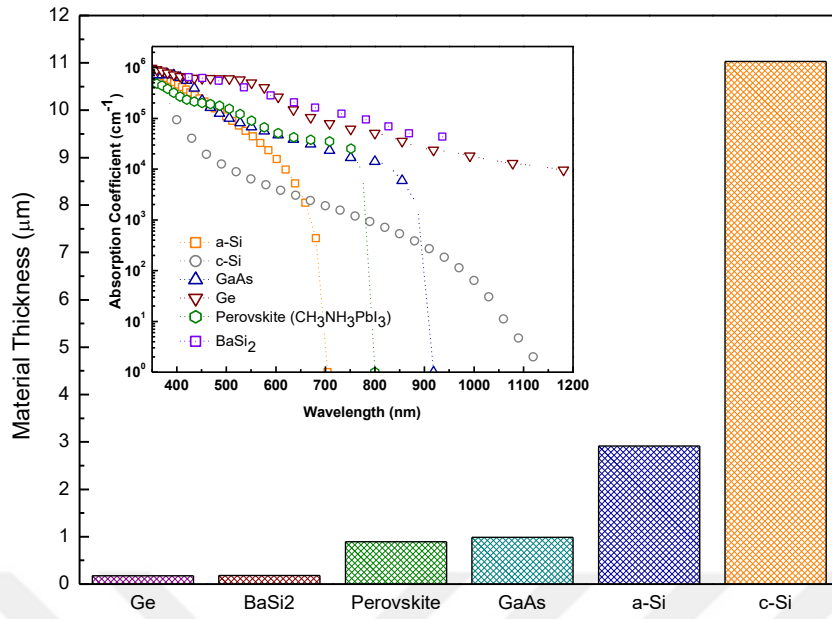
Figure 14 A calculation of material thickness needed to absorb 99% of the photons with a wavelength of 600nm for different materials. Inset is the absorption coefficients of these PV materials taken from the literature [73–77].

It is clear that c-Si has the lowest absorption and requires 50 times thicker material in order to absorb the same amount of light with Ge at 600nm. On the other hand, for the wavelengths close to each material's band edge, these values change enormously. For example, a Ge wafer of 200μm will be enough to absorb 99% of the wavelength of 1900nm while a Si slab of 10mm will be required for the same amount of absorption of 1100nm photons. Therefore, for the absorption of the entire spectrum, one should use of a very thick Si wafer. Absorption of each wavelength will result in generation of electron-hole pairs and a generation profile as shown in Figure 15 will be present for a 10mm thick Si wafer.
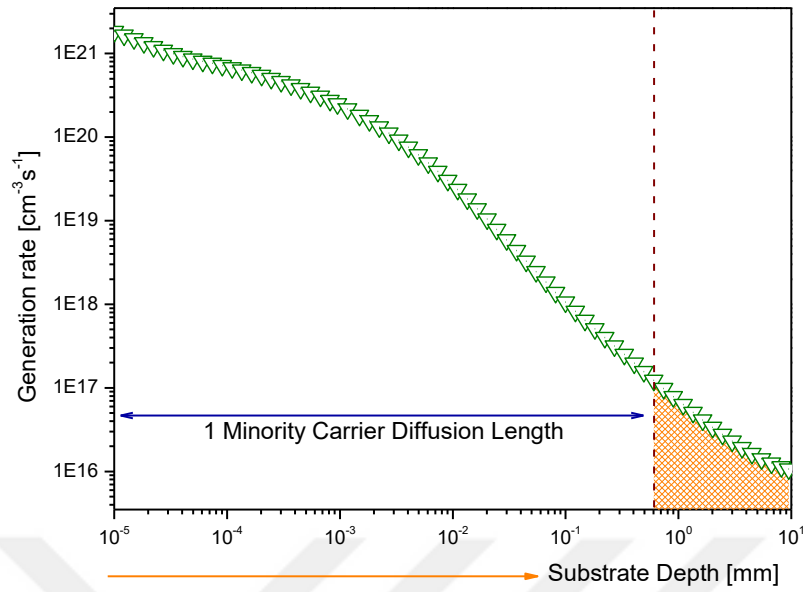
Figure 15 Generation rate for a 10mm thick c-Si wafer under 1 sun illumination with polished pristine surface.

It is observed that, the problem of absorption would be solved with the use of a thicker wafer for low absorption materials. On the other hand, c-Si PV devices are composed of very shallow p-n junctions located at a depth of approximately 300nm from the surface. This brings along the problem of diffusion length since for most of the c-Si devices, the diffusion length of minority carriers is of the order of several hundreds of micrometers. This implies that some portion of the spectrum that is absorbed more than one minority carrier diffusion length away from the junction will not contribute to current and will be lost as recombination (Figure 15 – orange shaded area and Figure 16).
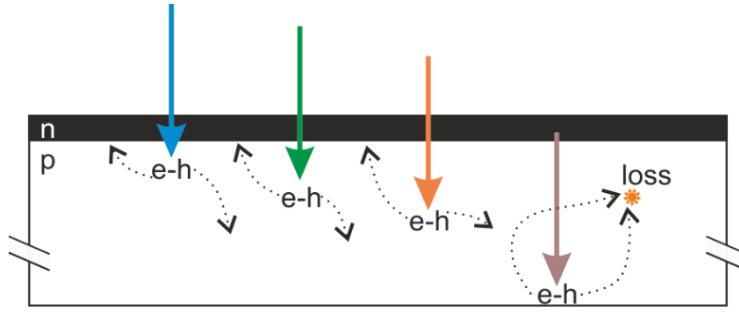
Figure 16 A wafer thick enough to absorb all wavelengths while some of the generated carriers are recombined since the generation takes place more than one minority carrier diffusion length away from the junction

As a second issue, use of thick Si wafers will result in expensive devices due to large amount of material consumption. For example, a 10mm silicon wafer of 156mm x 156mm will weight approximately 500gr and cost more than 50$ since a very high quality wafer will be needed for very long diffusion lengths[78]. On the other hand, present c-Si production mainstream is using 180µm wafers and the prediction for 2026 is down to 140µm for as cut wafer thickness in mass production(Figure 17)[79] The cost of one single monocrystalline wafer is about 1$ which constitutes about %55 of a solar cells. So, it is certainly favorable to further reduce the Si wafer thickness for cost reduction. However, the problem of low absorption should be solved by proper light trapping approaches. We address various aspect of light trapping throughout this thesis

16
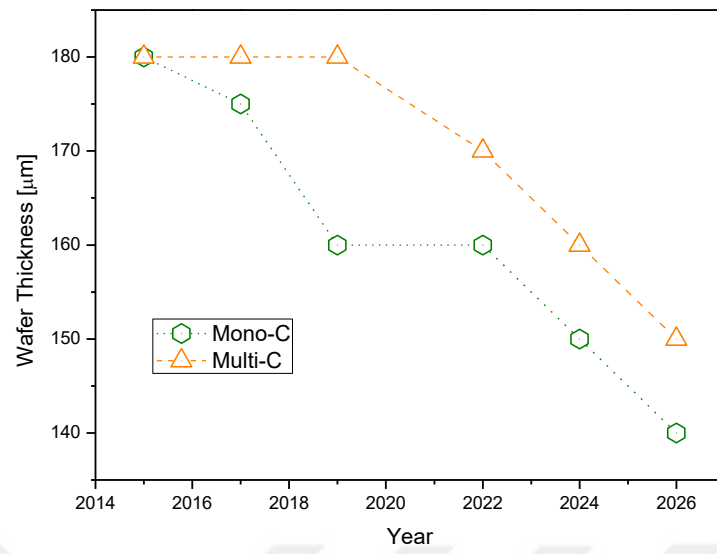
Figure 17 ITRPV Roadmap for industrial as cut wafer thickness

CHAPTER 2

LIGHT TRAPPING, TEXTURING AND METAL ASSISTED ETCHING

2.1. Light Trapping

It is clear that a c-Si wafer with a thickness of the order of hundred micrometers will suffer from transmission losses (Figure 14 and Figure 18). In the end, for c-Si, a competition between absorption and diffusion of minority carriers occurs.
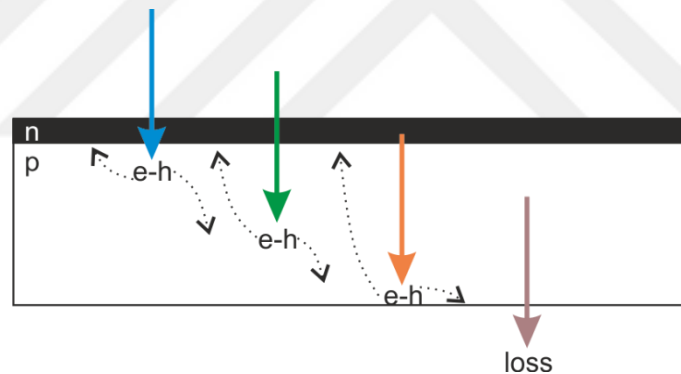
Figure 18 A wafer thinner than minority carrier diffusion length. All generated carriers may be collected while some portion of the spectrum is lost.

In order to solve the problems arising from insufficient absorption and limited diffusion length, increasing the optical path of the photon inside the semiconductor, "light trapping", is preferred[80–82]. With light trapping, the incoming photon "sees" the material thicker than it is in reality while created e-h pairs can travel along the semiconductor without recombination till separated by the junction. In 1982, Eli Yablonovitch and George D. Cody calculated the intensity enhancement factor limit

for semiconductor sheets using statistical mechanical approaches as '$4n^2$', called 'Yablonovitch Limit' where n is the refractive index of the semiconductor[83]. For c-Si, values of intensity enhancement with respect to wavelength is given in Figure 19. It is clear that for wavelengths close to the band gap, the enhancement is close to 50 which implies that instead of using a 10mm slab Si without light trapping, use of 200µm thick wafer with perfect light trapping will give the same optical performance.
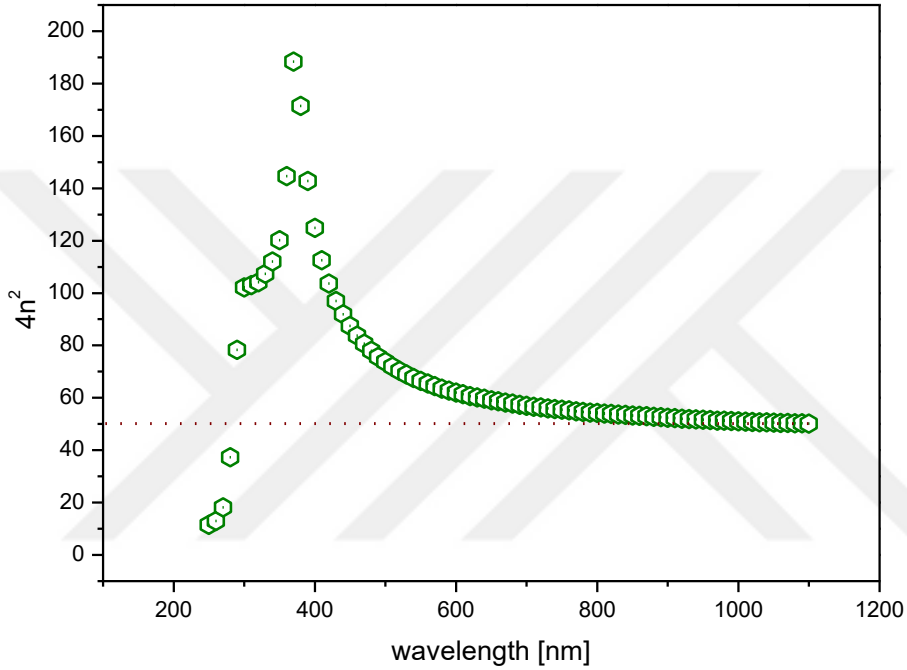
Figure 19 Intensity enhancement for c-Si at each wavelength according $4n^2$ limit

The effect of surface structuring on light trapping can be understood by the schematics shown in Figure 20. With proper surface structures providing good angular direction, the path length of a ray can be increased to many times of the thickness of the wafer leading to significant enhancement the absorption in the wafer. For example, the total weighed average reflection from a pyramid textured Si wafer is ~25% smaller than shiny wafer.

20
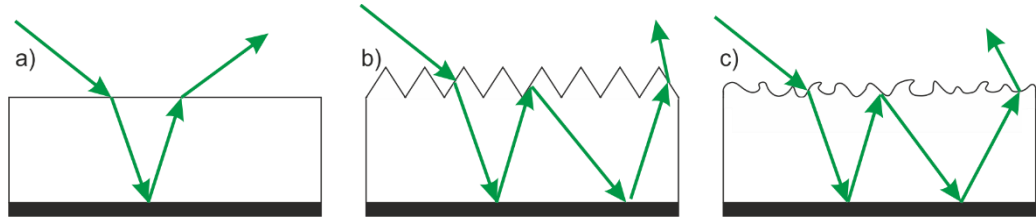
Figure 20 Effect of surface texture on optical path of the incident photon for a) flat surface, b) pyramid textured surface and c) isotropic etched surface

2.2. Texturing Methods

To enhance absorption, several light trapping structures and anti-reflective coatings have been developed[81,84]. Some common techniques for texturing will be discussed below.

2.2.1. Mono-c Si Texturing

For mono-c silicon, commonly alkaline etching is used as the texturing method [85]. This process takes the advantage of anisotropic etching property of KOH along (100) and (111) crystallographic planes. Etch rate of KOH for (100) plane can be as much as 600 times higher than that of (111) direction with the following reaction (eqn. 1)[86].

$$Si + 2KOH + H_2O \rightarrow K_2SiO_3 + H_2 \qquad \textit{eqn. 1}$$
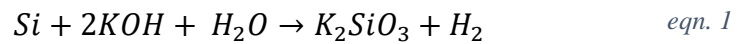
The reaction results in a textured surface of micro pyramids with (111) oriented faces which can be considered as etch stop for KOH etching (Figure 21).
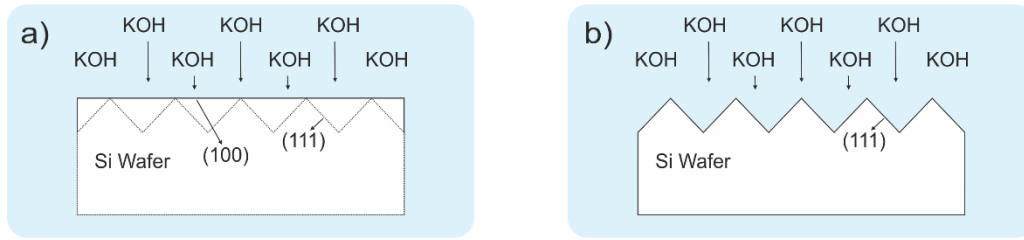
Figure 21 a) (100) oriented wafer in KOH solution, (b) after process only (111) planes are left on the surface creating pyramidal texture.

SEM image of typical pyramids formed by alkaline texturing is given as example in Figure 22.
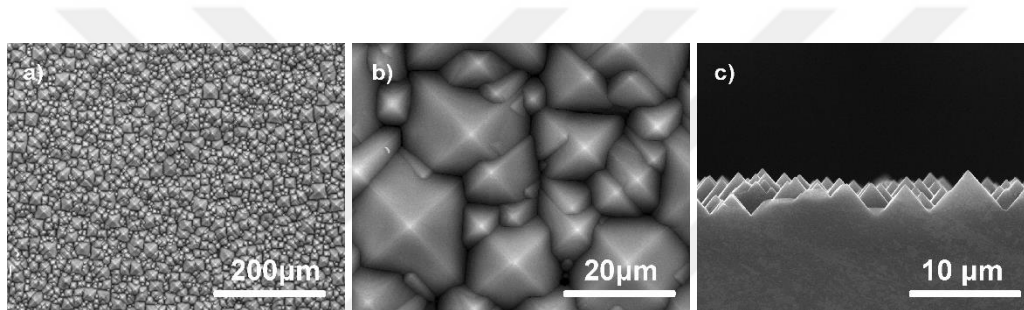
Figure 22 a), b) pyramids on the surface of silicon with different magnifications, c) another sample with cross section image of micro pyramid texture

2.2.2. Multi-c texturing

For multi-c silicon, since there are several grains with different crystal orientations on the surface, anisotropic alkaline texturing is not applicable. Instead, HF, HNO₃, H₂O₂ bearing isotropic stain etching solutions are used to form random texture on the surface[87]. During this process, HNO₃ is used for oxidation of Si and HF is used for etching of SiO₂ (eqn. 2).

$$Si + HNO_3 + 6HF \rightarrow H_2SiF_6 + HNO_3H_2O + H_2 \qquad \text{\textit{eqn. 2}}$$
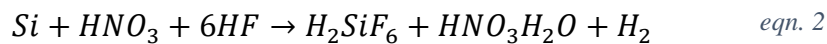
Example SEM images for multi-c isotropic texturing are given in Figure 23.
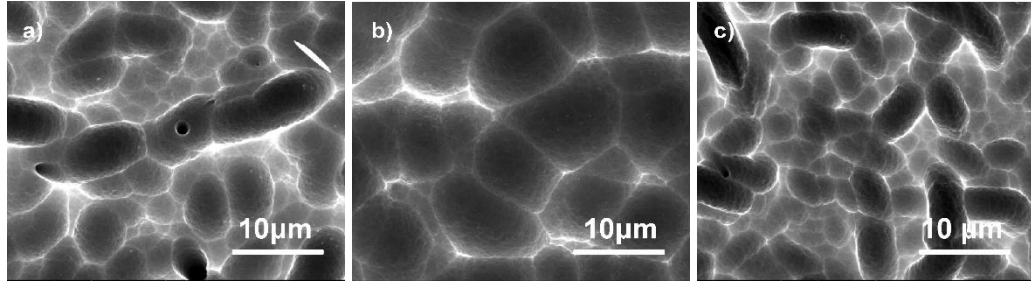
Figure 23 SEM images of variety of isotropic textured multi-c Si wafers

2.2.3. Other Texturing Methods

In addition to the previous standard methods, new approaches has been also developed for texturing of c-Si wafers. The main reasons for the requirement of alternative texturing processes with the developed process are given below:

Better optical performance: Even though the mono and multi-c silicon texturing is possible with previous methods, an antireflective coating must be utilized for both cases to improve optical properties of the surface. Commonly PECVD SiN is used as an ARC but new concepts such as forming nano-structures on the surface. Solar cells with nano-structure texture on front and back surface have been reported[88–92]. The sub-wavelength nanostructures formed on the surface act as a medium with a graded refractive index that suppresses Fresnel reflections[93–95]. A decreased reflection will result in an increased short circuit current density and increased conversion efficiency. These types of cells with virtually no reflection from the surface are called 'Black Silicon' solar cells[96–99]. However, high surface recombination as a result of increased surface area is the main drawback of nano-textured solar cells[97]. Improved passivation schemes lead to efficiencies of 18.2% for black silicon solar cells[94,100,101].

Applicability to thin wafers: For thin crystalline silicon cells, pyramid and acidic texturing methods are not applicable due to mechanical reasons since the device thickness is close to the minimum feature sizes. In the end, nano-texturing of the surface is a solution that will result in very low reflection from the surface without

significant material loss. Nano-structures for light trapping can be formed on the surface in various ways such as 'Nano-sphere Array Lithography', 'Reactive Ion Etching (RIE)', 'Chemical Vapor Deposition (CVD)', 'Vapor-Liquid-Solid (VLS) Growth Method' and 'Metal Assisted Etching (MAE)'[89,90,102–104]. Alternatively, plasmonic scattering and 3D photonic crystal enhanced light trapping methods are applicable to thin wafers since there is no loss of bulk or surface material[81][93,105,106].

Crystallographic orientation independence: Even though for mono-c, surface orientation is constant, for multi-c, new methods that give rise to low reflection from the surface have been investigated. Among these methods, dry texturing, laser texturing, plasma texturing are novel approaches towards high efficiency but application to large area and mass production are important issues to be addressed before these techniques can be put into the production lines [82,107–110].

2.3. Metal Assisted Etching

Among the different fabrication methods, MAE is a promising approach that can be adapted to mono, multi and thin crystalline silicon solar cells. It is a low cost, highly flexible technique to fabricate various structures on Si ranging from nanometers to micrometers in size[111–114]. As a top down approach, it allows the control of the nano-structure doping and crystal direction which is not possible with other methods such as VLS. As a wet process, it is adaptable to high throughput hence enables mass production. Also control of surface features such as nano-wires or nano-holes are possible by changing etching parameters and/or combining with other micro-machining techniques like photo-lithography, interference lithography, nano-sphere lithography etc. [115–129].

24

Several studies has been reported on texturing of crystalline silicon solar cells by MAE[91–93,101,103,104,130–134]. Mostly, vertically aligned silicon nanowires fabricated by MAE have been applied to solar cells due to their interesting optical properties[98,117,135,136]. The nanowires on the surface act like a medium with gradually decreasing refractive index from the surface which results in a perfect index matching and therefore a very low reflection from the surface[88,93,95]. However, as discussed below, with very large surface area, solar cells with nanowires suffer from extensive charge recombination on the surface.

2.3.1. Mechanism

In MAE, silicon which is partly covered by a thin layer of metal is subjected to an etchant solution of HF and H_2O_2. Regions of silicon in contact with the metal are oxidized faster and resultant SiO_2 is etched by HF to form cavities through which the metal sinks[114]. There are several reaction mechanisms suggested to explain the chemistry of the process[114,115,123,137,138]. These reactions are given below [139];

Cathode Reaction: reduction of H_2O_2 which occurs faster around the metal;

$$H_2O_2 + 2H^+ \rightarrow 2H_2O + 2h^+ \qquad \text{\textit{eqn. 3}}$$
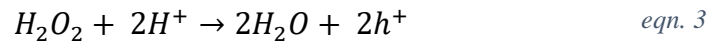
Anode reaction: dissolution of Si and SiO_2 by HF;

$$2Si + 12HF + 6h^+ \rightarrow 2H_2SiF_6 + 6H^+ + H_2 \qquad \text{\textit{eqn. 4}}$$

$$SiO_2 + 6HF \rightarrow H_2SiF_6 + H_2O \qquad \text{\textit{eqn. 5}}$$
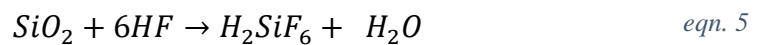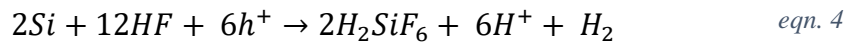
For 'Metal Assisted Electroless Etching' a metal salt such as AgNO₃ is used in a solution containing HF to deposit the metal and etch underlying silicon by MAE at the same time[118,119,140,141]. The anode reactions are similar while for cathode, metal ions become main hole sources for silicon oxidation if there are no additional oxidants:

$$Ag^+ \rightarrow Ag(s) + h^+ \qquad \text{eqn. 6}$$

This reaction leads to solid Ag dendrite formation on the surface. The nucleation of the solid Ag is controlled by changing solution parameters which result in various types of nanowire formation on the surface[117]. Full reaction mechanism is schematically shown in Figure 24.
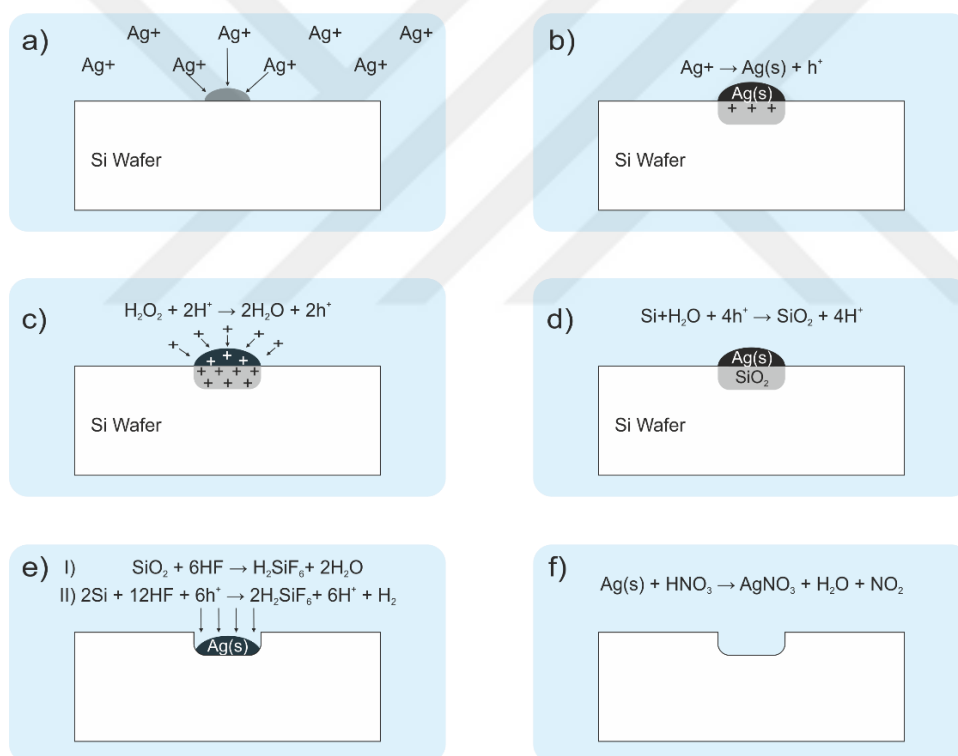
Figure 24 Symbolic drawing of the MAE process. a) wafer is immersed into the MAE solution, b) Ag nucleates on the surface of the surface by giving a hole to the Silicon, c) hydrogen peroxide is reduced in the solution which also adds extra hole injection to the Si, d) silicon is oxidized due to extra holes injected, HF etches both Si and oxide underneath the metal nano-particle, f) when the wafer is cleaned by nitric acid, the resulting etching is observed.

2.3.2. Transport of the chemicals

For transport of etchant to the interface two mechanisms are suggested [114]. First one is the transport of the chemical from the edges to the whole metal-Si interface. Of course this holds for small sized metal particles where lateral travel of the etchant is possible. The other one is Si diffusion through the metal into the metal surface where dissolution occurs. This model explains the etching behavior for metal structures with very low aspect ratio for which the MAE process still occurs. The schematic view for both models are given in Figure 25.
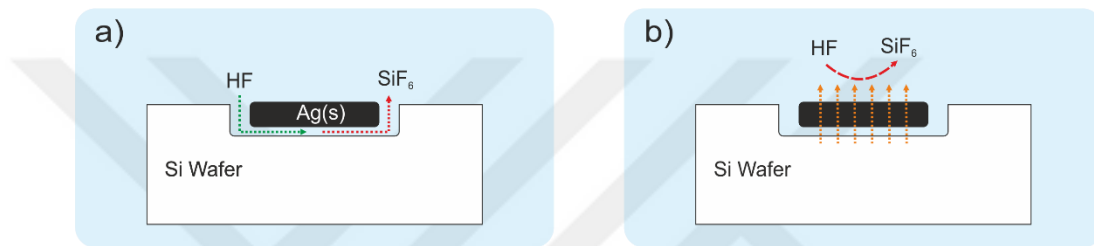
Figure 25 a) Transport of etchant laterally through the metal-Si interface. This model holds for metal particles with relatively small widths. b) Si diffuses through the noble metal to the metal-solution interface and reaction takes place on the surface. This model explains the MAE process for which the metal has long lateral dimensions.

2.3.3. Metal movement

Second point is the sinking of metal through silicon instead of floating into the solution. Ag is the cathode where reduction of peroxide occurs and the silicon surface is the anode such that there is hole flow from Ag to the Si. This results in an electric field directing from Si to Ag. The hole flow from anode to cathode is coupled with H^+ transfer from cathode to anode site, but this time not through but around Ag particle. The movement of the protons from anode to cathode is equivalent to the movement of Ag from cathode to anode due to Galilean invariance. As a result there is a net movement of the Ag particles through the anode site where H^+ is generated and used as a fuel for propulsion of Ag [142]. The mechanism is schematically explained in Figure 26.
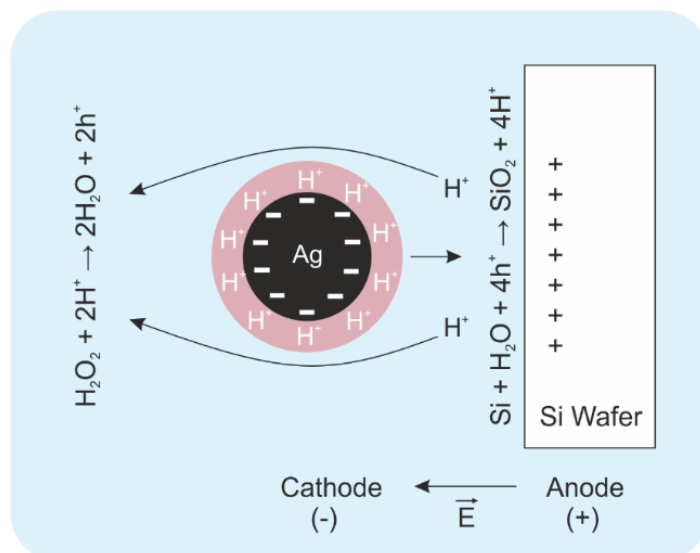
Figure 26 Electrophoretic slip of Ag nano-particle during etching process

Crystallographic orientation dependent etch rates have also been observed for MAE. Several studies have revealed that for low concentrations of oxidative, the preferred direction of etching is (100) direction. This anisotropy is the result of oxidation and etching rate dependence of crystal planes due to chemical bond density variations. On the other hand, with the increase of oxidative concentrations, the etching is takes place normal to the surface[123,143,144].

2.3.4. Metal Type

The widely used metals as catalyst for MAE are, silver, gold, platinum, copper and nickel[99,104,128,145–147]. The process can be facilitated by the use of the salts of the above metals or coating of metal via evaporation or sputtering can be preferred. Main difference between different metals is the reaction speed. For instance, etch rates of 3.5µm/min. can be achieved for Pt assisted etching while for the same solution, 1µm/min is achieved for Au.

2.3.5. Oxidation Agent

It is possible to have etching without addition of an oxidative agent when the process is carried out with metal salts[117]. With these reactions usually, etching profiles with the same cross-sectional area of the metal nanoparticles are observed. This is because of the hole generation rate is equal or less than hole consumption rate at the interface. However, when an additional oxidative agent is included, hole generation rate is greater than the hole consumption in Si-metal interface that result in spreading of holes to the sides of etch front, oxidizing an area greater than the size of the particle[148]. This process results in an etching structure which is not vertical nano-holes or nanowires but slanted or inverted conical holes as shown in Figure 27.
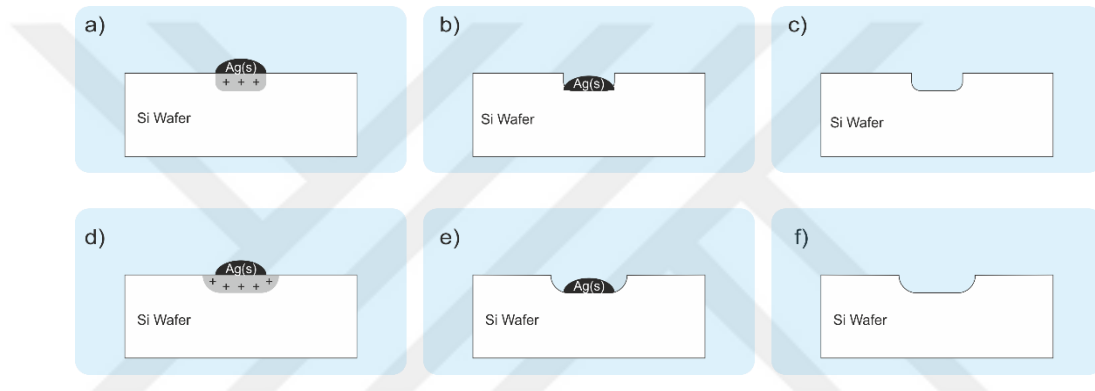
Figure 27 a), b) and c) represents etching without additional oxidative agent. The reaction is limited to metal-Si interface since hole generation rate is less than or equal to hole consumption rate at the interface. This results in vertical steep nano-wires or nano-holes. d), e) and f) represents the etching after a hole injection agent addition. The extra holes that cannot be consumed in the interface are spread around the metal-Si interface and resulting etching has a slanted structure.

CHAPTER 3

APPLICATION OF MAE TO SOLAR CELLS AS A TEXTURING METHOD – NANOWIRES ON MONO CRYSTALLINE SILICON[2]

3.1. Introduction

Mono-c Si holds the advantage of high minority carrier lifetimes as a result of perfect crystallinity without grain boundaries. Moreover, this allows us to obtain a nearly perfect texturing structure anisotropic etching technique discussed in section 2.2.1. On the other hand, as the device thickness becomes smaller, anisotropic pyramid texturing will not be applicable to mono-c Si since the etched amount becomes comparable to whole device thickness[149].

Nanowires formed by MAE are shown to have excellent anti-reflective properties by creating an effective medium with refractive index between air and Si[117][150]. Since the method is a top-down approach, the NW's formed with this method will not only have very good optical properties but also will allow to be used as base material for cell processing by having the same resistivity of the base Si material.

In order to take the advantage of NW texturing and show the proof of the concept MAE was applied to industrial sized and thick mono-c silicon wafers together with pyramid texturing as a reference. Al:BSF Si solar cells were fabricated on wafers textured with NW's and effect of NW length on cell performance was investigated. It was shown

---

that NW texturing could be an alternative to pyramid texture if the problems arising from passivation, junction formation and metallization are solved.

3.2. Experimental

For cell processing, 156x156mm^2, CZ grown mono-c Si, 180µm thick boron doped wafers with a resistivity of 1-3Ωcm were used. Process flow for solar cell fabrication is given in Figure 28. Wafers first went through a saw damage removal (SDR) step in a solution with 20% (wt) KOH for 2 minutes. This removed around 10µm of saw damaged silicon from each side of the wafers resulting in a smooth surface, ready for texturing. SDR was followed by deionized water (DI) rinsing and HF:HCl dip for SiO$_2$ and metallic contamination removal. For texturing, wafers were divided into two sets; one set for reference alkaline texturing and the other was MAE nanowire texturing. Alkaline texturing was conducted in a solution of 3.5% (wt.) KOH, 3.5% (wt.) isopropanol (IPA) at 75°C for 45 minutes. MAE was performed in a solution 0.02M AgNO$_3$ and 4.6M HF at room temperature for 10-50 minutes. Ag dendrites formed on the surface was cleaned by HNO3 dip followed by DI rinsing. After texturing, all wafers (pyramid and nanowire textured) went through another HF:HCl clean, DI rinsing and finally dried under hot N$_2$. Texturing was followed by 50Ω□ emitter formation by phosphorus doping inside a semi-industrial tube vacuum furnace using POCl$_3$ as dopant source. After doping, phosphosilicate glass (PSG) layer formed during emitter formation was removed by an HF dip followed by DI rinsing and hot N$_2$ drying. Subsequently, PECVD SiN$_X$ was deposited on the front surface of the cells as an antireflective coating (ARC) and field effect passivation layer. Metallization was conducted via screen printing of Ag finger to the front and full Al layer to the rear surface. After screen printing, co-firing of the front and back metal was done in a conveyor belt furnace to form front fire through Ag contacts and Al back surface field (Al:BSF). Edge isolation of the cells were carried out by an infrared (1064nm) laser.

Cell performance and I-V characteristics were measured by an AM1.5G calibrated class 3A flash solar simulator. Reflection and EQE measurements were conducted through an integrating sphere – monochromator, lock in amplifier, Si detector setup.

Lifetime measurements were done by quasi steady state photo conductance (QSSPC) method[151]. Textured surface structured was investigated by scanning electron microscopy.
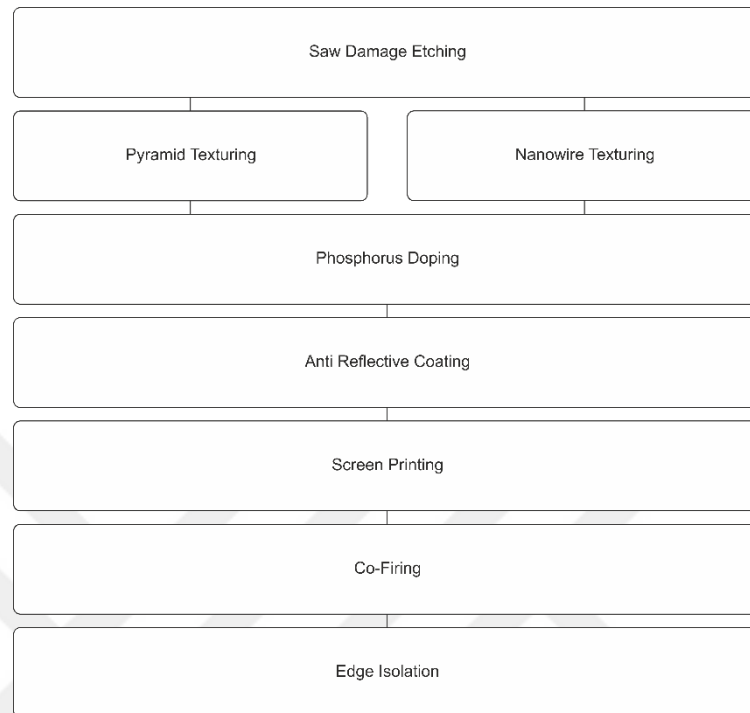
Figure 28 Process sequence for pyramid and NW textured cell production

3.3. Results

The cell texturing process was carried out for full area c-Si wafers. Figure 29 shows the cross sectional SEM images of the NW textured and pyramid textured surfaces.
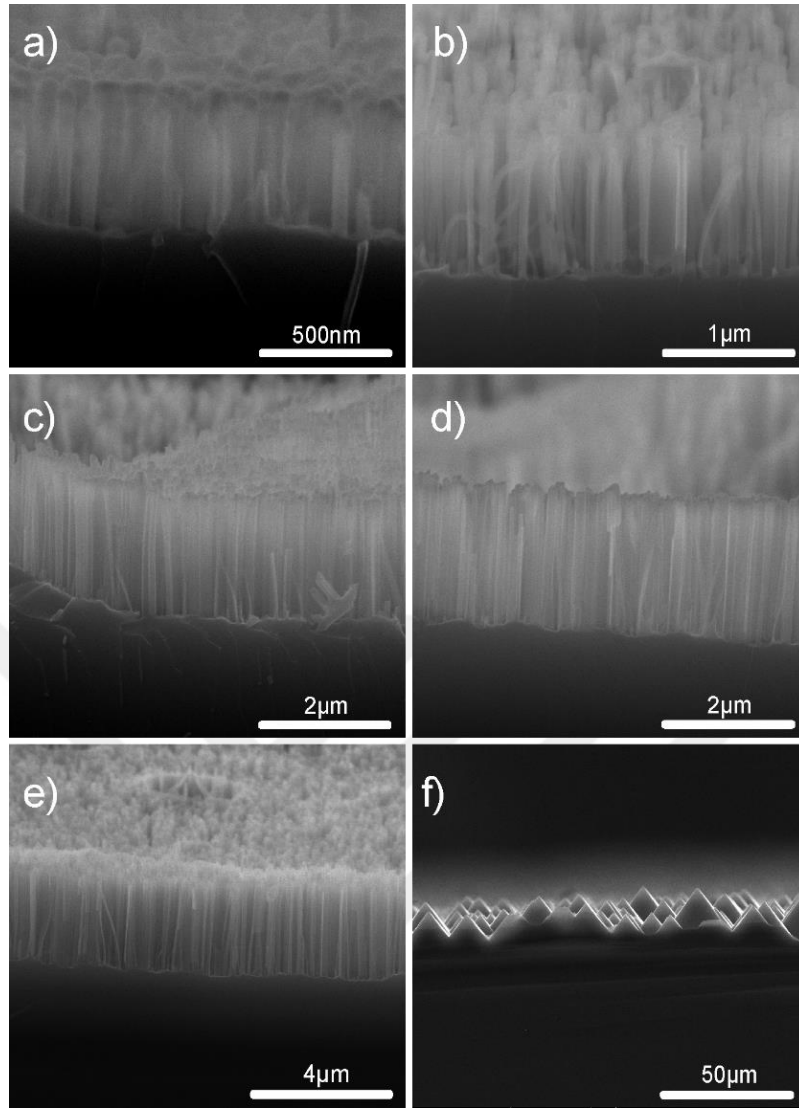
Figure 29 Cross sectional SEM images of the samples with MAE of a) 10 min., b) 20 min, c) 30 min., d) 40 min., and e) 50min. f) sample with pyramid texture.

It is clear that formation of vertically aligned Si NW's was successful with increasing length for higher MAE duration. It is observed that the length of Si NW's is linearly increasing with etching time Figure 30.
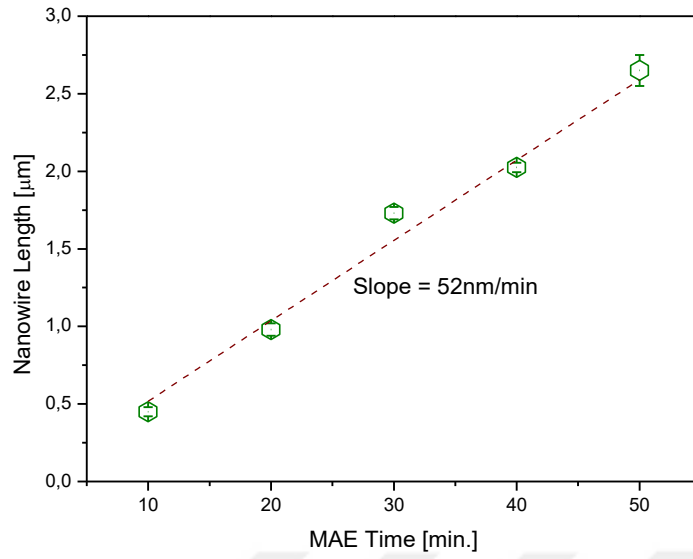
Figure 30 NW length vs MAE time. Almost a linear relationship was observed with a rate of 52nm/min for MAE NW formation.
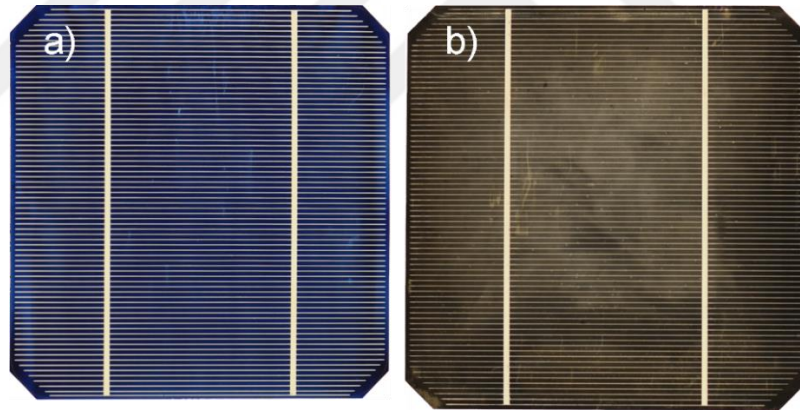
Figure 31 Photo of the cell with a) pyramid texture and b) NW texture

Figure 31 shows the photos of the final cells with pyramid and nano-texturing. We see that the NW textured sample had dark brown color while the reference sample had a blue color. This was attributed to low UV reflection of NW cells when compared to NW textures. For a full analysis of optical properties, spectral total reflectance measurements were conducted (Figure 32).
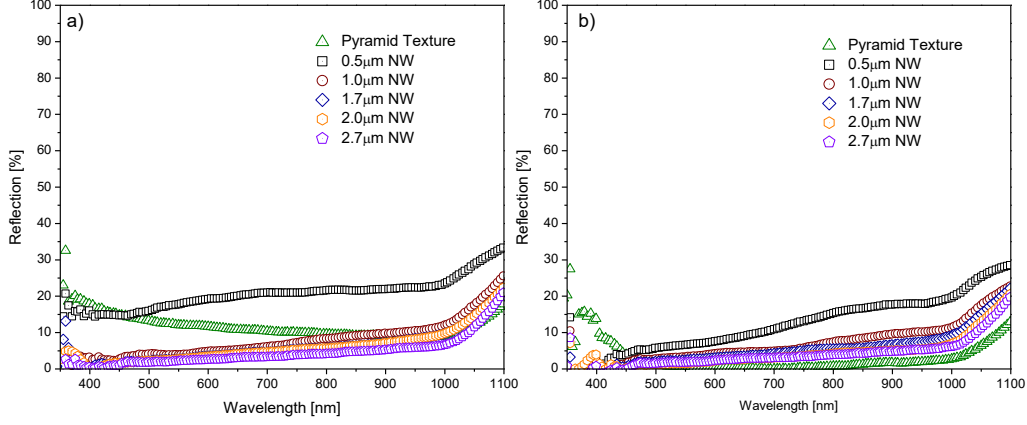
Figure 32 Reflection spectrum for the samples with a) before ARC and b) after ARC

As observed from the images of the finished cells (Figure 31), NW textured samples possess a lower reflection for blue part of the spectrum. In addition, before ARC, it is clear that samples with NW texture longer than 1µm had very low reflection compared to pyramid texture. On the other hand, after ARC, pyramid texture has the lowest reflection. This can be more easily visualized by looking at the AM1.5G weighted reflection averages before and after ARC coating (Figure 33). The weighted reflection is calculated by the formula:

$$R_W = \frac{\int_{350nm}^{1100nm} R(\lambda)\, I_{AM1.5G}(\lambda)\, d\lambda}{\int_{350nm}^{1100nm} I_{AM1.5G}(\lambda)\, d\lambda} \qquad \text{eqn. 7}$$

In eqn. 7;

R_W is the weighted reflection,

$R(\lambda)$ is the reflection from the surface at wavelength λ,

$I_{AM1.5G}(\lambda)$ is the intensity of solar radiation at specific wavelength λ[152].
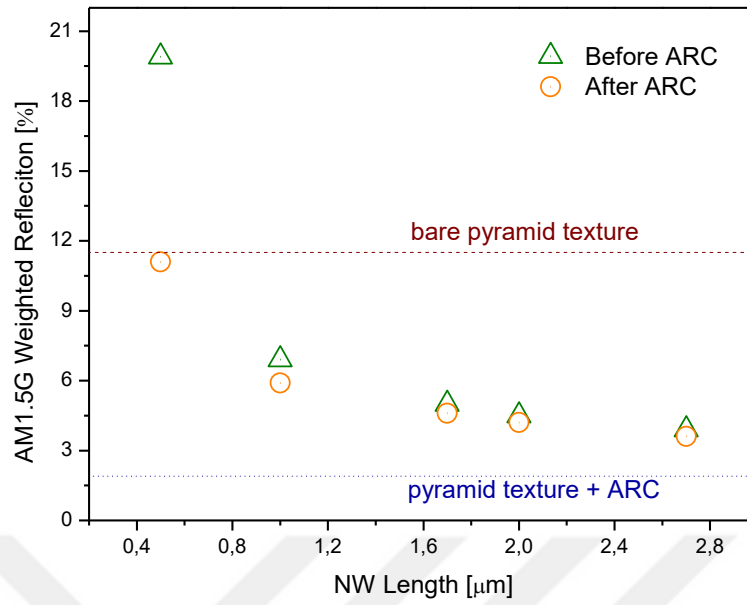
Figure 33 Average reflection for each NW length before and after ARC. Pyramid texture reflection was inserted reference lines. It is observed that with increasing NW length, effect of ARC becomes negligible.

This is attributed to the fact that the ARC is an optimized SiN_X layer with a refractive index of 1.8 which is optimized for pyramid textured surface. On the other hand, for long enough NW's, reflection is very comparable to pyramid textured-ARC coated samples even without ARC. This indicates that a passivation film without ARC property could also be sufficient for only passivation of the NW structures without necessity of optical performance enhancement.

Figure 34 shows the j-V characteristics of the cells textured with different NW lengths and reference pyramid texture. It is obvious that all the cells suffer from low shunt resistance. The problem is attributed to the firing problem that stem from the fast firing furnace used for this process was not very well optimized for PV purposes.
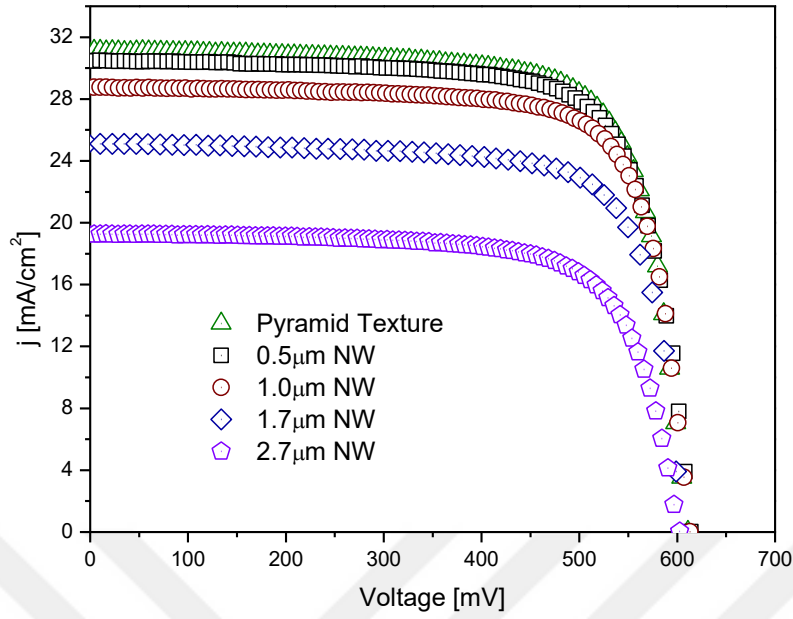
Figure 34 j-V curves for NW and pyramid textured solar cells.

It has been observed that the performance of NW textured samples decrease with increasing NW length, opposite to expected behavior from average reflection values. The cell parameters are summarized in Figure 35.
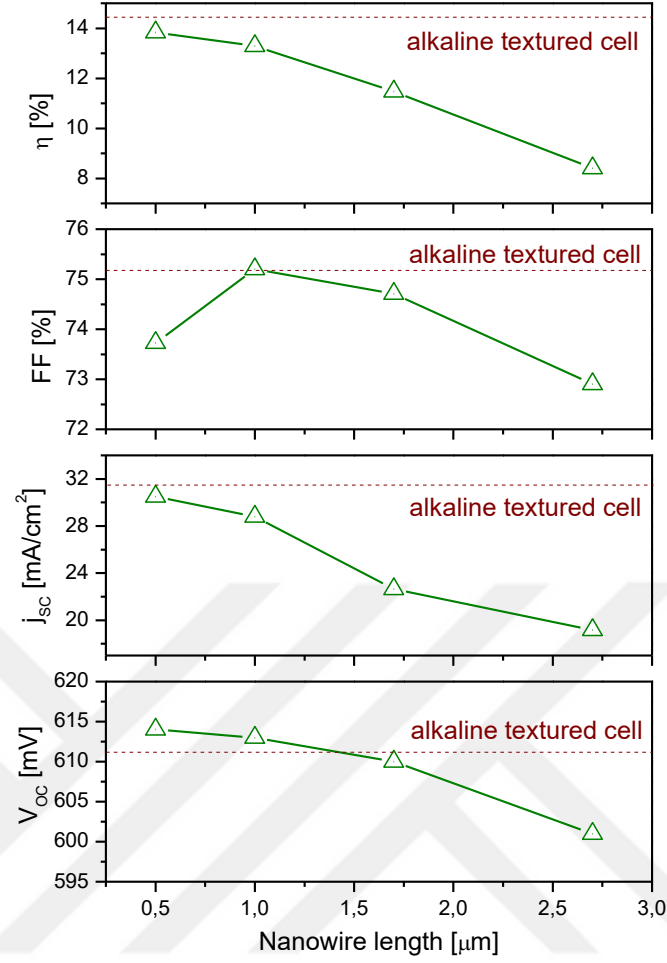
Figure 35 Efficiency, FF, J$_{SC}$ and V$_{OC}$ values as a function of NW length. Value for Pyramid texture is inserted as dash line as reference.

As discussed, short circuit current density is highest for pyramid texture which is in conjunction with weighted reflection values. However, for NW textured samples, as the NW length increases and/or weighted reflection decreases, we observe a decrease in current density. In order to understand the reason for this behavior, IQE spectrum of the samples would be analyzed (Figure 36).
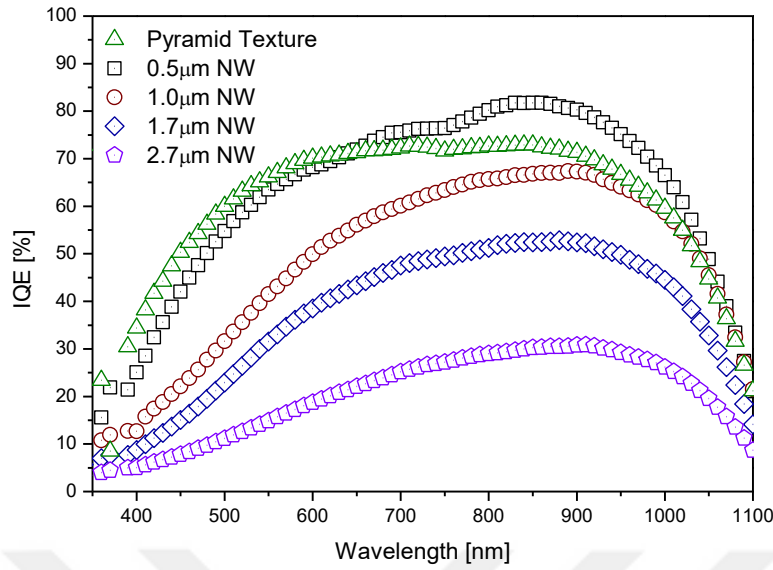
Figure 36 IQE spectrum for the NW and pyramid textured cells

It is clear from IQE results that as the NW length is increased, the blue and then visible response of the cells decrease. This is attributed to the fact that POCl$_3$ diffusion results in a doping profile with a junction depth of 0.5µm for our process. The nanowires have diameters ranging from 50nm to 200nm which is less than half of the junction thickness. As a result, after doping, a single nanowire becomes a highly phosphorus doped structure which suffers from high Auger and surface recombination which was discussed in detail by Oh *et. al.* [94] (Figure 37). Briefly, the carriers generated inside the NW has to travel along the NW to reach the junction for separation. However, very high doping levels inside the NW leads to Auger recombination and increased surface area with lack of conformal passivation results in increased surface recombination. As a result, the probability collection for small wavelength photon generated carriers is decreased.
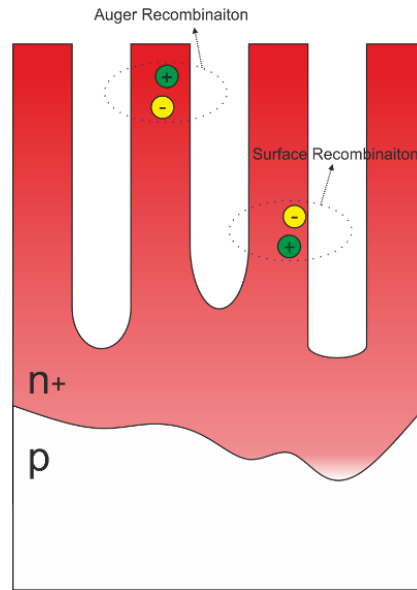
Figure 37 Possible recombination mechanisms that account for decreased blue response of the NW textured cells.[3]

On the other hand, it clear from IQE of the shortest NW textured sample had better response after 600nm. This suggest a better collection efficiency since generated carries have to follow a shorter path which is close to junction depth of a planar cell with the same diffusion.

When the FF of the cells are examined, again a decrease is observed for increasing NW length. One possible reason is the insufficient contact formation. As shown in Figure 38, screen printed Ag fingers were not able to diffuse through the NW structure and touch the Si bulk. Instead, the contacts seem to float on NW structures making a very small contact to the fingers. Since the cross sectional are of an individual NW is low, series resistance losses through the NW during current flow is inevitable. The only advantage here is that the doping is so high in NW that keeps the resistive losses low to some degree. This has been observed by different researcher before and is due to the super-hydrophobic and self-cleaning properties of individual nanowires[153][154].

---

[3] Redrawn with courtesy of Nature Publishing Group
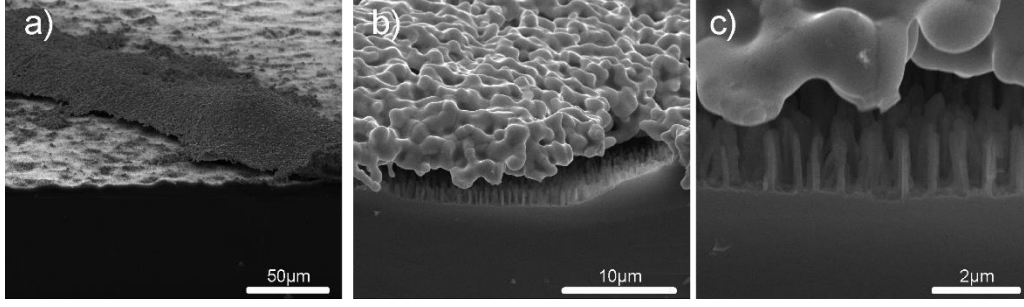
Figure 38 Cross sectional image of screen printed Ag contacts on NW's

Although this explains the decrease of FF after 1µm long NW (Figure 35), the reason for low FF of 0.5µm long NW is not clear. To see this, shunt resistance measurements are conducted via Suns&Voc analysis [155] (Figure 39).
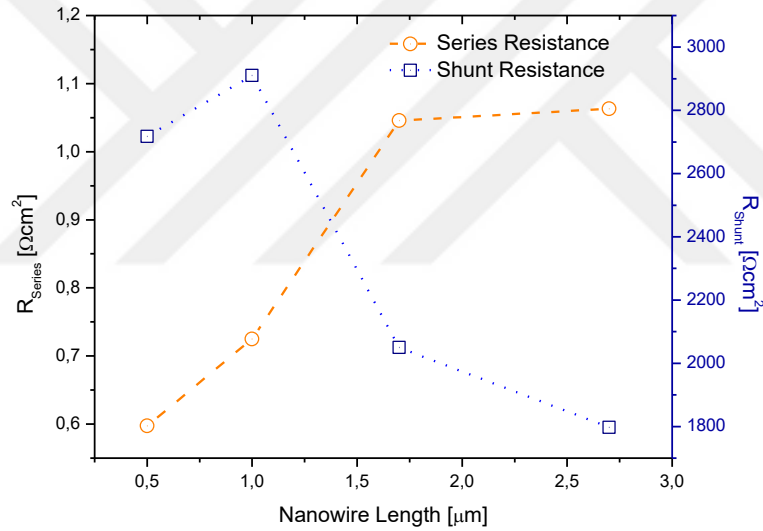
Figure 39 Variation of series and shunt resistances with respect to NW length.

As can be seen from Figure 39, series resistance follows an increasing trend with NW length. This is in conjunction with the floating fingers model we discussed earlier. However, when we analyze the shunt values, we see that the sample with the shortest NW exhibits a lower shunt resistance when compared to the next NW length. This is the reason for lower FF for the shortest NW. Shunts can be attributed to two mechanisms. First one is Ag spiking through the NW structure in to the junction,

effective for shorter NW's. Second one is the tendency of local shunts due non-uniform junction formation for increased NW's length [101,156].

3.4. Conclusion

Silicon nanowires with different lengths were uniformly formed on the surface of industrial sized mono crystalline silicon wafers. It was observed that NW length increased linearly by etching time. Standard $POCl_3$ tube furnace doping, PECVD SiN_X coating, screen printed metallization, co-firing of the contacts and edge isolation was performed on the NW textured samples as well as pyramid textured wafers as reference. Reflection measurements revealed that increased NW length lead to lower average reflection from the un-coated surface. After anti reflective coating, average reflection for pyramid textured wafer was lowest since optimization was based on this reference structure. On the other hand, reflection of UV and blue part was still less than pyramid texture for NW samples that resulted in dark brown color of the cells. When cell results were analyzed, it was observed that increased NW length resulted in lower j_{SC}, mainly because of the low blue response of the cells. This collection problem was attributed to increased Auger and surface recombination in very highly doped, high surface area NW structures that cannot be passivated conformally by PECVD. In addition, low FF values were linked to screen printed contact problems and shunting effect due to doping non-uniformities. In the end, NW textured cells with an efficiency of 13.9% has been fabricated while for pyramid textured reference, efficiency was 14.4%.

CHAPTER 4

APPLICATION OF MAE TO SOLAR CELLS AS A TEXTURING METHOD –
NANOWIRES ON MULTI CRYSTALLINE SILICON[4]

'The perfect is the enemy of the good'

Voltaire

4.1. Introduction

One way of decreasing the cost per watt of PV energy production is decreasing the production costs while preserving the efficiency. Multi-c silicon is therefore a cost effective alternative to mono-c silicon where material cost is decreased. However, efficiencies cannot be as high as mono-c as described below due to optical and electrical losses. First of all, as a material with lots of grain boundaries, multi-c Si is prone to bulk recombination losses. Secondly, since the surface consists of different crystal orientation grains, anisotropic alkaline texturing used for (100) oriented mono-c cannot be applied here. Instead, isotropic acidic texturing is applied for multi-c wafers which does not result in reflection values as low as pyramid texture[157]. In addition, since the process does not yield perfectly formed structures such as pyramids with (111) oriented faces, a standard way of texturing has not been established yet. Many studies have been focused on multi-c silicon texturing such as inject texturing or laser texturing [108,158]. However, none of the proposed processes are applicable

to industrial production due to throughput problems. On the other hand, MAE can be an alternative to iso-texturing of multi-c wafers as a wet chemical approach with possibility of fabrication of very low reflection surfaces.

In this study, we apply NW texture to multi-c silicon solar cells to compare the effects of NW length on cell performance together with a reference cell textured by isotropic texturing. The problems arising from doping and passivation remained still while it was observed that the contacting problem was not pertinent for NW on multi-c cells.

4.2. Experimental

Cells were fabricated on 156x156 mm^2 full square, boron doped, multi-c Si solar wafers with a resistivity of 1-3Ωcm and a thickness of 200μm. Wafers were divided into two sets; one set for MAE NW formation and one set for standard iso-texturing. All wafers went through the same cell fabrication process steps mentioned in section 3.2 except for iso-texturing of reference set. For texturing of multi-c with acidic mixtures, saw damage etching step was bypassed and process was carried on as cut wafer surfaces. Texturing solution consisted of 12:1:1 HF:HNO$_3$:H$_2$O solution and process was carried out at room temperature for 30sec. After rinsing in DI and HF:HCl dipping, a 1% (wt) KOH dip for the removal of porous Si formed during the stain etch was carried out. Subsequently, all sets went through the RCA$_2$ clean together with NW textured samples. NW fabrication with MAE was carried out for durations of 5, 10, 20, 30, 40 and 50 min. Characterization of the samples was also carried out with the methods mentioned in section 3.2. The process flow is given in Figure 40.
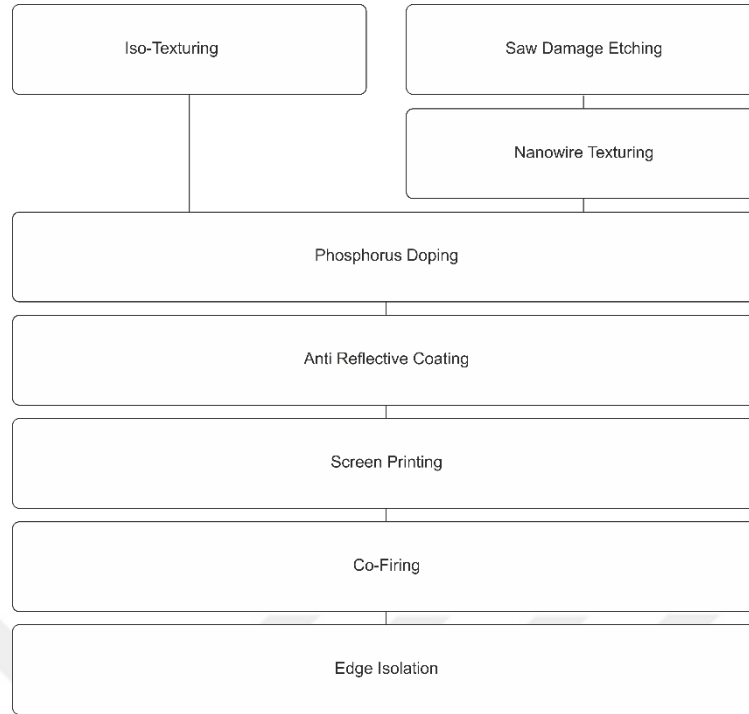
Figure 40 Fabrication sequence for NW and iso-texture multi-c cells

4.3. Results

Figure 41 shows the cross sectional SEM images of the NW structured formed on the surface of multi-c wafers via MAE for different etching durations. Since the multi-c wafers compose of different oriented grains, it was not possible to have a sharp breakage for perfect cross sectional sample preparation. On the other hand, by analyzing different SEM images for each etching time, again a linear dependence of NW length with respect to etch time was observed (Figure 42). The etch rate was 10nm/min less than for the case of mono-c texturing (Figure 30). This was attributed to the dependence of etch rate to solution temperature which was maintained at room temperature and controlled with a tolerance of ±2°C. The dependence of etch rate to temperature was calculated to be 9.3nm/min/°C previously [117]. This implies a 1°C of difference in etching solution which is in tolerance limits of the control system.

47
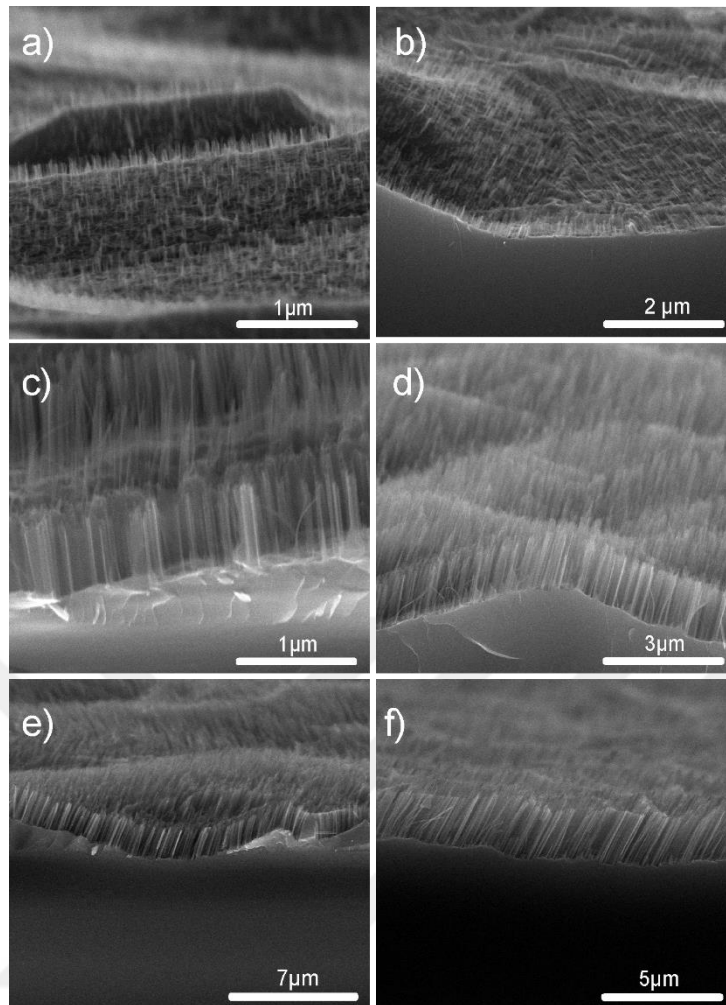
Figure 41 SEM images of the wafers for a) 5min., b) 10min., c)20 min., d) 30 min., e) 40 min., and f) 50 min. of etching in MAE solution
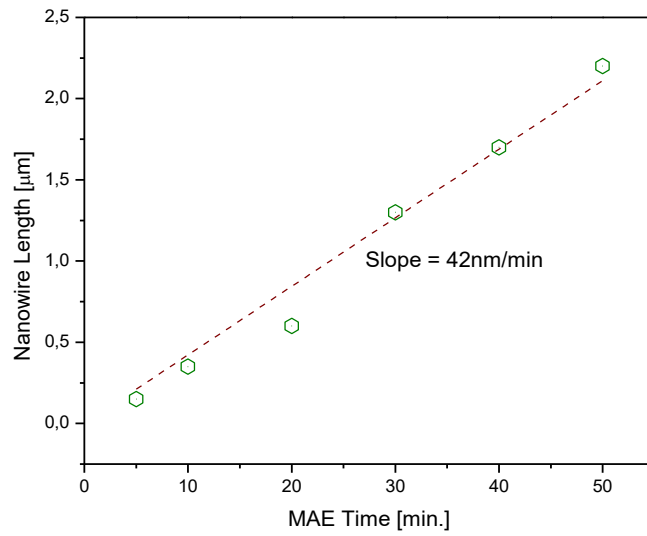
Figure 42 Etching time vs. NW length. A linear relation was found as in the case of mono-c counterparts.

For the reference set, SEM image of the surface fabricated by iso-texturing is given in Figure 43.
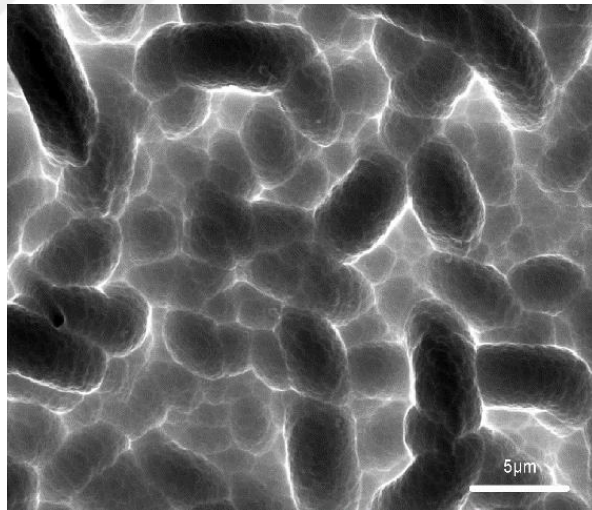
Figure 43 Surface texture formed after acidic etching of the multi-c wafers.
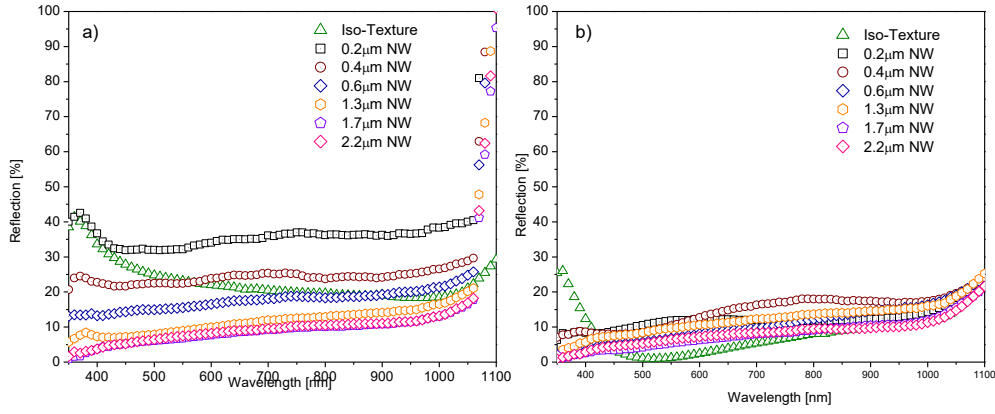
Figure 44 Reflection spectrum for samples with a) NW and iso-texture, b) after ARC

As in the case of mono-c results, highest response to ARC was obtained in iso-textured sample (Figure 44). On the other hand, to see the effect of texturing and ARC, again AM1.5G weighted average reflection was calculated (eqn. 7) (Table 2) and full cell images are given in Figure 45.

Table 2 AM1.5G weighted reflection for NW and Iso-textured samples before and after ARC

Sample	Average Reflection Before ARC [%]	Average Reflection After ARC [%]
Iso-Tex	23.2	6.9
0.2μm NW length	37.6	11.7
0.4μm NW length	25.9	13.6
0.6μm NW length	19.0	9.6
1.3μm NW length	12.7	11.4
1.7μm NW length	9.9	7.4
2.2μm NW length	10.2	7.7
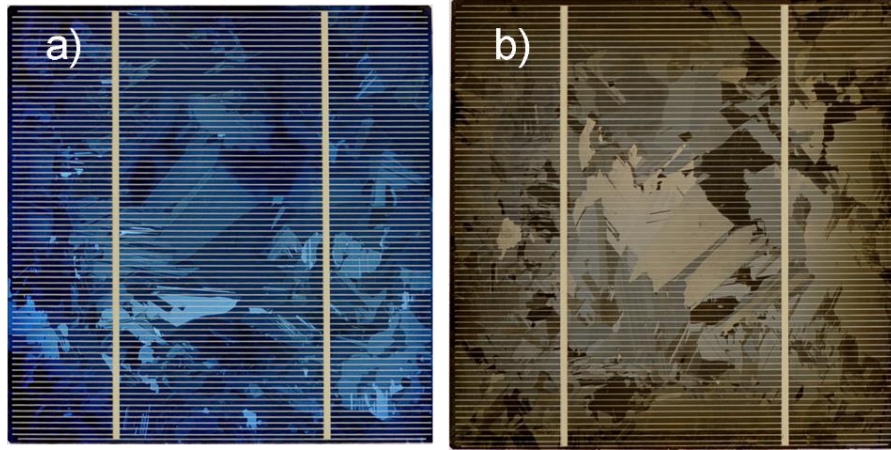
Figure 45 Photos of the finished samples: a) iso-textured sample, b) NW textured sample

The reflection difference for the cells textured by NW and standard texturing is lower than the case of mono-c after anti reflective coating. Therefore, application to multi-c looks more promising as discussed in the introduction chapter (section 4.1).

When we analyze the j-V curves of the finished cells, we observe a similar behavior to NW textured mono-c cells (Figure 46). Highest efficiency is again observed for reference set while the performance decreases with increasing NW length, which is opposite to what is expected from reflection results (Figure 47). Other than FF, all values for cell parameters are lower than the reference set. This brings us to the conclusion that the problems arising from Auger and surface recombination is still dominant. On the other hand, higher FF compared to reference suggests that the series resistance problem is not holding out.
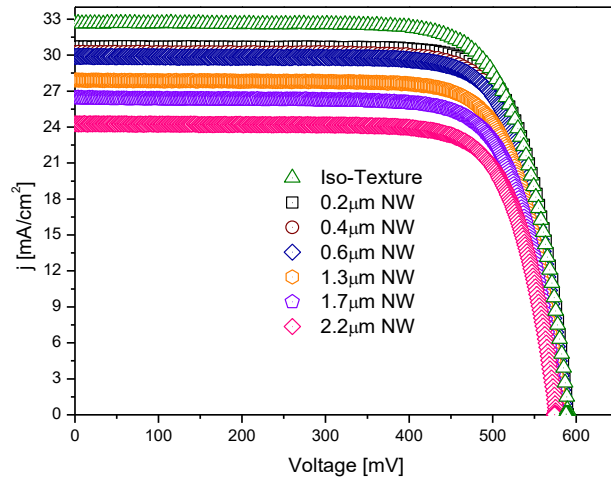
Figure 46 j-V curves for reference and NW textured samples.
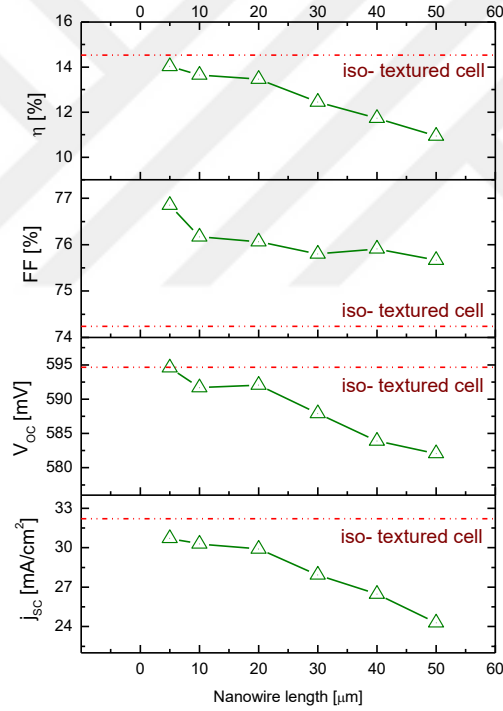
Figure 47 Cell parameters for NW textured samples. Reference values are added as dashed lines.

In order to understand this behavior of FF, SEM images of the samples after metallization was taken (Figure 48). It is clear from the SEM images that the contact formation was more successful when compared to mono-c screen printed metallization. This was attributed to the difference of density of the nanowires formed

52

on the surface of the multi and mono-c Si wafers. As seen from Figure 48 c) and d), multi-c wafers had a very less density of NW formed when compared to mono-c wafers. The reason for this is the anisotropic property of the MAE which will be discussed in detail in the following chapters[114,123,144].
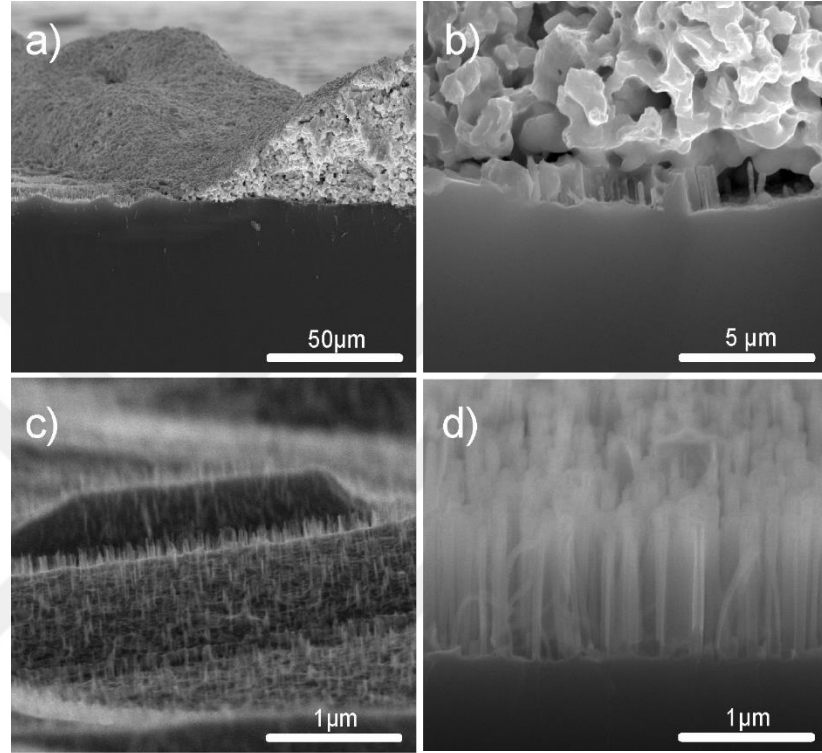
Figure 48 SEM images of the a) multi-c NW textured sample with Ag contacts on top, b) a closer look to multi-c NW textured sample – Ag contact interface. c) shows the NW texturing of multi-c wafer and d) shows the NW texturing of mono-c wafer.

IQE measurements also confirm that the surface passivation and Auger recombination problems still persist for multi-c wafers and collection efficiency dramatically decreases with 1.3µm and longer textured nanowires (Figure 49).
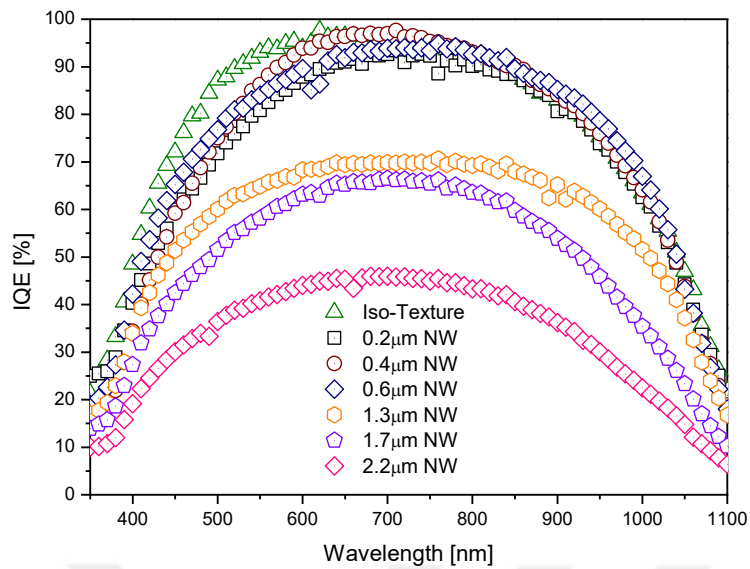
Figure 49 IQE spectrum for the NW and iso-textured wafers

On the other hand, just to have an idea about the applicability to industry, a comparison was carried out in terms of etching process in Table 3. It is clear that HF consumption is decreased dramatically while HNO_3 usage is increased. On the other hand, HNO_3 used in mainly due to dissolving of Ag dendrites and may be used as a recycling agent for $AgNO_3$ in the future.

Table 3 Comparison of process parameters for 5 minutes of NW texturing and reference iso texturing.

Cell	Etch Time [min.]	HF (Relative)	HNO_3 (Relative)	$AgNO_3$ [g]	KOH [g]	Eff. (%)
Ref.	1	8.5	1	x	80	14.4
150nm NW	5	1	3	2.5	x	14.0

4.4. Conclusion

Multi crystalline silicon solar cells textured with different lengths of nanowires and iso-texture as reference has been fabricated with the same procedures followed in Chapter 3. Results revealed that the problems arising from recombination due to surface area enlargement, lack of conformal passivation and Auger recombination as a result of high doping in NW structures remained the efficiency deteriorating factors. Nevertheless, series resistance issue was not observed as a result of lower density of NW due to anisotropic nature of MAE. When the process and effort was compared together with efficiency output, it is seen that the shortest length NW texture had a chance as an industrial alternative to isotropic etching process if recycling of Ag can be succeeded with tolerable costs.

CHAPTER 5

METAL ASSISTED ETCHING WITH HNO$_3$ AS A HOLE INJECTION MECHANISM[5]

'God created the bulk; surfaces were invented by the devil.'

Wolfgang Ernst Pauli

5.1. Introduction

Chapter 3 and Chapter 4 draws the conclusion that application of NW as a texturing method for mono and multi crystalline silicon has generic problems arising from increased surface recombination, auger recombination and series resistance. The last two are arising from cell process parameters to be optimized other than MAE while surface recombination is controllable via adjusting the shapes formed by changing the texturing parameters. It was already discussed in section 2.3.5 that the etching front's shape can be adjusted by addition of oxidation agents to the MAE solution. Effect of H$_2$O$_2$ as an oxidant has been discussed previously by several groups [115,159]. It has been shown that additional oxidative results in nano-cone shaped structures that can be facilitated for wafer texturing. On the other hand, for MAE with Ag as the catalyst, removal of metal dendrites of the process is completed by nitric acid (HNO$_3$), which is also another oxidative agent for Si. This brings the idea of using HNO$_3$ not only in cleaning but also in MAE process instead of H$_2$O$_2$ so that the number of chemical

---

[5] Contents of this chapter has been published in 2016, IEEE Journal of Photovoltaics, 1-7

species used in a texturing process will be decreased. In this part of the thesis use of HNO_3 in MAE as an optimized surface texture for c-Si is studied in detail.

5.2. Effect of solution parameter on surface structures

In this section, MAE solution parameters that effect the surface structures' shape is analyzed through SEM imaging and reflection/transmission measurements. Elimination of specific parameters were carried out by pre-defined tolerance levels as well as visual analysis.

5.2.1. Chemical concentration and time

Experiments were conducted on saw damage etched, 1-3 Ωcm p type doped, all RCA_2 cleaned and oxide stripped mono-c Si wafers. MAE was carried out in a solution, containing 200ml of DI water and different amount of chemicals for different etching times given in Table 4. After MAE, all wafers went through a 2 min. rinsing, 15 min. HNO_3 cleaning, 2 min. rinsing, HF:HCl dip, rinsing and N_2 drying step. This helped the removal off all residual metallic contamination and SiO_2 formed during the process. Reflection from the surface was measured via an integrating sphere setup and surface imaging was carried out by scanning electron microscopy.

Table 4 Parameters varied for etching optimization resulting in 120 different sets

AgNO$_3$ [mg]	HNO$_3$ [ml]	HF [ml]	Etching Time [min]
20	1	5	4
50	10	10	8
x	50	20	15
x	*x*	40	30
x	*x*	*x*	60
# of sets × 2	× 3	× 4	× 5
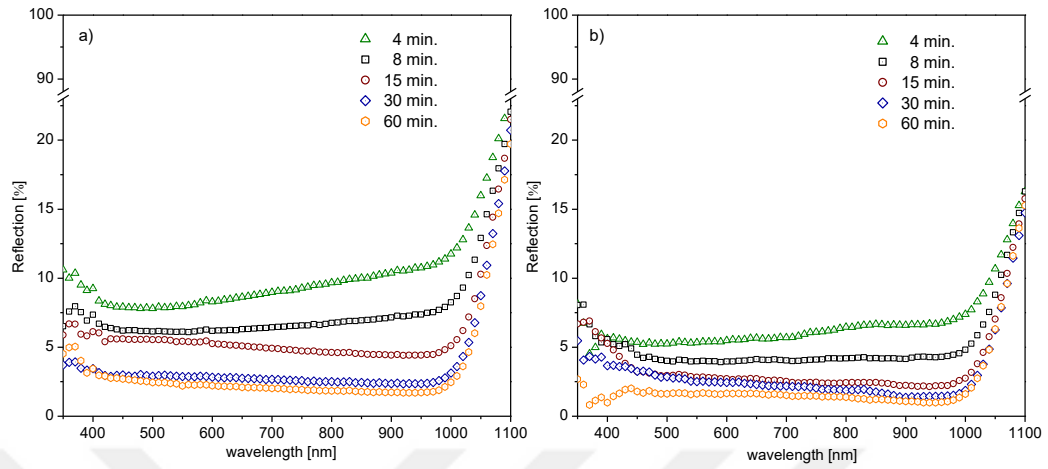
Figure 50 Reflection spectrum for samples etched with 40ml of HF, 50ml of HNO$_3$ and a) 20mg of AgNO$_3$, b) 50mg of AgNO$_3$

Figure 50 shows the reflection spectrum of a specific concentration of HF and HNO$_3$ to show the effect of etching time and AgNO$_3$ concentration. We observed that AgNO$_3$ had little effect on reflection for same process parameters. On the other hand, etching time decreases the reflection monotonously. It is also interesting to note that all reactions resulted in reflections less than 10% throughout the spectrum. When compared to pyramid texturing around 13% reflection completed in at least 15min., the process seems to be promising in terms of optical performance.

For all samples, AM1.5G weighted reflection was calculated using eqn. 7 to have an easier view of effect of all different parameters on reflection (Figure 51 and Figure 52). Color mapping was configured such that; the lighter the grey color is, the more reflection is observed from the wafer surface and the darker for low reflection.
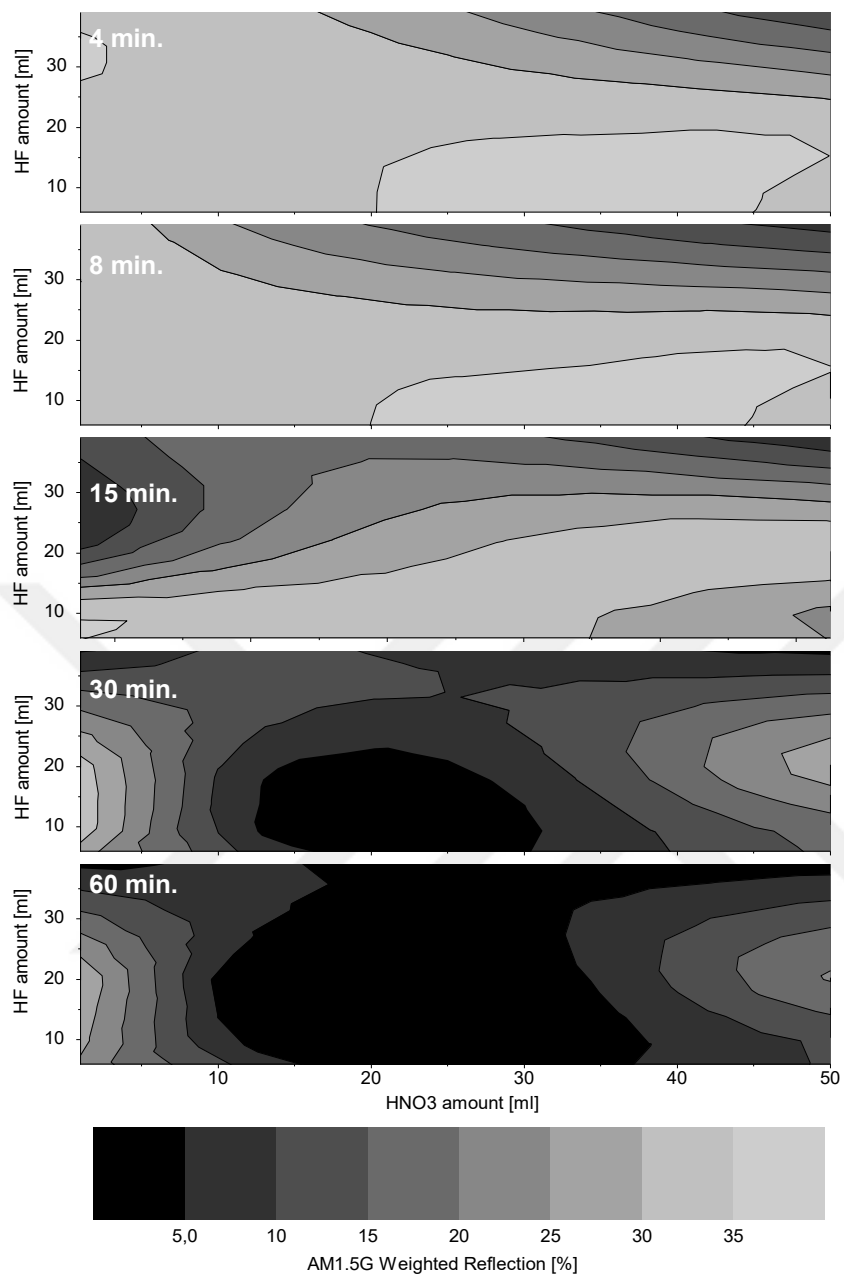
Figure 51 Effect of HF and HNO₃ concentration on average reflection of the samples for etching times 4 min. to 60 min. H₂O is 200ml and AgNO₃ is 20mg.
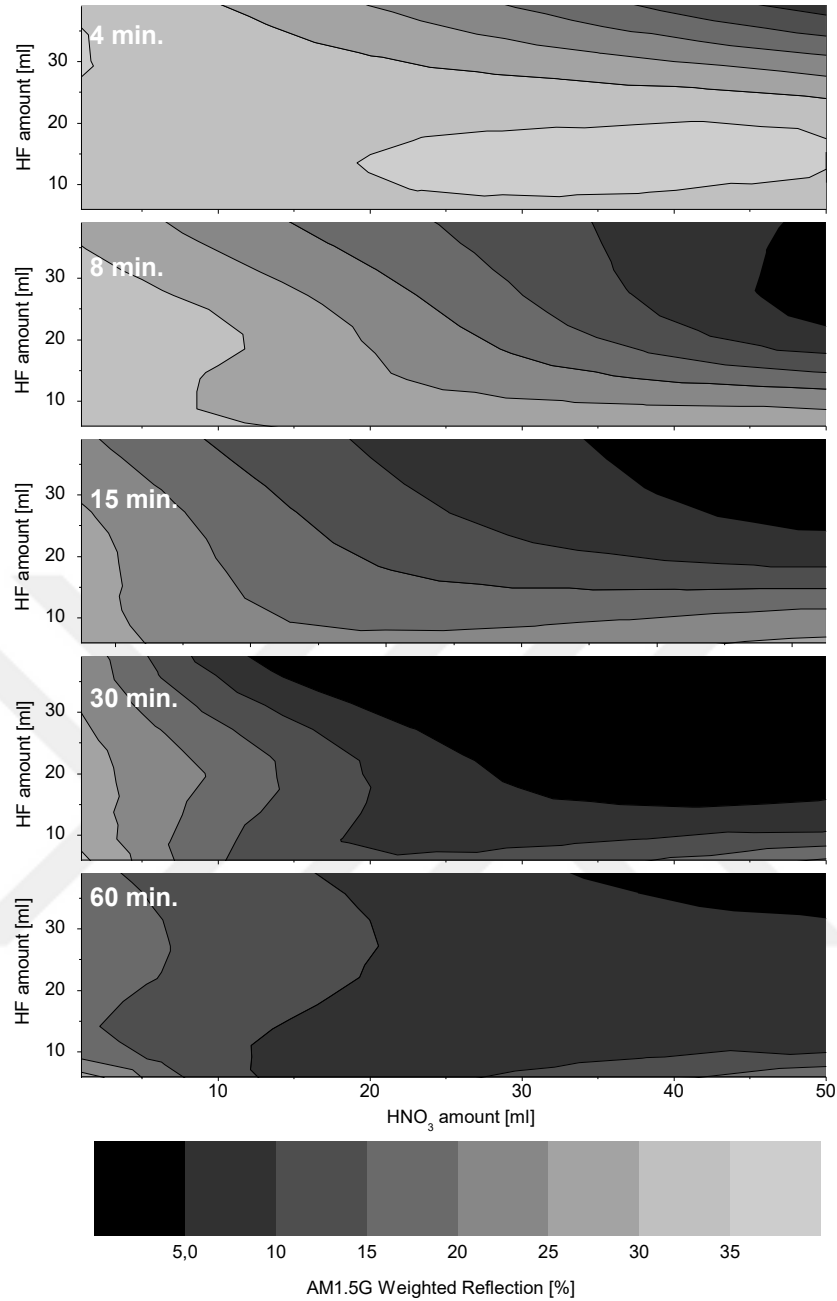
Figure 52 Effect of HF and HNO₃ concentration on average reflection of the samples for etching times 4 min. to 60 min. H₂O is 200ml and AgNO₃ is 50mg.

In Figure 51 and Figure 52, every single graph corresponds to a specific etching time starting from 4min. to 60min from top to bottom. For 50mg of AgNO₃, it is clear that increased texturing time leads to lower reflection from the surface. For 4 min. of

61

texturing, average reflection that less than <10% can only be observed for highest concentration of HF and HNO_3 while with increased time, the low reflection region gets wider. For each texturing duration, increased HF leads to decreased reflection and increased HNO_3 leads to decreased reflection. However, for 20mg of $AgNO_3$ a minimum of reflection is followed by an increase with the increase of HNO_3 concentration. In addition, several minima may occur for some set of parameters, which can be attributed to less reliability of the solution due to lower amount of catalyst.

Figure 53 and Figure 54 show the SEM images of the samples after MAE etching. In Figure 53, HF amount is kept constant and HNO_3 is increased from left to right and $AgNO_3$ is increased from bottom to top. It was observed that for lower HNO_3 concentrations, structures formed were nano-wire like.
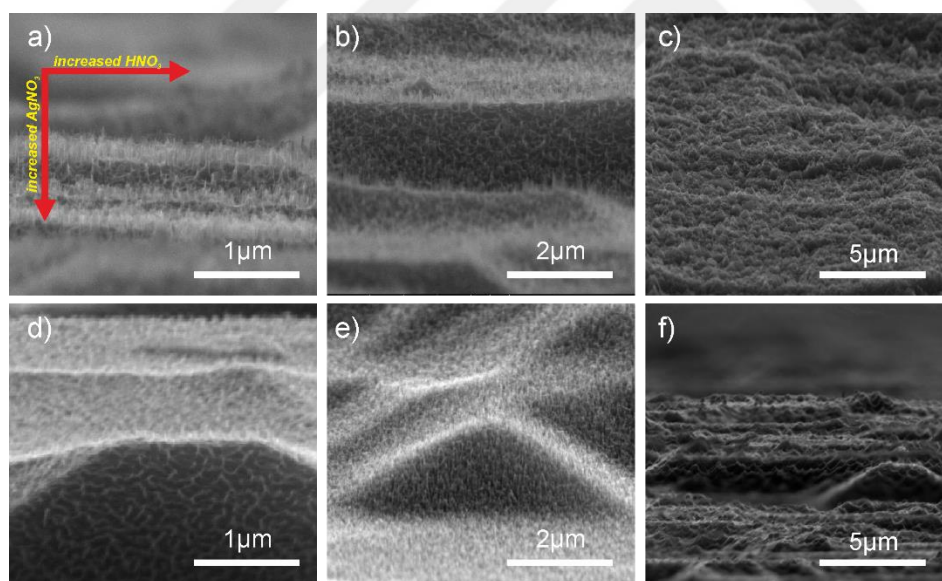
Figure 53 SEM images of samples etched in a solution of constant HF. HNO_3 is incresing from left to right and $AgNO_3$ is increasing from top to bottom.

On the other hand, with increasing HNO_3, structures started to form in a more blunt form. Furthermore, increased $AgNO_3$ amount lead to denser structures.

Figure 54 also brings the same conclusion in which HNO$_3$ is kept constant and HF is increased from left to right. Again we see that lower HNO$_3$ or in other words higher HF concentration results in NW like structure formation while lower HF lead to nano-cone like structures. The effect of AgNO$_3$ was observed to be same for this case.
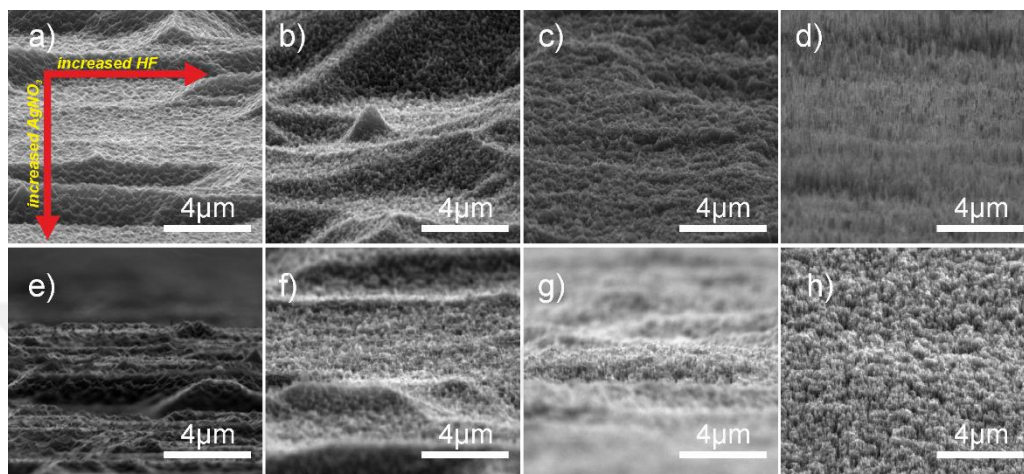
Figure 54 SEM images of samples etched in a solution of constant HF. HNO$_3$ is incresing from left to right and AgNO$_3$ is increasing from top to bottom.

SEM analysis revealed that the process results were in agreement with the literature in the way that addition of oxidative agents resulted in a change of the surface structures Figure 27. In our case, HNO$_3$ addition leads to additional hole injection to Si with the following reaction (eqn. 8) [118,140,160];

$$HNO_3 + 3H^+ \rightarrow NO + 2H_2O + 3h^+ \qquad \text{eqn. 8}$$
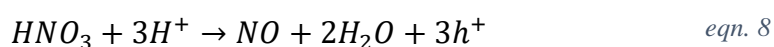
Schematics of the proposed mechanism is given in Figure 55.
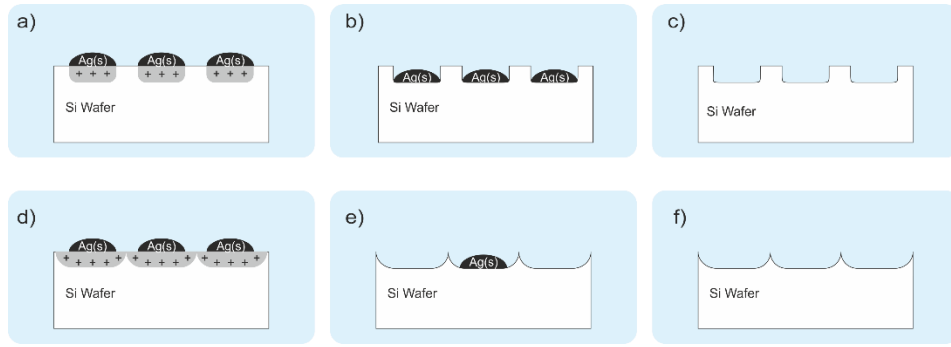
Figure 55 MAE mechanism with low HNO$_3$ high HF concentration is given in a), b) and c). Hole generation rate is less than consumption rate at the interface, resulting in a directional etching (silicon nano-wires). When HNO$_3$ is high and HF is low, extra generated holes are swept through the edges Si-Ag interface, resulting in nano-cone like structures in d), e) and f).

In the analysis, samples with average reflection greater than 25% was excluded because of the low optical performance even when compared to standard multi-c iso-texturing. In addition, sample with NW formation was also excluded since non-nanowire structures are desired (Table 5). However, as a reference, one set with structures close to NW was included in the analysis for performance comparison.

Table 5 Eliminated parameters due to high reflection and NW formation for 20mg and 50mg of AgNO$_3$

HF [ml] HNO$_3$ [ml]	5	10	20	40
1	4 - 60 min.	4 - 60 min.	4 - 60 min.	4 - 60 min.
10	4 - 60 min.	4 - 60 min.	4 - 60 min.	4 - 60 min.
50	4 - 15 min.	4 - 15 min.	4 - 15 min.	4 - 15 min.

5.2.2. Reusability

In order to transfer this techniques industrial lines, not only optical performance but also reliability should be assured. For the repeatability of the process and reusability of the etching solution, a series of experiments were designed. This experiment was

called as 'chemical aging test' since it checks the solutions performance in terms of max number of usability.

The workflow for a chemical aging test of a specific etching solution is given in Figure 56
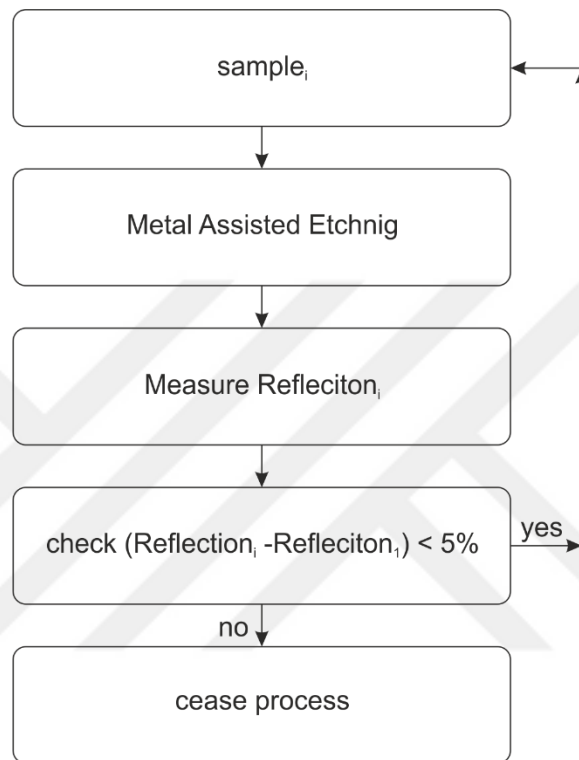
Figure 56 Process flow for a chemical aging test sequence for a specific chemical concentration

For this testing, a fresh solution of specific concentration is first prepared. One sample is textured in the solution for 60min. and then cleaned and reflection was measured. After 1st sample, a second sample is also textured in the same solution for 60 min. without refreshing the chemicals. After the cleaning of the second sample, reflection was also measured and was compared to the reflection of sample 1. If the difference is below the limits, the process is continued until the resulting texturing does not yield reflection values lower than the limits. An additional constraint is put forward that if a solution is able to texture 20 samples with results within the limits, the process is again stopped and the solution passes the test. The average reflections vs. number of samples

etched in one solution is given in Figure 57. It is clear that increased catalyst resulted in more repeatable results. In addition, increased HF is also resulting in higher number of samples that can be etched in one solution.
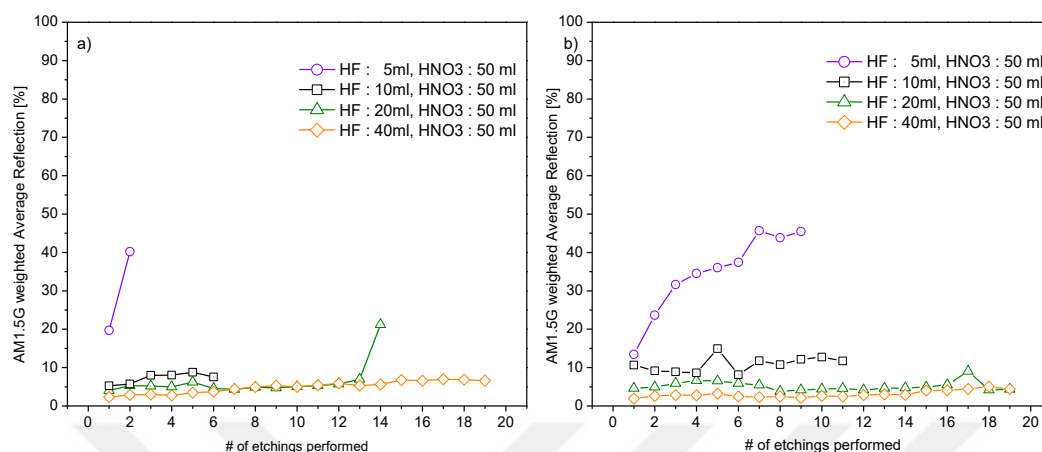
Figure 57 Average reflection as a function of the number of samples etched in one solution for a) 20mg of AgNO₃ and b) 50mg of AgNO₃

For better visualization, statistical graphs has been plotted as seen in Figure 58.
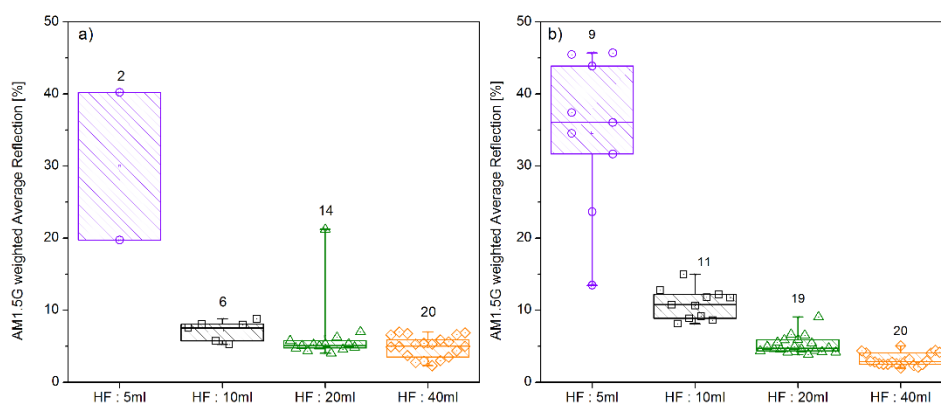
Figure 58 The distribution of average reflection with respect to chemical concentration for a) 20mg of AgNO₃ and b) 50mg of AgNO₃. Total number of etched samples are given as data label on top of each whisker. Nitric acid amount is fixed to 50ml. and the distribution is drawn according to 25-75 percentile of the data

Again it is seen that increased HF lead to lower reflection together with lower deviation and higher number of samples to be etched in the same solution. On the other hand,

when Figure 58 a) and b) are compared, we see that higher amount of catalyst result in a tighter distribution and higher number of samples to be etched for independent of HF concentration. As a result of this study, the sets with lower concentration of $AgNO_3$ were also excluded.

5.2.3. Passivation

In this chapter, results on the response of the surface to processes that are being used for standard cell production are presented. First smoothing of the surface for reducing surface recombination and then the effect of doping on the optical properties are discussed. Lifetime results after passivation will be given as a conclusion in the end of the section.

5.2.3.1.   Surface Smoothing

Increased surface area as a result of nano-texturing had resulted in very low blue response in mono and multi crystalline silicon solar cells presented in Chapter 3 and Chapter 4. The addition of HNO_3 aimed to decrease the surface area by adjusting the shape of the structures while keeping the optical performance high. On the other hand, induced damage during the MAE process deteriorates the surface quality resulting in high recombination[95]. One way to prevent this issue is to apply a short KOH/NaOH dip where the porous layer on the surface is etched very fast resulting in smoothing of the surface [82,108,115,161,162]. For surface smoothing, wafers were textured with four different metal assisted texturing recipes. After texturing, each wafer was exposed to a 1% (wt) KOH solution for different time intervals. After cleaning and drying, reflection experiments and SEM imaging was conducted.
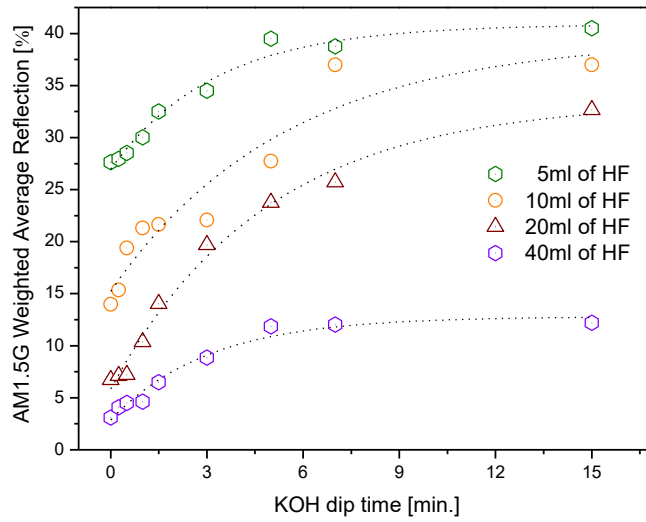
Figure 59 Effect of KOH dipping on reflection from the surface of samples with different nano structure texturing

Average reflection of the samples with increasing KOH dip time is given in Figure 59. All samples showed an increased reflection for higher surface smoothing times as expected. On the other hand, even though an intuitive conclusion can be made from the reflection measurements, however, the ultimate results are obtained by lifetime measurements.
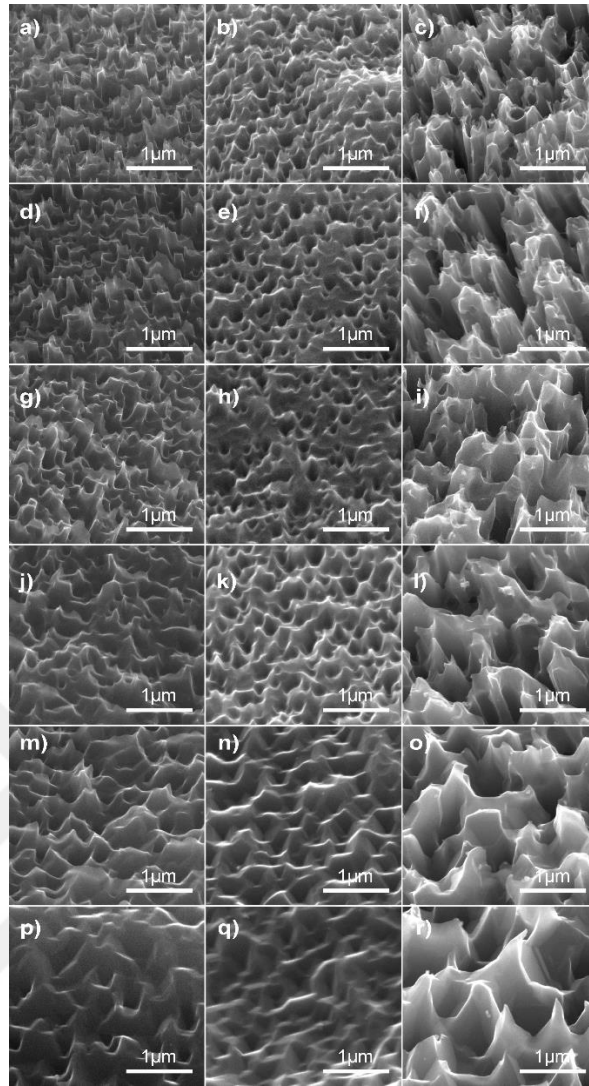
Figure 60 Column starting from a) is for 10ml of HF, b) is for 20ml of HF and c) is for 40ml of HF. From top to bottom, each row corresponds to 15, 30, 60, 90, 180 and 300 seconds of KOH dipping

Figure 60 shows the SEM images of the surfaces with increasing KOH dipping time. As expected from reflection data, the smoothing was successful and lead to non-complex surface features with increased time. Even for some samples (Figure 60 m), n) and p)), formation of inverted pyramid structures was initiated as a result of anisotropic etching behavior of KOH.

5.2.3.2. Effect of phosphorus doping

For solar cell production, phosphorus doping is utilized for p-type wafers in order to from p-n junction. Doping process is carried out in a tube furnace at around 830°C.

The process mainly consists of two steps, 'pre-deposition' of the dopant glass to the surface and 'drive-in' for diffusion of dopant from glass to the silicon bulk. During the doping process, O_2 and $POCl_3$ (carried by N_2) are reacted on the surface of Si with the following mechanism (eqn. 9, eqn. 10) [163]:

$$4POCl_3 + 3O_2 \rightarrow P_2O_5 + 6Cl_2 \qquad \textit{eqn. 9}$$

$$2P_2O_5 + 5Si \rightarrow 4P + 5SiO_2 \qquad \textit{eqn. 10}$$
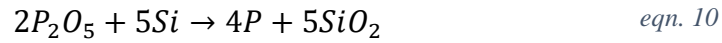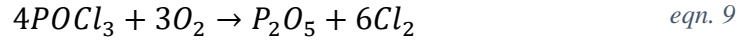
As can be seen from the reactions, the silicon is oxidized throughout the process. For a micro-meter sized texture on the surface, the oxidation during the diffusion process will be negligible while for nano-structures, the process may result in complete oxidation of the nano-structure which will be etched away during PSG cleaning process by HF.

In order to see the effect of a standard doping recipe, MAE samples were subjected to phosphorus doping and cleaning process. Reflection from the surface before and after the doping process is given in Figure 61. It has been observed that a difference of 2.5% absolute was the maximum for reflection before and after doping. This concluded that the doping process did not affect our surface dramatically.

70
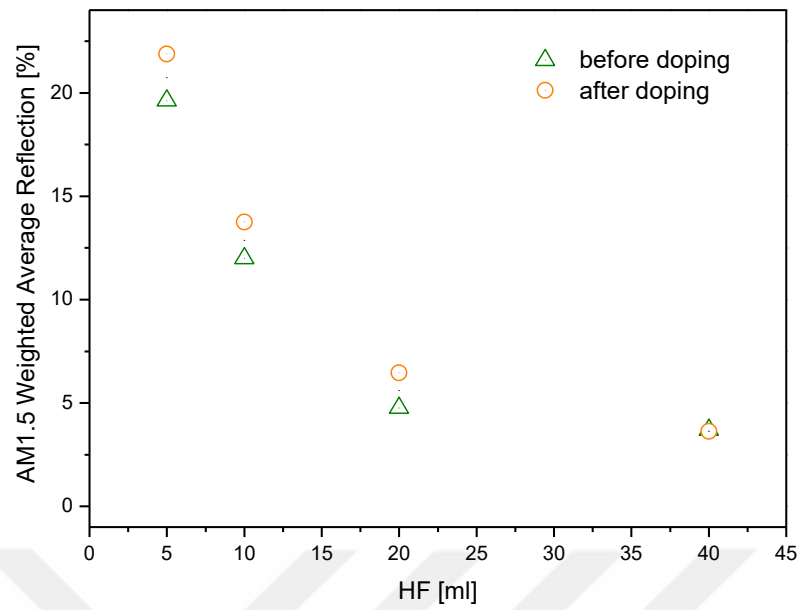
Figure 61 Average reflection of the surfaces before and after doping. The effect becomes more negligible with increased HF concentration while has max on lowest HF. On the other hand, as observed from the reliability chapter, this values stand in the tolerance region of each process and the difference may not be attributed to doping oxidation as well.

SEM images of the surface before and after doping are given in Figure 62. As observed from the reflection, there was not a dramatically change in the surface structure therefore it can be concluded that the surface is damage proof for doping process.
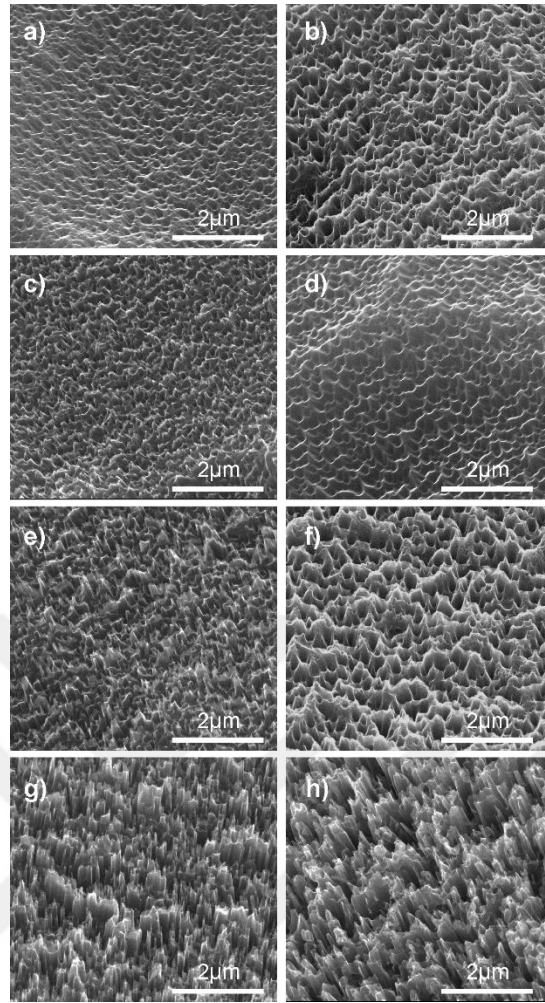
Figure 62 SEM images of the surface before (left column) and after doping (right column). HF concentration increases from top to bottom each row corresponding to one specific concentration

5.2.3.3.   Passivation results

Passivation of the surfaces was conducted by thermal dry oxidation, PECVD SiN_X deposition and fast firing of each set of samples for different KOH smoothing times. Thermal oxide was grown in a vacuum furnace at 850°C for 30min. under O_2 flow. Fast firing was conducted in conveyor belt furnace with a peak temperature of 950°C under ambient atmosphere. Results are given in Figure 63.
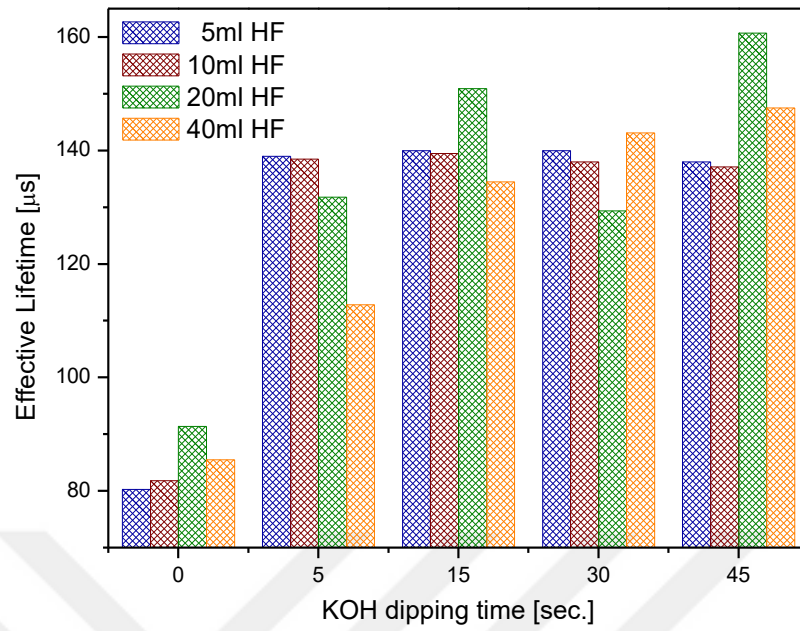
Figure 63 Effective lifetime measured by QSSPC method at an injection level of $10^{15} cm^{-3}$.

It was observed that all samples followed the same increase in surface passivation with increased KOH etching time. On the other hand, in between each texturing recipe, there were not a systematical difference. This concluded that the applied passivation would be useful for each type of texturing when at least a 5 seconds of KOH dip was applied.

5.2.4. Effect of temperature and light

A temperature controlled acidic bath illuminated with a halogen light source is used to see the effects of temperature and illumination on the etch process. The parameters used are tabulated below (Table 6).

Wafer Type	Illumination	Temperature [°C]	HF [ml]
-	-	5	5
p	Dark	10	10
n	90mW/cm^2	15	20
mc (p)	450mW/cm^2	20	40

First, it was observed that the main trend of the etching with respect to HF amount was conserved as seen in Figure 58 and Figure 64
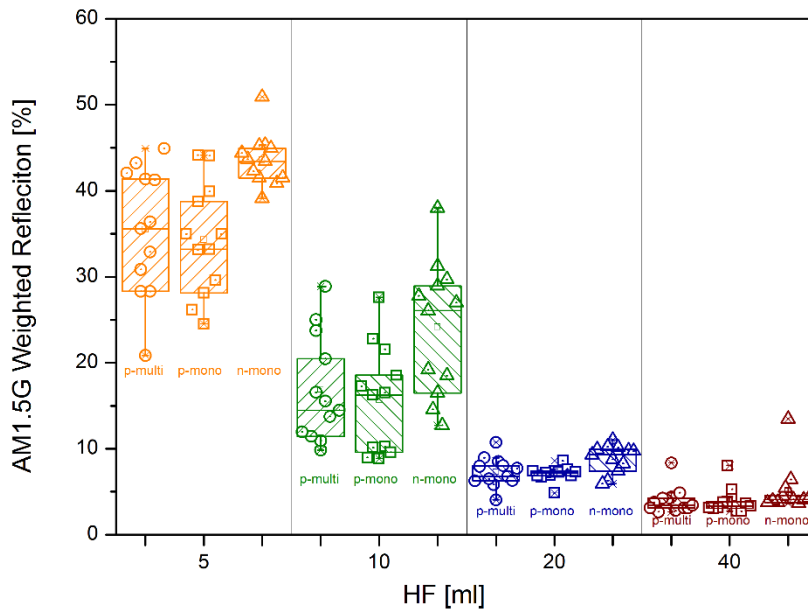
Figure 64 Effect of HF on the average reflection of the samples. Effect of temperature and light are averaged.

On the other hand, for all HF concentration, n type wafers gave higher reflection. P type multi and mono crystalline wafers resulted in similar reflection values which concluded that the reflection is not affected by crystal orientation when averaged.

74

However, from all other experiments, regarding the difference of ambient light and solution temperature, no correlation was observed. Instead, the results were in the tolerance limits of the measurements. This concludes that the process can be done at any temperature between 5-20°C at dark or illuminated ambient with repeating results.

5.2.5. Effect of Starting Surface

For mono-c silicon cell production, first, an etching step is conducted in order to remove the saw damage during the wire cutting of the wafers[164]. However, multi-c, this step is avoided since the acidic texturing requires a rough surface for initiation.

In order to check the effect of the starting surface, we applied one of our optimized recipe (10ml of HF) to a saw damage etched and as cut wafer. Process was done for 60 minutes to see if the longest process could remove the damage during the texturing. Reflection measurements and SEM imaging were done for the analysis of the process. Figure 65 shows the SEM images of the as cut and saw damage etched surfaces textured with MAE. It is clear that a saw damage etching step will be required since the micro cracks due to wire cutting can easily be seen on textured surface. On the other hand, we can see from reflection spectrum that nearly same optical performance was observed for both cases Figure 66.
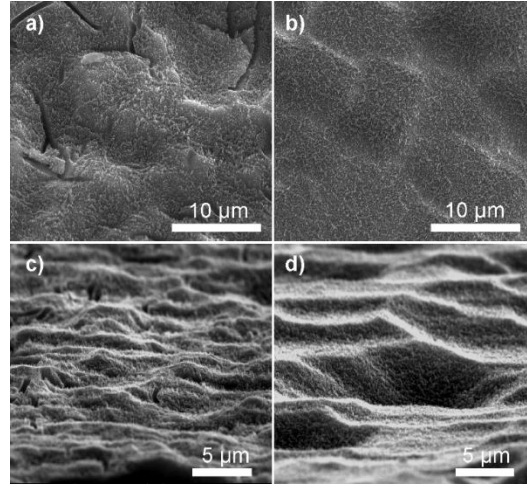
Figure 65 Surface structure of the samples, images taken at 45° elevation for a) and b). 75° for c) and d). the left column shows texturing on as-cut surface while the right column shows on saw damage etched surface.
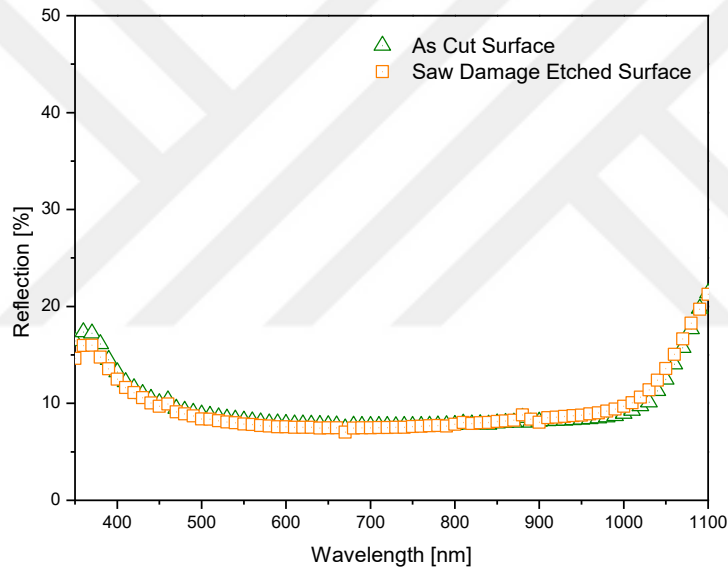
Figure 66 Reflection spectrum for both cases of texturing. Nearly no difference is observed. Hence optically, using as-cut wafers is acceptable.

5.3. Direct & Diffuse Reflection, Transmission and Absorption results

For the last step of characterization, reflection (direct and diffuse), transmission and absorption properties of the samples were measured. In order to be able observe transmission data, wafers were thinned down to 50µm in a 20% (wt) KOH solution at 80°C for 50min. Measurements were conducted in an integrating sphere setup that has

two modes of operation for reflection measurements, one is the diffuse mode where only scattered light due to surface texture is measured and the other is the total reflection mode where total reflection is measured (Figure 67). Total reflection is sum of diffuse and specular component in which specular corresponds to the reflection from the surface such that incoming and reflected light make equal angle with the surface normal (eqn. 11).
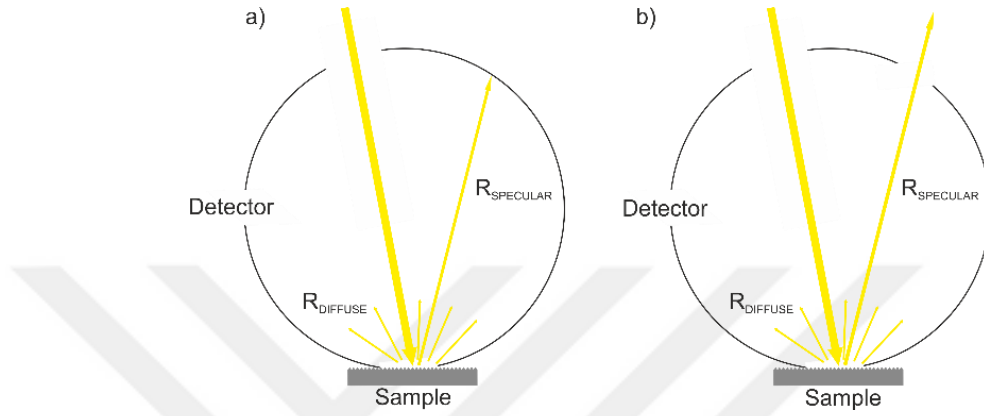
Figure 67 Measurement setup for reflection with a) total reflection configuration and b) with diffuse reflection configuration.

$$R_{Total} = R_{Diffuse} + R_{specular}$$ *eqn. 11*

First of all, reflection from the surfaces are given in Figure 68, Figure 69 and Figure 70. The total reflection follows the expected trend with bare wafer having the highest reflection and texturing with 40ml of HF yields lowest reflection. On the other hand, when we check the diffuse reflection, we observe a 10% absolute decrease in bare Si reflection while we do not see a significant change in textured samples. Therefore, we can calculate the bare sample to have nearly 10% of direct component while for nano textured samples, the value gets close to zero with increased HF content (Figure 70). This brings the conclusion that the nano textured samples nearly reflects all incoming directional light as a perfect diffuser. Even though this reflection is not a measure of optical performance itself, we can indirectly conclude that the surface textures act as scattering structures that can help light trapping when placed on top of the wafer and will definitely help light scattering when place on the bottom of the cells.

77
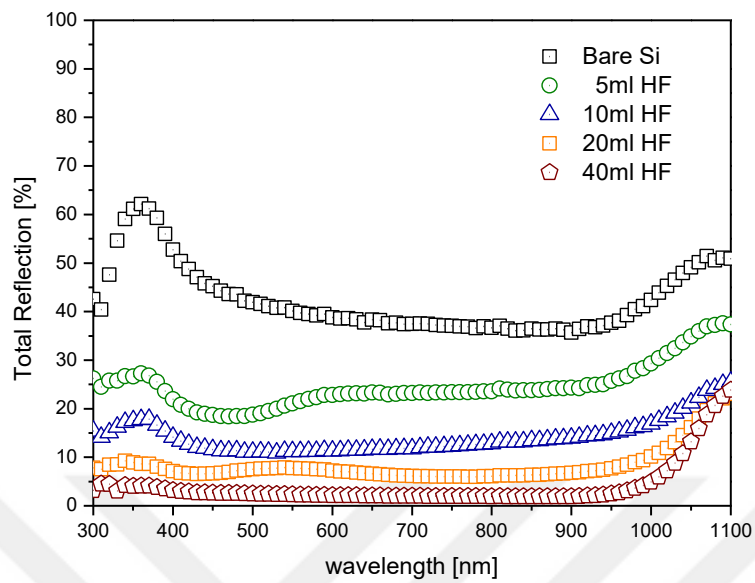
Figure 68 Total reflection from the surface of the textured and bare Si.
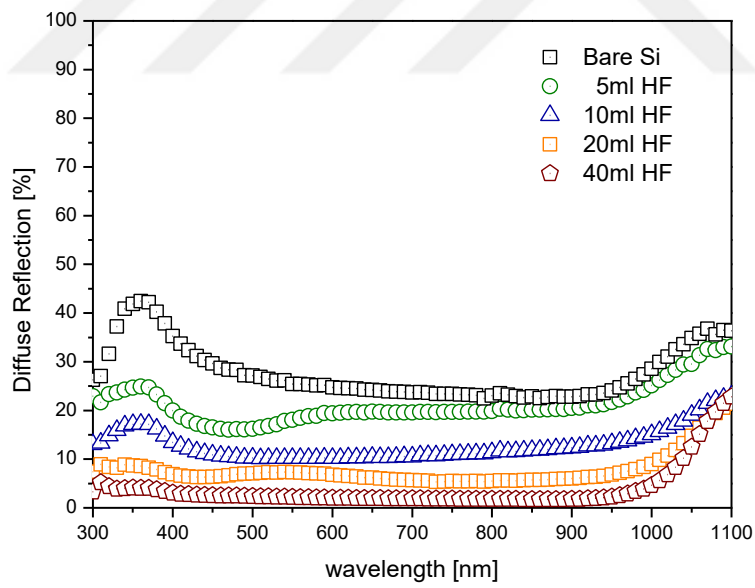
Figure 69 Diffuse reflection from the surface of the textured and bare Si.
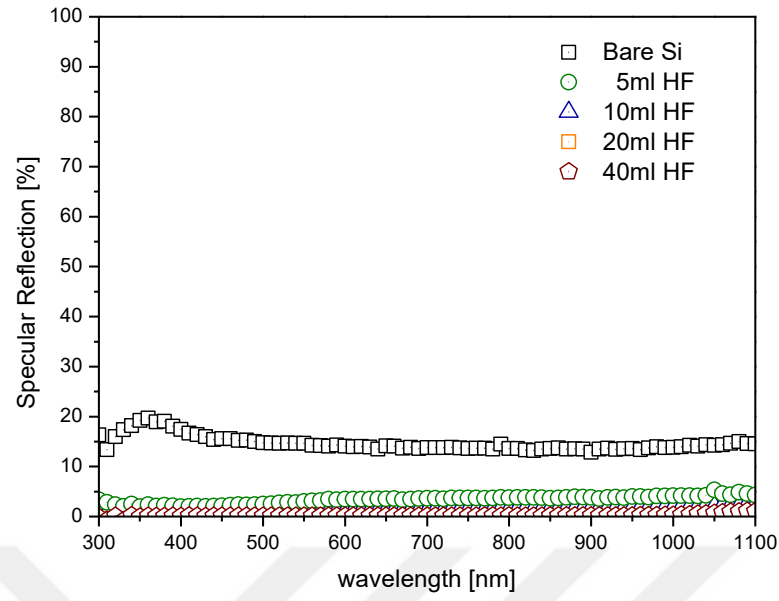
Figure 70 Specular reflection from the surface of the textured and bare Si.

As discussed above, reflection alone cannot be used as a tool for determining the optical performance of the texturing structures. Since the cell needs to absorb photons for e-h pair generation, measurement of absorption is of interest for full characterization. To extract absorption, transmission from the surface is measured and then Absorption is calculated through the formula:

$$A = 1 - T - R$$

eqn. 12

Measured transmission spectrum are given in Figure 71. We observed that increased HF lead to lower transmission after 800nm. Absorption spectrum is given in Figure 72.
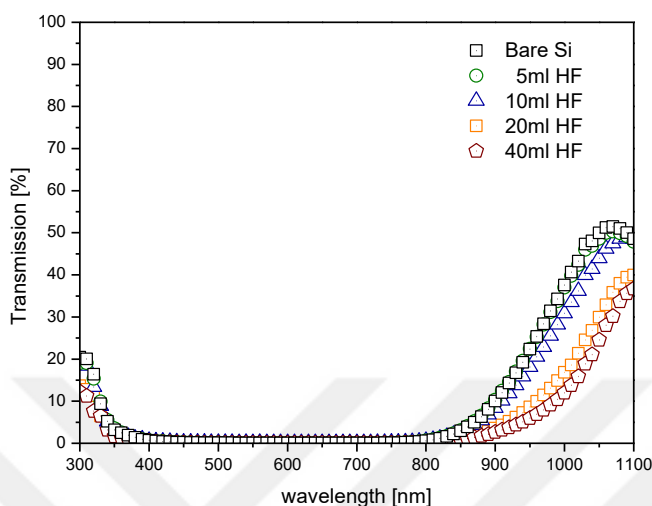
Figure 71 Transmission for the textured and bare Si samples.
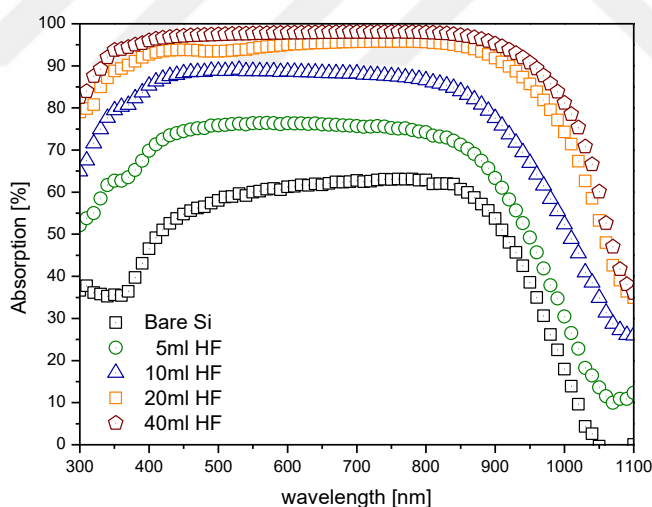
Figure 72 Absorption for the textured and bare Si samples.

We observed from absorption that the highest HF content texture absorbs a very large portion of the spectrum while bare Si with the same thickness can only have nearly half performance. In order to get a better understanding, we calculated the J_{SC} loss bare

and textured samples with a thickness of160 and 50µm respectively as given in Figure 73 where we assume an internal quantum efficiency of unity for each wavelength. As expected, bare Si loses half of the current present from the sun while the textured sample just has 3,7mA/cm^2 loss without any ARC.
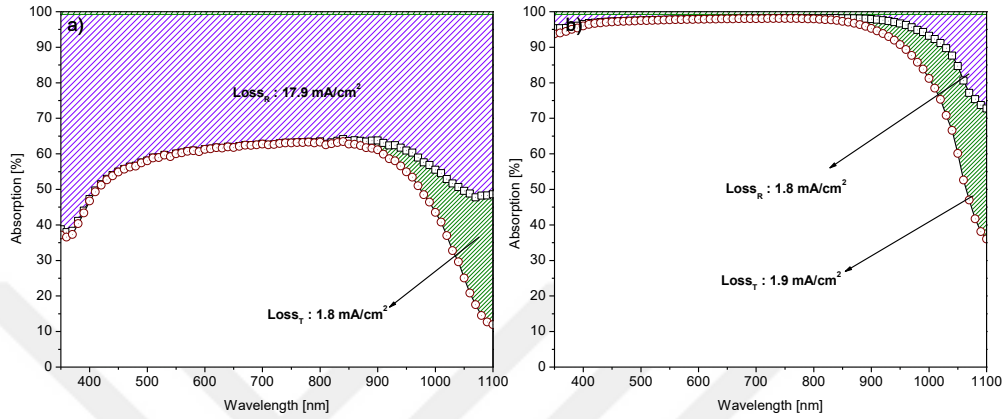
Figure 73 losses induced by reflection and transmission for a) bare silicon 160µm and b) nano textured 50 µm silicon with 40ml of HF

When the calculation is performed for all texturing recipes and the losses are compared between 50µm and 160µm samples with same texturing, we observed that for 20ml of HF, the difference of J_{SC} is only 0.6mA/cm^2. On the other hand, in total, if we compare a sample textured with 40ml of HF and a bare wafer both at 50µm thickness, we observe a 16mA/cm^2 enhancement, nearly 40% of the J_{SC} limit for single junction c-Si solar cells(44.23mA/cm^2) [165].
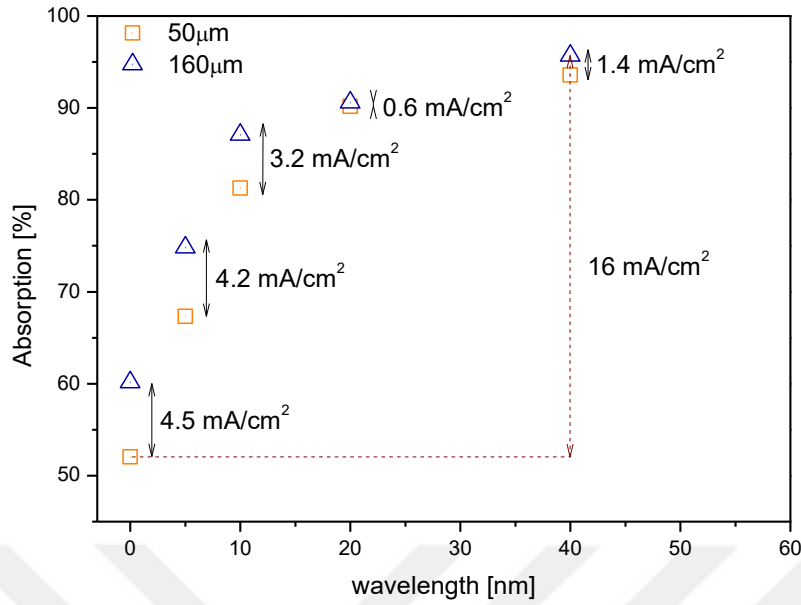
Figure 74 AM1.5G weighted absorption of samples with nano texture and bare Si with thickness of 50µm and 160µm. J_{SC} calculations were also given as difference for each sample assuming an IQE of unity.

5.4. Conclusion

In this chapter, optimization studies for a nano texturing recipe using MAE was discussed. Addition of HNO_3 resulted in control of surface structure morphology ranging from nano-wires to nano-cone like texture. Chemical concentrations for MAE process has been varied and best working 4 recipes has been chosen as candidates for cell texturing with solutions consisting of 200ml of DI water, 50ml of HNO_3, 50mg of $AgNO_3$ and 5ml, 10ml, 20ml and 40ml of HF respectively. In addition, cell processes such as solid state diffusion have been applied and no effect was observed after this high temperature oxidation step on the optical performance. Re-usability of the chemical for industrial applications was tested and two of the recipes was proven to be very reliable. Structure of the starting surface did not affect the optical properties while SEM images revealed that a saw damage removal step was necessary. Passivation studies showed that a short KOH dip was very useful for better passivation of the surface. Effect of wafer type, illumination and temperature have been investigated.

Multi-c and mono-c p type wafers resulted in similar performance while n-type samples had higher reflections. On the other hand, effect of illumination and temperature was not observed throughout the experiments. In the end, absorption enhancement has been calculated and it was observed that the texturing process lead to very high optical performance even for 50μm thick c-Si wafers having comparable J_{sc} potentials to 160μm thick samples.

CHAPTER 6

APPLICATION OF MAE WITH HNO$_3$ AS A HOLE INJECTION AGENT TO SOLAR CELLS AS A TEXTURING METHOD – NANO-TEXTURE ON MONO CRYSTALLINE SILICON

6.1. Introduction

Nanowire texturing which results in a 'black Si' texture has problems related to recombination and doping due to geometrical structures of the nanowires (very high surface area and dimensions smaller than the junction depth) [91][166]. In order to solve this generic problems of NW black Si texture, MAE with HNO$_3$ as a hole injection agent which has been optimized in terms of geometrical, optical and passivation properties has been applied to mono-c silicon solar cells as a surface texturing method[156]. Passivation via SiO$_2$/SiN$_X$ stack has been used in order to approve industrial applicability together with screen printed metallization. Optimization of doping and contact firing resulted in cells with better performance than the reference pyramid texture.

6.2. Experimental

For solar cell production, 1-3Ωcm, p type boron doped, CZ grown mono-c silicon wafers with a thickness of 180μm were used. The process flow is given in Figure 75. Wafers first went through an etching to remove saw marks in 20% KOH at 80°C for 2 minutes. After etching, DI rinsing and HF:HCl cleaning of SiO$_2$ and metallic

impurities from the surface was applied followed by rinsing again. In this step, wafers were divided into two sets. First set was textured in a solution of 3.7% (wt.) KOH and 3.7% (wt.) IPA for 45 minutes at 75°C for random pyramid texture formation. Then wafers were cleaned in HF:HCl and rinsed in DI water. Second set went through a MAE step consisting of a solution with 1000ml of DI, 250ml of HNO_3, 100ml of HF and 0.25g of $AgNO_3$. Texturing was completed in 60 minutes and was followed by and HNO_3 removal of the Ag dendrites, DI rinsing, HF:HCl cleaning and rinsing again. After this step, all sets went through the same process steps. First and RCA2 cleaning procedure was applied to remove any metallic contaminant from the surface. This was followed by a DI water rinse, HF:HCl clean, DI water rinse and hot N_2 drying step. Textured and cleaned samples were doped by solid state diffusion. PSG formed on the surface was cleaned by HF:HCl clean and DI rinsing. Subsequently, another RCA_2 was applied to remove any metal contamination during the doping process followed by HF:HCl dip, DI rinsing and hot N_2 drying. Clean wafers were passivated by thermal oxidation at 850°C for 30 minutes under O_2 flow in order to grow an 8nm of SiO_2 layer. This was followed by PECVD SiN_x deposition, screen printed metallization and firing. Finally edge isolation was performed by cutting the samples into small pieces mechanically. I-V measurements were conducted under class AAA calibrated AM1.5G flash simulator. Reflection and EQE measurements were conducted with an integrating sphere - monochromator setup.
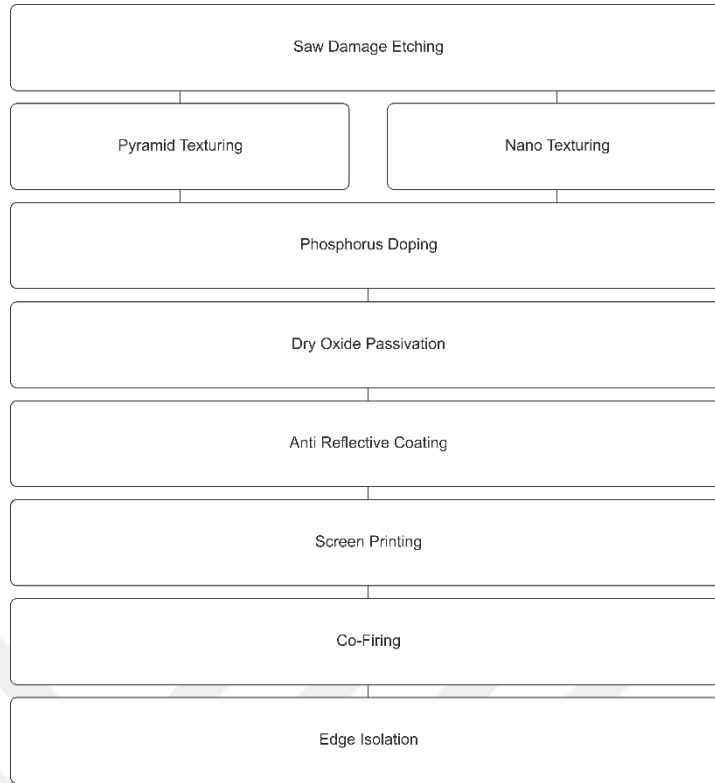
Figure 75 Process flow for nano and pyramid textured mono-c Si cell production

Contact resistance measurements were conducted by measuring the resistance between two fingers with changing pitch and extrapolating the pitch to zero to find contact resistance.

Finally, series resistance free I-V characterization was conducted via Sinton Suns-V_{OC} tool to extract the pseudo fill factor and shunt resistance values.

6.3. Results

Figure 76 shows the average reflection for 4 set of samples that have been elected through 120 different sets due to their optical and morphological properties (Chapter 5). It is clear that sample with the lowest concentration of HF has an average reflection greater than pyramidal texture hence is not suitable as an alternative to reference set.

On the other hand, highest HF concentration sample gave very low reflection while having a very nanowire like form which was proved to be in-effective in Si cell texturing through Chapter 3 and Chapter 4. When medium concentration of HF solutions are taken into consideration, we can definitely say that optical performance are negligibly close while solution reliability for higher amount of HF was better (Chapter 5). Therefore, solution with 200ml of DI water, 20ml of HF, 50ml of HNO_3 and 0.05g of $AgNO_3$ has been chosen for use in mono-c silicon texturing.
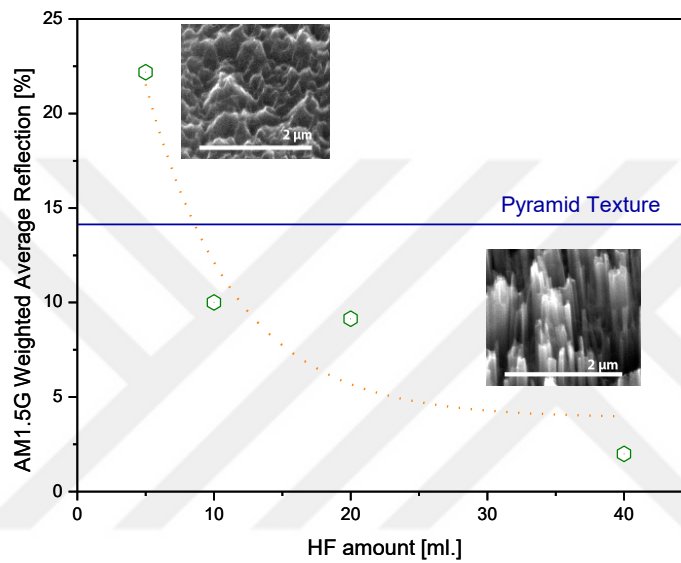
Figure 76 Average reflection for the samples with changing HF concentration. Pyramid textured samples average reflection was inserted as a reference for comparison. SEM images of highest and lowest HF content are also inserted into the graph

88

SEM images of the nano textured and pyramid textured samples are given in Figure 77 a) and b) respectively. We observe nano texture and pyramid formation to be succesfull for both cases.
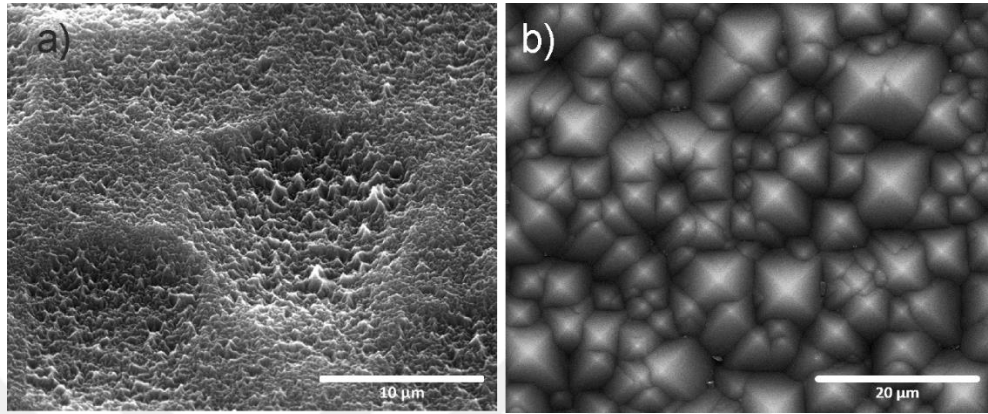
Figure 77 a) nano textured surface and b) pyramid textured surface.

Pyramid textured sample has been coated with 80nm of SiN_X as an anti reflective and passivating film. On the other hand, surface of the nano textured sample has been coated with changing SiN_X thickneses to observe the optical properties. The results of different SiN thickneses are given in Figure 78. It was shown that a dramatic reduction of reflection is observed for all sets of nano texture and pyramid textured sample. For nano texture, 80nm of SiN gave the lowest value as for the case in pyramid texture always. Therefore 80nm of SiN has been chosen to be the best option for cell processing with nano texture.
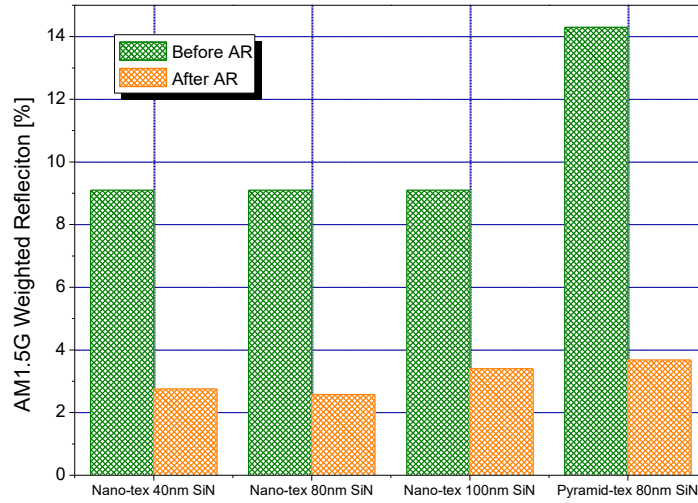
Figure 78 Average reflection for samples with nano and pyramid texturing. Nano textured samples have different SiN thicknesses while for pyramid textured sample, 80nm has been used as reference.

First, a set of samples with standardized doping process which was optimized for pyramid texture has been applied to nano textured samples. Resulting samples had very low blue response to incoming light which can be seen from IQE spectrum shown in Figure 79. The results indicated a high recombination activity which may be result of a very thick emitter. Since SIMS or ECV measurement of dopant depth was not possible, in order to extract the junction depth, PC1D5 simulation of the cell was conducted[167]. Parameters used for the cell are listed in Table 7. Simulation was run with the parameters given in Table 7. They were kept constant and the junction depth was varied until a good fit with measured IQE is observed which is given as solid line in Figure 79. The fitting was acceptable for a junction depth of 2.45µm. However, expected junction depth was on the orders of 0.5µm for a pyramid textured surface.
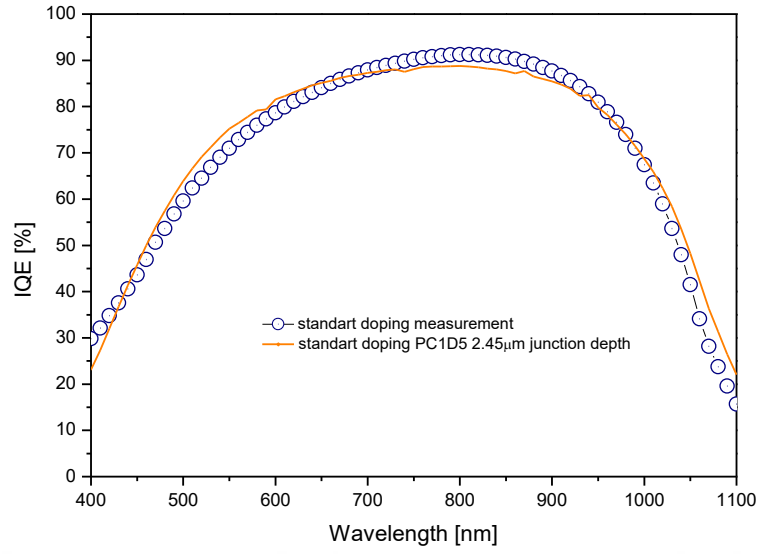
Figure 79 IQE spectrum measured from nano textured sample with a doping process optimized for pyramid texture. Data points are measurements while solid line is simulated IQE curve.

Table 7 PC1D5 simulation parameters used to extract the doping depth of the nano-textured samples

Parameter	Value
Cell Thickness*	160 μm
Base Contact Resistance*	1.0174 Ω
Internal Shunt Element*	4.37e-7 S
P type background Doping (Boron)*	9.787e15 cm^{-3}
Front Doping Peak (Phosphorus)**	1.099e20 cm^{-3}
Front Doping Profile*	Erfc
Bulk τ_n*	30 μs
Bulk τ_p*	30 μs
Front Surface Recombination Velocity S_n	2.94e6 cm/s
Front Surface Recombination Velocity S_p	2.94e5 cm/s
Back Surface Recombination Velocity S_n	500 cm/s
Back Surface Recombination Velocity S_p	500 cm/s

The reason for this difference is suggested to be a result of the surface nano-structures which have dimensions of the orders of diffusion depth. When a pyramid textured surface is doped by solid state diffusion, the surface of a pyramid can be considered as a flat structure (Figure 80).

91
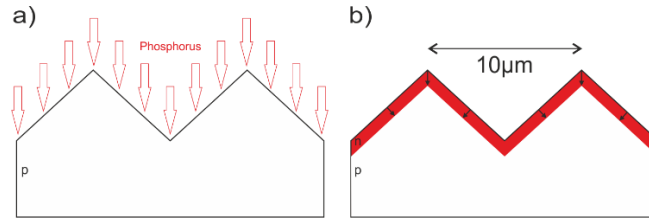
Figure 80 Doping of a pyramid textured surface a) during diffusion, b) after n emitter formation. Since the size of the structures are much larger than the junction depth, a conformal and homogenous depth junction is formed.

On the other hand, if the surface structures are of the orders of junction depth there is the possibility of doping to reach at the same point of the wafer from different surface normal. This would result in an effective doping with a larger depth (Figure 81).
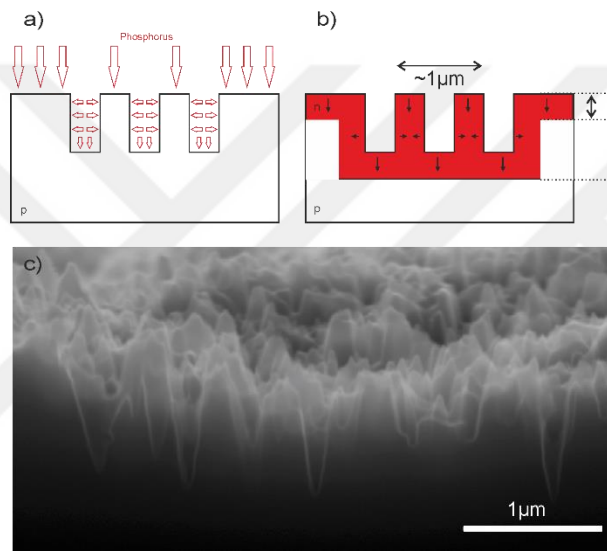
Figure 81 Doping of a nano textured surface a) during diffusion, b) after n emitter formation. Since the size of the structures are of the order of the junction depth, an effective junction depth larger than actual diffusion is expected

As discussed elsewhere, decreasing the junction depth would result in an enhancement of collection efficiency since the effective junction depth will be closer to the expected junction depth [94]. A 20°C temperature decrease in pre-deposition step was applied to decrease the solubility of phosphorus in Si together with different drive-in durations for the best cell performance. The IQE of the sample with the highest efficiency from this set is given in Figure 82.
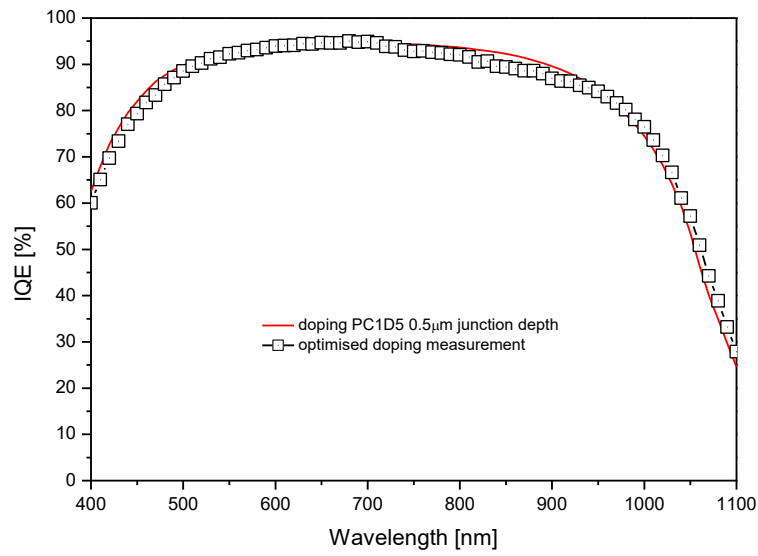
Figure 82 an increased blue response was observed for decreased doping temperature which fits well with a PC1D5 simulation of 0.5µm junction depth solar cell.

Of course, changing the doping process results in a different emitter profile which needs an optimization of contact formation by firing. For this purpose, nano-textured samples with the new doping recipe was screen printed with standard fingers and TLM measurements were conducted to find the contact resistivities for different firing parameters. Results are shown in Figure 83.
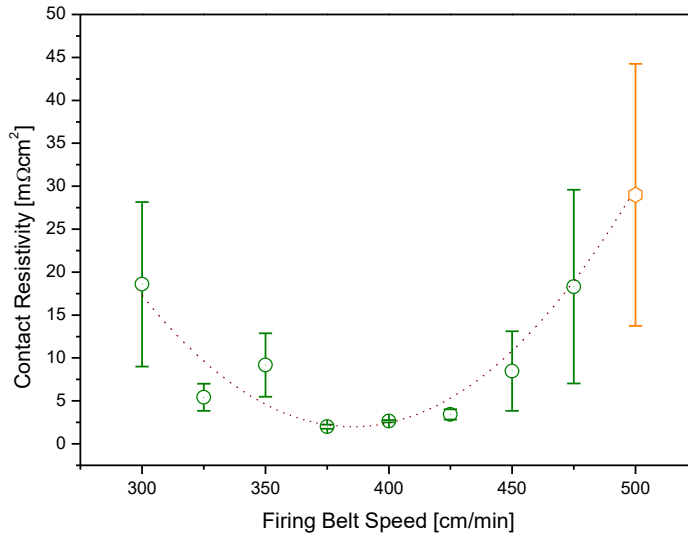
Figure 83 Contact resistivities of Ag on Si for nano-textured samples fired at 925°C for various belt speeds. Value used for pyramid textured standard doped sample is given as an orange data point.

It is clear that a decreased surface doping required a slower belt speed so that the thermal budget is increased and contact formation was successful. Therefore, 375-400cm/min belt speed is chosen as the optimum firing parameter while for standard doped pyramid textured samples, the recipe is at 500cm/min.

The doping with 20°C less temperature also includes a drive in step which is 16 minutes for standard recipe. In order to decrease the depth of the junction, 8 minutes and no drive-in samples were also prepared. Minority carrier lifetime values measured by QSSPC method for different emitter profiles are given in Figure 84. The resulting cell parameters for changing firing belt speeds and drive in durations are given in Figure 85.
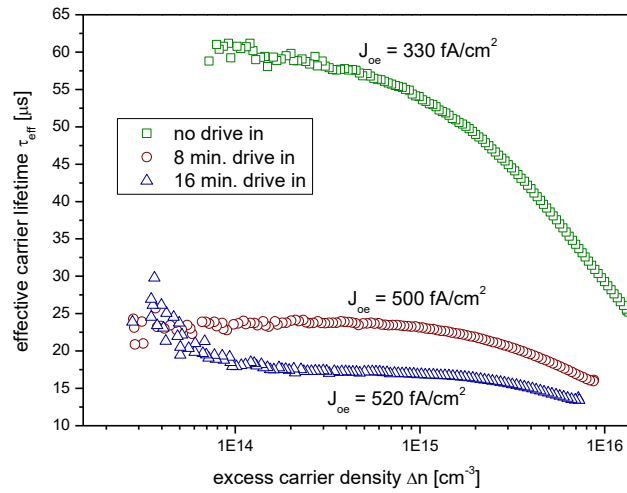
Figure 84 effective carrier lifetime and J_{0e} extracted by QSSPC measurements for three different doping parameters.
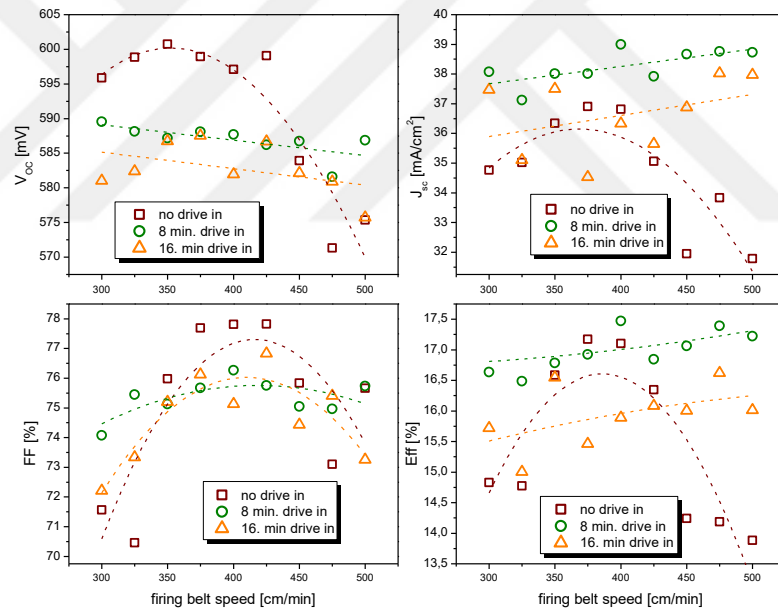
Figure 85 Cell parameters for different drive in and firing belt speeds. Dashed lines are visual aid only

Lifetime and J_{0e} measurements claim that no drive in sample would result in highest performance in terms of V_{OC} due to decreased recombination. Figure 85 also confirms this results. On the other hand, samples with higher durations of diffusion shows a

linear open circuit voltage – firing speed dependence while no drive in samples possess a maximum. This behavior is attributed to vulnerability to shunting of the samples with no drive in for lower belt speeds due to shallower junction depth and higher thermal budget. For high speeds, the effect is related to insufficient BSF formation and contacting problems that lower the FF also.

In the end, the parameters of 8 minutes drive-in and 400cm/min firing belt speed was chosen since they resulted in higher efficiency. A new cell with those parameters were fabricated together with a standard pyramid textured sample. Resulting cells' j-V curves are given in Figure 86.
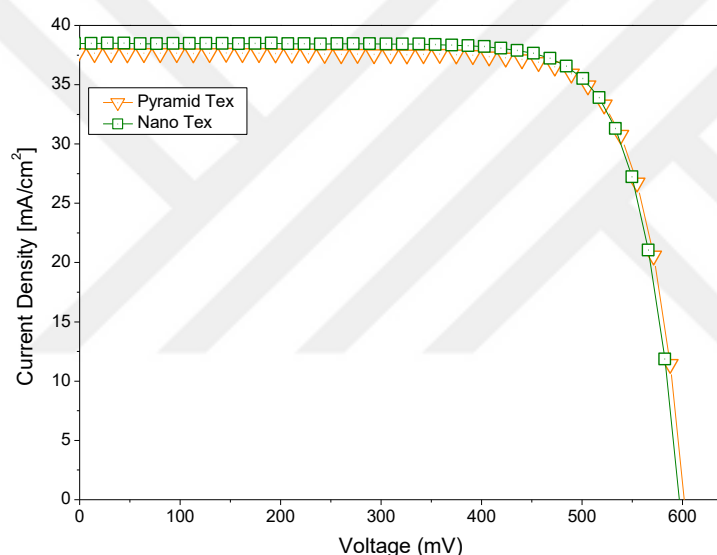
Figure 86 j-V curves of the reference and nano-textured sample

Cell parameters are given in Table 8. An increase of 0.9mA/cm^2 in J_{SC} was observed together with an increase of 0.1% absolute efficiency for nano-textured samples. On the other hand, V_{OC} was lower, stating a need for better passivation for nano-textured samples.

Table 8 Cell parameters for nano-textured and pyramid textured cell

	i-Voc [mV]	Voc [mV]	Jsc [mA/cm2]	p-FF [%]	FF [%]	p-Efficiency [%]	Efficiency [%]	Rseries [mΩcm2]
Nano	604	597	38.5	80.7	77.52	18.74	17.80	808
Pyramid	608	601	37.6	80.9	78.30	18.51	17.71	791

6.4. Conclusion

The optimized surface texturing recipe with HNO_3 as the oxidative agent has been applied to mono-c silicon solar cell production sequence together with pyramid texture as reference. Low blue response has been identified and simulations indicated that a deep junction depth is the reason as a result of surface texture geometry. Through optimizations on doping, and metallization of the cells, efficiencies 0.1% higher that pyramid texture has been observed with increased J_{SC} as expected. This proved the process to be an alternative to mono-c Si texturing by pyramid formation, especially a high performance low cost alternative for thin crystalline Si solar cells.

CHAPTER 7

APPLICATION OF MAE WITH HNO$_3$ AS A HOLE INJECTION AGENT TO SOLAR CELLS AS A TEXTURING METHOD – NANO TEXTURE ON MULTI CRYSTALLINE SILICON

7.1. Introduction

Development of multi-c Si growth and wafering technology results in higher efficiency, low cost cells [156,168,169]. Among those, diamond wire cut wafer, decreasing the material loss, is a popular approach [170]. Main drawback of this technology is that it results in a surface very smooth compared to slurry based wafering techniques. For mono-c wafers, diamond wire cut does not possess a problem since texturing method is not affected by the starting surface structure[171]. On the other hand, for multi-c texturing, standard iso-texture taking the advantage of the roughness of the slurry cut surface is not applicable for the case of diamond wire cut wafers [172,173]. Alternative methods have been proposed for texturing diamond cut multi-c wafer such as laser texturing, chemical vapor texturing and MAE[173–176]. In this study, MAE with HNO$_3$ addition that has been optimized is applied to multi-c silicon wafers for texturing. Wafers with saw damage etched surface has been used because they resemble the diamond cut surfaces. For reference, standard iso-texture has been applied to as cut wafers. Cell process was completed with all standard production techniques and 0.9mA/cm^2 J$_{SC}$ gain together with 0.6% absolute efficiency gain was observed.

7.2. Experimental

For cell production, 1-3Ωcm, boron doped p-type multi-c wafers with a thickness of 200µm has been used. Wafers were divided into two sets for texturing purposes in the beginning. Reference set was directly textured in a solution of $HF:HNO_3:H_2O$ with a concentration 15:1:1 for 60 seconds. After texturing, wafers were rinsed in DI water and a short KOH (1% wt.) dip was performed to remove porous Si formed on the front surface. MAE samples first went through a saw damage etching step in a 20% (wt.) KOH solution for 2 minutes at 80°C. This step resulted in a smooth surface which is not suitable for iso-texture. After saw damage etching, a rinsing, RCA2 cleaning, rinsing, HF:HCl dip and rinsing sequence was applied to remove any metal contaminations from the surface. Then wafers were MAE textured in a solution of $HF:HN_3:H_2O$ with a ratio of 2:5:50 and $AgNO_3$ 0.02% (wt.). Textured samples were cleaned in HNO_3 for removal of Ag dendrites. Subsequently, MAE and isotropic textured samples went through another RCA2 cleaning, DI rinsing, HF:HCl dip, DI rinsing and hot N_2 drying steps to get ready for emitter formation. Solid state diffusion was conducted with the optimized recipe of Chapter 6. Doped samples went through another HF:HCl, DI, RCA2, DI, HF:HCl, DI and hot N_2 drying step. After PSG removal, samples were passivated by dry oxidation and PECVD SiN deposition. Front Ag grid and rear full Al metallization was formed by screen printing. Fast firing was used to form Ag fire through contacts and Al:BSF and wafers were cut mechanically into small pieces for edge isolation (Figure 87).
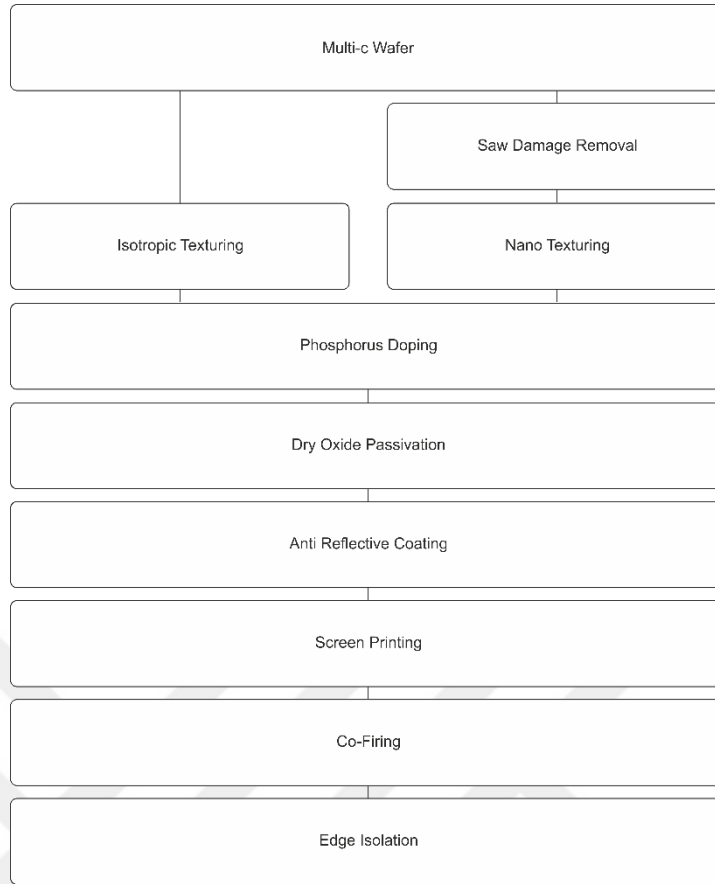
Figure 87 Multi-c Si cell process flow for nano and iso textured samples

Cell efficiency was measured by an AM1.5G weighted Class 3A flash solar simulator. Reflection and EQE was measured through an integrating sphere – monochromator setup and surface structures were examined by scanning electron microscopy.

7.3. Results

SEM images of the surface of nano textured samples are given in Figure 88. It was observed that in micro scale, the formation of the nano-texture was successful and on macro scale, differences in direction of surface normal due to anisotropic property was clear. The anisotropy of the etching was discussed elsewhere and is attributed to difference in the speed of oxidation and etching due to bond density of specific crystal planes[114][115][143].
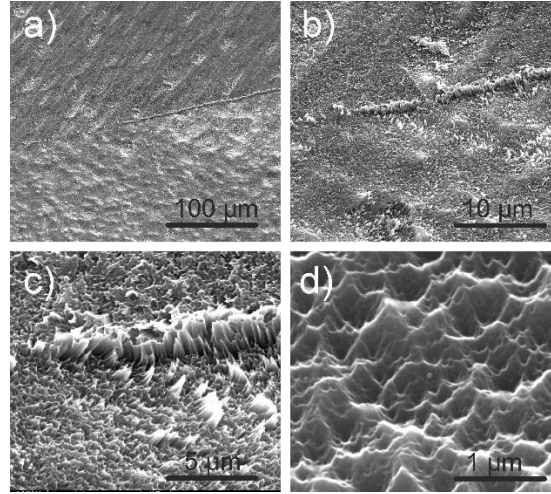
Figure 88 SEM images of the nano textured samples with different magnifications

As in the case of mono-c nano-texture, nano cone shaped structures were formed as a result of the optimized MAE recipe with HNO_3 addition. Average reflection from the surface for reference and nano-textured sample can be seen in Table 9. Optically, MAE textured showed better performance as expected. The reflection measurements were conducted from a large area of the wafer ($5cm^2$) hence the effect of different crystal orientations has been averaged since a single domain has sizes of $0.1cm^2$ – $1cm^2$.

Table 9 Weighted reflection from the surface of the nano textured and iso textured samples after SiN coating.

Texturing Method	AM1.5G Weighted Reflection [%]
MAE	3.53
Isotropic	4.03

Figure 89 shows the IQE and R spectra of the samples with nano and iso texturing. The reference cell has a better blue response as in the case of mono-c samples, which is attributed to lower surface recombination on micro structures, but in total, the reflection difference is with the main reason for the calculated J_{SC} difference of $0.8ma/cm^2$. Throughout the rest of the spectrum, both texturing methods worked well with similar optical and electronical performances. This brings along the conclusion that the nano-textured sample has an advantage in high energy side of the spectrum which may not be completely reflected to the real cell performance due to difference in IQE.

102
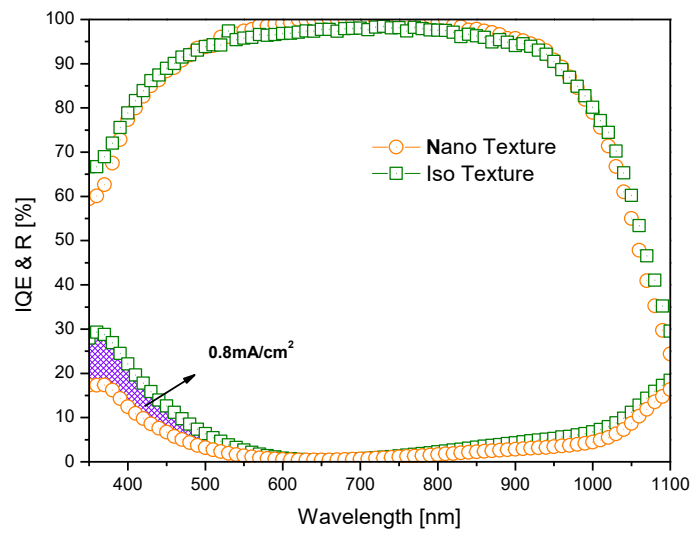
Figure 89 IQE and R spectrum for the cells with nano and iso texturing.

Finally, cell results for both kind of texturing are given in Figure 90. We observed an increase of 0.9mA/cm^2 for short circuit current density together with a 0.6% absolute efficiency gain.

	V_{OC} [mV]	j_{SC} [mA/cm^2]	FF [%]	η [%]
Nano	622	37.1	74.7	17.2
Iso	619	36.2	74.1	16.6
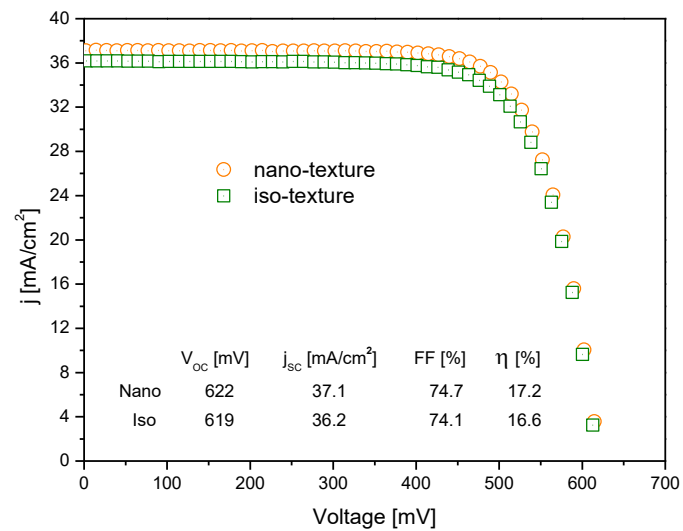
Figure 90 Light j-V curves of the samples with nano and iso texturing

7.4. Conclusion

In this chapter, application of our new and optimized nano texturing recipe to multi-c silicon solar cells is presented. Iso textured samples have been used as reference for which the texturing process was applied directly on as-cut wafers. On the other hand, for nano-textured samples, saw damage etched smooth surfaces were used. This proves the applicability of the optimized recipe to diamond wire sawn multi-c wafers for which a standard technique has not been established yet. In the end, it was shown that the samples with nano-texture resulted in higher current densities and efficiency values compared to reference structures.

CHAPTER 8

CONCLUSION

'I have no idols. I admire work, dedication and competence.'

Ayrton Senna

Silicon, as one of the most abundant elements in the world, is exclusive when compared to other elemental or compound semiconductors. It has a very stable natural oxide as an insulator and a nearly optimum band gap for optical and electronical use in everyday life in visible range. Last but not least, it can be doped in both polarities with a large variety of resistance ranges. All these material properties turned out a huge interest in research and development of silicon material and device technologies. Since the start of the VLSI age, studies on silicon brought the processing technology to a very mature level enabling any adjustment in device physics and/or geometry with an easy way for the desired output. As a result, nearly all electronic equipment used today somehow incorporates a silicon component such as a MEMS sensor or a read-out circuitry.

PV has been developed as a derivative of microelectronics and always affected by the trends in this technology. The dominance of silicon in microelectronics has been therefore the main driving force for the prevalence of silicon in PV. On the other hand, the main advantages of silicon as a semiconductor material for PV technology are its

convenience for high throughput and low cost which are the important parameters desired besides efficiency.

Indirect band gap of crystalline silicon, which may be a disadvantage as the first, causes poor absorption of wavelengths closer to band gap energy. On the other hand, this nature of c-Si results in very low radiative recombination rates, which is certainly an advantage in PV devices. As the absorption is basically related to device thickness as well as an internal material property i.e. "absorption coefficient", it becomes possible to compensate the transparency of such a specific material by adjusting the former. Increasing the path travelled by a photon inside the semiconductor will also increase the possibility of absorption. This is called "light trapping" and theoretical calculations shows that for crystalline silicon, absorption can be enhanced up to 50 times more by adjusting the path of the light inside the bulk. By perfect light trapping, therefore, a 200µm silicon wafer will have an absorption as high as a 10mm bulk c-Si for the wavelengths close to the band edge. An efficient light trapping will make it possible to us thinner wafer allowing use of less material which is necessary to lower the cost of PV cells. Light trapping does not only help optical enhancement, but also allows usage of lower quality and cheaper material with low diffusion lengths of minority carriers. In summary, a threefold enhancement in the cost per efficiency is expected with a good light trapping scheme that is characterized with enhanced current output by high absorption, enhanced charge collection and cost reduction.

Light trapping in industrial crystalline silicon solar cells is accomplished by surface texturing. The surface features formed after texturing refract light into the cell with various angles to the normal, leading to total internal reflections and hence path enhancement. For mono-c Si, using the intrinsic property of crystal geometry and anisotropic etch properties of alkaline etchants, micro pyramids with (111) surfaces and (100) bases can be fabricated easily through wet chemical process. Pyramid surfaces helps reducing the reflection by directing the first reflected beam onto another pyramid surface and trapping photons in the wafer by randomizing the angle of

incidence. For multi-c Si, since the surface does not have a specific orientation, isotropic etchants are usually used to form micro-structures that enhance light trapping and decrease reflection. In addition, both wafer types can be textured using novel methods such as laser structuring, reactive ion etching, plasma etching, plasmonic or photonic crystal scattering enhancement, and MAE. These methods are all in research level due to the problems in cost, throughput and process integration. Among others, MAE is a strong candidate for industrial applications. The method is a chemical etch process in which a noble metal is used as catalyst to enhance the reaction speed locally. Resulting surface can have very low reflection values, usually called as "black Si". On the other hand, since the structures formed on the surface are of the order of nanometer sizes, their application to thin Si substrates is possible when cost considerations in the future market are taken into account. Main disadvantages of MAE are the use of expensive metals such as Ag, Au or Pt and increased surface recombination losses by area enhancement due to nano-texturing. Since the metals are used as catalysts, theoretically, recycling is possible. On the other hand, passivation and surface structures should be optimized for lowest surface recombination.

Throughout this PhD work, we have carried out extensive studies on MAE and its applications to c-Si solar cells. When nanowires formed by MAE were used as surface texture for mono and c-Si cells, the problems faced were not only about surface recombination but were also metallization and doping related. First, solid state diffusion that resulted in a junction depth of about 500nm led to the formation of completely compensated nanowire structures which turned from p type into n type with heavy doping. This induced very high Auger recombination throughout the wire together with surface and SRH recombinations. As a result, photons absorbed in the first few hundred nanometers from the surface (inside the nanowire) created electron-hole pairs with very low recombination lifetime, which were impossible to be collected. This decreased the blue response of the cells, although the optical properties of the nanowire textured samples were nearly perfect. Secondly, metallization by screen printing was not very feasible, especially for mono-c samples, since the individual nanowires acted as super hydrophobic structures that prevented metal paste

107

to diffuse in between them. Instead, the metal contacts constituted a floating structure on the top of the nano-wires and as an outcome of this behavior the contact area at the tips remained very small and hence destroyed the fill factor. In the end, it was concluded that, though optically black surfaces could be prepared with this method, electrical passivation and contacting issues had to be solved together with dopant diffusion in order to have comparable efficiencies with pyramid or iso texturing. However, proof of concept was demonstrated in large area with uniform coverage of nanowires produced by MAE.

In MAE, oxidation of silicon speeds up under the metal silicon contacts due to the catalytic effect of the metal which in the end accelerates hole transfer from solution to silicon. The oxide formed is then etched by hydrofluoric acid and cause the metal to sink towards the etching direction. When the rate of oxidation under the metal and the rate of oxide etching are equal or etching rate is higher, the oxide formed has a cross-sectional area equal to the metal-silicon contact area. In this case, nano-wires or nano-holes are formed. On the other hand, if the rate of oxidation is increased and higher than that of oxide etching rate, the holes are swept away from the metal-silicon interface to the sides of the cross sectional area and cause final structures to have inverse tapered conical shapes. Having these structures seem to be more effective since the air-Si interface changes more smoothly for photons and conformal passivation becomes easier. In this thesis, nitric acid was used as a hole injection agent to increase the oxidation rate and adjust the surface structures' geometry. 120 different etching parameters including concentration of HF, HNO_3 and $AgNO_3$ and etching time were studied in detail through SEM imaging and reflection measurements. Parameters that led to nano-wire formation or high reflection were eliminated. Thus, only 8 sets of solution parameters were left to be used in the implementation of the second set of experiments. Recipes of texturing were then subjected to reliability tests to confirm repeatability and industrial applicability. After this experiment elimination of 4 more sets of recipes were required. The last four sets were then subjected to passivation studies and it was observed that a surface smoothing with a dilute KOH dip provided an increase of lifetime. Effect of temperature and light were not been able to be

observed clearly for these sets of wafers that had the surface preferred in the beginning. However, using saw damage etched surfaces was chosen since it was not possible to realize the removal of saw induced damages via etching. Direct-diffuse reflection and transmission measurements were conducted for thick and thin wafers and absorption was calculated for each case. It was observed that absorption enhancement was enormous for thinner samples that corroborated the potential of the process for industrial applications

In order to check the performance of the optimized MAE texturing recipe, mono and multi-c silicon solar cells were fabricated. Even though optical performance was enhanced, collection problems in the blue part of the spectrum persisted. One dimensional device simulations revealed that since the structures had the size of the order of junction depth, again a complete compensation was occurring that resulted in an effective junction depth larger than the actual diffusion of dopants. This high recombination emitters caused loss of blue response. In order to resolve this problem, doping temperature and drive in time were optimized and a shallower junction was achieved to be formed with a better blue response as expected. On the other hand, changed emitter doping required the optimization of the contact formation again. TLM characterization was used to solve the issues related to contact formation and shunting. In the end, mono and multi-c cells with increased efficiency and short circuit current density compared to standard texturing techniques have been attained.

In conclusion, this thesis study proves the applicability of MAE with nitric acid as an oxidizing agent for texturing mono and multi crystalline silicon solar cells which are processed with commercially applicable passivation techniques as well as its effect on enhanced cell performance. Parameters related to etching solution were optimized in conjunction with the requirements of cell fabrication in order to exploit the enhanced optical performance of the black Si texture used effectively. For future studies, the technique can be further elaborated and adapted to the industrial manufacturing lines. In particular, application to diamond cut wafers, which is becoming a standard in the industry, can be studied in the near future. Other than today's standard passivation

techniques, atomic layer deposition of passivating films such as AlO_X or HFO_X can be used taking the advantage of conformality of ALD. In addition, instead of using silver, nickel can be used since it is an attractive material due to cost considerations and first studies show that it can be used as a catalyst for MAE.

REFERENCES

[1] P.T. Keyser, Aristotle's Physics: A Guided Study Joe Sachs, Isis. 87 (1996) 716–717. doi:10.1086/357668.

[2] E. Cook, The Flow of Energy in an Industrial Society, Sci. Am. 225 (1971) 134–144. doi:10.1038/scientificamerican0971-134.

[3] No Title, (n.d.). ttp://climate.nasa.gov/vital-signs/global-temperature/. Accessed: 2016-06-09. (Archived by WebCite® at http://www.webcitation.org/6i98N8UZt) (accessed June 9, 2016).

[4] A.M.C. Şengör, S. Atayman, The Permian Extinction and the Tethys: An Exercise in Global Geology, in: Intergovernmental Panel on Climate Change (Ed.), Spec. Pap. 448 Permian Extinction Tethys An Exerc. Glob. Geol., Geological Society of America, Cambridge, 2009: pp. 1–85. doi:10.1130/2009.2448.

[5] E. Becquerel, Mémoire sur les effets électriques produits sous l'influence des rayons solaires, in: Comptes Rendus, 1839: pp. 561–567.

[6] W. Smith, Effect of Light on Selenium During the Passage of An Electric Current, Nature. 7 (1873) 303–303. doi:10.1038/007303e0.

[7] W.G. Adams, R.E. Day, The Action of Light on Selenium, Philos. Trans. R. Soc. London. 167 (1877) 313–349. doi:10.1098/rstl.1877.0009.

[8] C.E. Fritts, On a new form of selenium cell, and some electrical discoveries made by its use, Am. J. Sci. s3-26 (1883) 465–472. doi:10.2475/ajs.s3-26.156.465.

[9] D.M. Chapin, C.S. Fuller, G.L. Pearson, A new silicon p-n junction photocell

for converting solar radiation into electrical power, J. Appl. Phys. 25 (1954) 676–677. doi:10.1063/1.1721711.

[10] M.A. Green, K. Emery, Y. Hishikawa, W. Warta, E.D. Dunlop, Solar cell efficiency tables (Version 47), Prog. Photovoltaics Res. Appl. 24 (2016) 3–11. doi:10.1002/pip.2728.

[11] A.S. Blazev, Photovoltaics for commercial and utilities power generation, 2012.

[12] NREL, Efficiency_Chart, Nrel. (2015) 1. http://www.nrel.gov/ncpv/images/efficiency_chart.jpg.

[13] M.A. Green, K. Emery, Solar cell efficiency tables (Version 1), Prog. Photovoltaics Res. Appl. 1 (1993) 25–29. doi:10.1002/pip.4670010104.

[14] M.A. Green, K. Emery, Solar cell efficiency tables (Version 2), Prog. Photovoltaics Res. Appl. 1 (1993) 225–227. doi:10.1002/pip.4670010306.

[15] M.A. Green, K. Emery, Solar cell efficiency tables (Version 4), Prog. Photovoltaics Res. Appl. 2 (1994) 231–234. doi:10.1002/pip.4670020307.

[16] M.A. Green, K. Emery, Y. Hishikawa, W. Warta, Solar cell efficiency tables (Version 3), Prog. Photovoltaics Res. Appl. 19 (1994) 84–92. doi:10.1002/pip.

[17] M.A. Green, K. Emery, K. Bücher, D.L. King, Solar cell efficiency tables (Version 6), Prog. Photovoltaics Res. Appl. 3 (1995) 229–233. doi:10.1002/pip.4670030403.

[18] M. Green, K.A. Emery, K. Bucher, Solar Cell Efficiency Tables (Version 5), Prog. Photovoltaics Res. Appl. (1995).

[19] M. Green, K.A. Emery, Solar Cell Efficiency Tables (Version 8), Prog. Photovoltaics Res. Appl. (1996). doi:10.1002/(SICI)1099-159X(199607/08)4.

[20] M.A. Green, K. Emery, K. Bucher, D.L. King, Solar Cell Eficiency Tables (Version 7), Prog. Photovoltaics Res. Appl. 4 (1996) 59–62.

[21] M.A. Green, K. Emery, K. Bu, D.L. King, S. Igari, Solar Cell Effi☐ciency Tables (Version 9), Prog. Photovoltaics Res. Appl. 5 (1997) 51–54.

[22] M. Green, K.A. Emery, K. Bucher, D.L. King, S. Igari, Solar Cell Efficiency Tables (Version 10), Prog. Photovoltaics Res. Appl. (1997) 3–7. doi:10.1002/(SICI)1099-159X(199707/08)5.

[23] M.A. Green, K. Emery, K. Bücher, D.L. King, S. Igari, Solar cell efficiency tables (Version 11), Prog. Photovoltaics Res. Appl. 6 (1998) 35–42. doi:10.1002/(SICI)1099-159X(199801/02)6:1<35::AID-PIP205>3.0.CO;2-5.

[24] M.A. Green, K. Emery, K. Bücher, D.L. King, S. Igari, Solar cell efficiency tables (Version 12), Prog. Photovoltaics Res. Appl. 6 (1998) 265–270. doi:10.1002/(SICI)1099-159X(199807/08)6:4<265::AID-PIP235>3.0.CO;2-7.

[25] M.A. Green, K. Emery, K. B??cher, D.L. King, S. Igari, Solar cell efficiency tables (Version 14), Prog. Photovoltaics Res. Appl. 7 (1999) 321–326. doi:10.1002/(SICI)1099-159X(199907/08)7:4<321::AID-PIP283>3.0.CO;2-H.

[26] E.D. Green, M. A., Emery, K., Hishikawa, Y., Warta, W. & Dunlop, Solar cell efficiency tables (Version 13), Prog. Photovoltaics Res. Appl. 19 (1999) 565–572. doi:10.1002/(SICI)1099-159X(199901/02)7.

[27] M.A. Green, K. Emery, D.L. King, S. Igari, W. Warta, Solar cell efficiency tables (Version 16), Prog. Photovoltaics Res. Appl. 8 (2000) 377–383. doi:10.1002/1099-159X(200007/08)8:4<377::AID-PIP339>3.0.CO;2-H.

[28] M.A. Green, K. Emery, Y. Hishikawa, W. Warta, Solar cell efficiency tables (Version 15), Prog. Photovoltaics Res. Appl. 17 (2000) 320–326. doi:10.1002/pip.

[29] M.A. Green, K. Emery, D.L. King, S. Igari, W. Warta, Solar cell efficiency tables (Version 17), Prog. Photovoltaics Res. Appl. 9 (2001) 49–56. doi:10.1002/pip.361.

[30] M.A. Green, K. Emery, D.L. King, S. Igari, W. Warta, Solar cell efficiency tables (Version 18), Prog. Photovoltaics Res. Appl. 9 (2001) 287–293. doi:10.1002/pip.389.

[31] M.A. Green, K. Emery, D.L. King, S. Igari, W. Warta, Solar cell efficiency tables (Version 19), Prog. Photovoltaics Res. Appl. 10 (2002) 55–61. doi:10.1002/pip.428.

[32] M.A. Green, K. Emery, D.L. King, S. Igari, W. Warta, Solar cell efficiency tables (version 20), Prog. Photovoltaics Res. Appl. 11 (2002) 347–352. doi:10.1002/pip.499.

[33] M.A. Green, K. Emery, D.L. King, S. Igari, W. Warta, Solar cell efficiency tables (Version 21), Prog. Photovoltaics Res. Appl. 11 (2003) 39–45. doi:10.1002/pip.478.

[34] M.A. Green, K. Emery, D.L. King, S. Igari, W. Warta, Solar cell efficiency tables (version 22), Prog. Photovoltaics Res. Appl. 11 (2003) 347–352. doi:10.1002/pip.499.

[35] M.A. Green, K. Emery, D.L. King, S. Igari, W. Warta, Solar cell efficiency tables (Version 23), Prog. Photovoltaics Res. Appl. 12 (2004) 55–62. doi:10.1002/pip.530.

[36] M.A. Green, K. Emery, D.L. King, S. Igari, W. Warta, Solar cell efficiency tables (Version 24), Prog. Photovoltaics Res. Appl. 12 (2004) 365–372. doi:10.1002/pip.574.

[37] M.A. Green, K. Emery, D.L. King, S. Igari, W. Warta, Solar cell efficiency tables (Version 25), Prog. Photovoltaics Res. Appl. 13 (2005) 49–54. doi:10.1002/pip.598.

[38] M.A. Green, K. Emery, D.L. King, S. Igari, W. Warta, Solar cell efficiency tables (Version 26), Prog. Photovoltaics Res. Appl. 13 (2005) 387–392. doi:10.1002/pip.651.

[39] M.A. Green, K. Emery, D.L. King, Y. Hisikawa, W. Warta, Solar cell efficiency tables (Version 27), Prog. Photovoltaics Res. Appl. 14 (2006) 45–51. doi:10.1002/pip.686.

[40] M.A. Green, K. Emery, D.L. King, Y. Hishikawa, W. Warta, Solar cell

efficiency tables (Version 28), Prog. Photovoltaics Res. Appl. 14 (2006) 455–461. doi:10.1002/pip.720.

[41] M.A. Green, K. Emery, D.L. King, Y. Hishikawa, W. Warta, Solar cell efficiency tables (Version 29), Prog. Photovoltaics Res. Appl. 15 (2007) 35–40. doi:10.1002/pip.741.

[42] M.A. Green, K. Emery, Y. Hisikawa, W. Warta, Solar cell efficiency tables (Version 30), Prog. Photovoltaics Res. Appl. 15 (2007) 425–430. doi:10.1002/pip.781.

[43] M.A. Green, K. Emery, Y. Hishikawa, W. Warta, Solar cell efficiency tables (Version 31), Prog. Photovoltaics Res. Appl. 16 (2008) 61–67. doi:10.1002/pip.808.

[44] M.A. Green, K. Emery, Y. Hishikawa, W. Warta, Solar cell efficiency tables (Version 32), Prog. Photovoltaics Res. Appl. 16 (2008) 435–440. doi:10.1002/pip.842.

[45] M.A. Green, K. Emery, Y. Hishikawa, W. Warta, Solar cell efficiency tables (Version 33), Prog. Photovoltaics Res. Appl. 17 (2009) 85–94. doi:10.1002/pip.880.

[46] M.A. Green, K. Emery, Y. Hishikawa, W. Warta, Solar cell efficiency tables (Version 34), Prog. Photovoltaics Res. Appl. 17 (2009) 320–326. doi:10.1002/pip.911.

[47] M.A. Green, K. Emery, Y. Hishikawa, W. Warta, Solar cell efficiency tables (Version 35), Prog. Photovoltaics Res. Appl. 18 (2010) 144–150. doi:10.1002/pip.974.

[48] M.A. Green, K. Emery, Y. Hishikawa, W. Warta, Solar cell efficiency tables (Version 36), Prog. Photovoltaics Res. Appl. 18 (2010) 346–352. doi:10.1002/pip.1021.

[49] M.A. Green, K. Emery, Y. Hishikawa, W. Warta, Solar cell efficiency tables (Version 37), Prog. Photovoltaics Res. Appl. 19 (2011) 84–92.

doi:10.1002/pip.1088.

[50]   M.A. Green, K. Emery, Y. Hishikawa, W. Warta, E.D. Dunlop, Solar cell efficiency tables (Version 38), Prog. Photovoltaics Res. Appl. 19 (2011) 565–572. doi:10.1002/pip.1150.

[51]   M.A. Green, K. Emery, Y. Hishikawa, W. Warta, E.D. Dunlop, Solar cell efficiency tables (Version 40), Prog. Photovoltaics Res. Appl. 20 (2012) 606–614. doi:10.1002/pip.2267.

[52]   M.A. Green, K. Emery, Y. Hishikawa, W. Warta, E.D. Dunlop, Solar cell efficiency tables (Version 39), Prog. Photovoltaics Res. Appl. 20 (2012) 12–20. doi:10.1002/pip.2163.

[53]   M.A. Green, K. Emery, Y. Hishikawa, W. Warta, E.D. Dunlop, Solar cell efficiency tables (Version 42), Prog. Photovoltaics Res. Appl. 21 (2013) 827–837. doi:10.1002/pip.2404.

[54]   M.A. Green, K. Emery, Y. Hishikawa, W. Warta, E.D. Dunlop, Solar cell efficiency tables (Version 41), Prog. Photovoltaics Res. Appl. 21 (2013) 1–11. doi:10.1002/pip.2352.

[55]   M.A. Green, K. Emery, Y. Hishikawa, W. Warta, E.D. Dunlop, Solar cell efficiency tables (Version 44), Prog. Photovoltaics Res. Appl. 22 (2014) 701–710. doi:10.1002/pip.2525.

[56]   M.A. Green, K. Emery, Y. Hishikawa, W. Warta, E.D. Dunlop, Solar cell efficiency tables (Version 43), Prog. Photovoltaics Res. Appl. (2014) 1–9. doi:10.1002/pip.

[57]   M.A. Green, K. Emery, Y. Hishikawa, W. Warta, E.D. Dunlop, Solar cell efficiency tables (Version 46), Prog. Photovoltaics Res. Appl. 23 (2015) 805–812. doi:10.1002/pip.2637.

[58]   M.A. Green, K. Emery, Y. Hishikawa, W. Warta, E.D. Dunlop, Solar cell efficiency tables (Version 45), Prog. Photovoltaics Res. Appl. 23 (2015) 1–9. doi:10.1002/pip.2573.

[59] H.C. Sio, D. Macdonald, Direct comparison of the electrical properties of multicrystalline silicon materials for solar cells: conventional p-type, n-type and high performance p-type, Sol. Energy Mater. Sol. Cells. 144 (2016) 339–346. doi:10.1016/j.solmat.2015.09.011.

[60] International Technology Roadmap for Photovoltaic - 2015 Results, 2016.

[61] F. Dross, K. Baert, T. Bearda, J. Deckers, V. Depauw, O. El Daif, I. Gordon, A. Gougam, J. Govaerts, S. Granata, R. Labie, X. Loozen, R. Martini, A. Masolin, B.O. Sullivan, Y. Qiu, J. Vaes, D. Van Gestel, J. Van Hoeymissen, A. Vanleenhove, K. Van Nieuwenhuysen, S. Venkatachalam, M. Meuris, Crystalline thin-foil silicon solar cells : where crystalline quality meets thin- fi lm processing, (2012) 770–784. doi:10.1002/pip.

[62] S.R. Wenham, M.A. Green, Silicon Solar Cells, 4 (1996) 3–33.

[63] C. Battaglia, A. Cuevas, S. De Wolf, High-efficiency crystalline silicon solar cells: status and perspectives, Energy Environ. Sci. 9 (2016) 1552–1576. doi:10.1039/C5EE03380B.

[64] I. Shoukry, J. Libal, R. Kopecek, E. Wefringhaus, J. Werner, Modelling of bifacial gain for stand-alone and in-field installed bifacial PV modules, in: 2016: pp. 0–8.

[65] Y.-T. Cheng, J.-J. Ho, W.J. Lee, S.-Y. Tsai, Y.-A. Lu, J.-J. Liou, S.-H. Chang, K.L. Wang, Investigation of Low-Cost Surface Processing Techniques for Large-Size Multicrystalline Silicon Solar Cells, Int. J. Photoenergy. 2010 (2010) 1–6. doi:10.1155/2010/268035.

[66] J.Y. Kwon, D.H. Lee, M. Chitambar, S. Maldonado, A. Tuteja, A. Boukai, High efficiency thin upgraded metallurgical-grade silicon solar cells on flexible substrates., Nano Lett. 12 (2012) 5143–7. doi:10.1021/nl3020445.

[67] X. Gu, X. Yu, K. Guo, L. Chen, D. Wang, D. Yang, Seed-assisted cast quasi-single crystalline silicon for photovoltaic application: Towards high efficiency and low cost silicon solar cells, Sol. Energy Mater. Sol. Cells. 101 (2012) 95–101. doi:10.1016/j.solmat.2012.02.024.

[68]   V. Depauw, Y. Qiu, K. Van Nieuwenhuysen, I. Gordon, J. Poortmans, Epitaxy-free monocrystalline silicon thin film : first steps beyond proof-of-concept solar cells, (2011) 844–850. doi:10.1002/pip.

[69]   E. Schmich, H. Lautenschlager, T. Frieß, F. Trenkle, N. Schillinger, S. Reber, n-Type Emitter Epitaxy for Crystalline Silicon Thin-Film Solar Cells, (2008) 159–170. doi:10.1002/pip.

[70]   R. Brendel, Crystalline thin-film silicon solar cells from layer-transfer processes : a review Lambertian intrinsic surface grain boundary single pass, (2000).

[71]   J. Rentsch, S. Bau, D.M. Hulji?, Screen-printed epitaxial silicon thin-film solar cells with 13.8% efficiency, Prog. Photovoltaics Res. Appl. 11 (2003) 527–534. doi:10.1002/pip.513.

[72]   I. Gordon, S. Vallon, A. Mayolet, G. Beaucarne, J. Poortmans, Thin-film monocrystalline-silicon solar cells made by a seed layer approach on glass-ceramic substrates, Sol. Energy Mater. Sol. Cells. 94 (2010) 381–385. doi:10.1016/j.solmat.2009.08.015.

[73]   M.A. Green, Self-consistent optical parameters of intrinsic silicon at 300K including temperature coefficients, Sol. Energy Mater. Sol. Cells. 92 (2008) 1305–1310. doi:10.1016/j.solmat.2008.06.009.

[74]   Z.C. Holman, A. Descoeudres, L. Barraud, F.Z. Fernandez, J.P. Seif, S. De Wolf, C. Ballif, Current Losses at the Front of Silicon Heterojunction Solar Cells, IEEE J. Photovoltaics. 2 (2012) 7–15. doi:10.1109/JPHOTOV.2011.2174967.

[75]   D.E. Aspnes, A.A. Studna, Dielectric functions and optical parameters of Si, Ge, GaP, GaAs, GaSb, InP, InAs, and InSb from 1.5 to 6.0 eV, Phys. Rev. B. 27 (1983) 985–1009. doi:10.1103/PhysRevB.27.985.

[76]   P. Löper, M. Stuckelberger, B. Niesen, J. Werner, M. Filipič, S.-J. Moon, J.-H. Yum, M. Topič, S. De Wolf, C. Ballif, Complex Refractive Index Spectra of $CH_3 NH_3 PbI_3$ Perovskite Thin Films Determined by Spectroscopic

Ellipsometry and Spectrophotometry, J. Phys. Chem. Lett. 6 (2015) 66–71. doi:10.1021/jz502471h.

[77]   K. Morita, Y. Inomata, T. Suemasu, Optical and electrical properties of semiconducting $BaSi_2$ thin films on Si substrates grown by molecular beam epitaxy, Thin Solid Films. 508 (2006) 363–366. doi:10.1016/j.tsf.2005.07.344.

[78]   No Title, (n.d.). http://pvinsights.com/. Accessed: 2016-06-02. (Archived by WebCite� at http://www.webcitation.org/6hyM9f1pp) (accessed June 2, 2016).

[79]   International Technology Roadmap for Photovoltaic - 2015 Results, 2016. http://scholar.google.com/scholar?hl=en&btnG=Search&q=intitle:International+Technology+Roadmap+for+Photovoltaic#1.

[80]   Y. Li, Z. Li, Y. Zhao, A. Lennon, Modelling of Light Trapping in Acidic-Textured Multicrystalline Silicon Wafers, Int. J. Photoenergy. 2012 (2012) 1–8. doi:10.1155/2012/369101.

[81]   K.X. Wang, Z. Yu, V. Liu, Y. Cui, S. Fan, Absorption enhancement in ultrathin crystalline silicon solar cells with antireflection and light-trapping nanocone gratings., Nano Lett. 12 (2012) 1616–9. http://www.pubmedcentral.nih.gov/articlerender.fcgi?artid=3698494&tool=pmcentrez&rendertype=abstract.

[82]   B.K. Nayak, V. V Iyengar, M.C. Gupta, Efficient light trapping in silicon solar cells by ultrafast-laser-induced self-assembled micro / nano structures, Prog. PHOTOVOLTAICS Res. Appl. (2011) 631–639. doi:10.1002/pip.

[83]   E. Yablonovitch, G.D. Cody, Intensity enhancement in textured optical sheets for solar cells, IEEE Trans. Electron Devices. 29 (1982) 300–305. doi:10.1109/T-ED.1982.20700.

[84]   K.J. Weber, a. W. Blakers, A novel silicon texturization method based on etching through a silicon nitride mask, Prog. Photovoltaics Res. Appl. 13 (2005) 691–695. doi:10.1002/pip.632.

[85] W.C.S. Jessica D. Hylton, Ronald Kinderman, Antonius R. Burgers, Uniform Pyramid Formation on Alkaline-et ched Polished Monocrystalline (100) Silicon Wafers, 4 (1996) 435–438.

[86] S. Bilgen, F. Es, R. Turan, Comparison of mechanical and ultrasonic agitation methods for mono c-Si texturing, Phys. Status Solidi. (2016). doi:10.1002/pssa.201600205.

[87] K. Kim, S.K. Dhungel, S. Jung, D. Mangalaraj, J.Ã. Yi, Texturing of large area multi-crystalline silicon wafers through different chemical approaches for solar cell fabrication, Sol. Energy Mater. Sol. Cells. 92 (2008) 960–968. doi:10.1016/j.solmat.2008.02.036.

[88] D. Kumar, S. S.K., S. P.K., H.M.. K. V V., Fabrication of silicon nanowire arrays based solar cell with improved performance, Sol. Energy Mater. Sol. Cells. 95 (2011) 215–218. doi:10.1016/j.solmat.2010.04.024.

[89] E. Garnett, P. Yang, Light trapping in silicon nanowire solar cells, Nano Lett. 10 (2010) 1082–1087. doi:10.1021/nl100161z.

[90] T. Stelzner, M. Pietsch, G. Andrä, F. Falk, E. Ose, S. Christiansen, Silicon nanowire-based solar cells., Nanotechnology. 19 (2008) 295203. doi:10.1088/0957-4484/19/29/295203.

[91] M. Kulakci, F. Es, B. Ozdemir, H.E. Unalan, R. Turan, Application of Si Nanowires Fabricated by Metal-Assisted Etching to Crystalline Si Solar Cells, 3 (2013) 548–553.

[92] F. Es, O. Demircioglu, M. Gunoven, M. Kulakci, H.E. Unalan, R. Turan, Performance of nanowire decorated mono- and multi-crystalline Si solarcells, Phys. E Low-Dimensional Syst. Nanostructures. 51 (2013) 71–74. doi:10.1016/j.physe.2013.01.002.

[93] H. Yue, R. Jia, C. Chen, W. Ding, Y. Meng, D. Wu, D. Wu, W. Chen, X. Liu, Z. Jin, W. Wang, T. Ye, Antireflection properties and solar cell application of silicon nanostructures, J. Vac. Sci. Technol. B Microelectron. Nanom. Struct. 29 (2011) 031208. doi:10.1116/1.3591344.

[94] J. Oh, H.-C. Yuan, H.M. Branz, An 18.2%-efficient black-silicon solar cell achieved through control of carrier recombination in nanostructures, Nat. Nanotechnol. 7 (2012) 743–8. doi:10.1038/nnano.2012.166.

[95] C.-H. Lin, D.Z. Dimitrov, C.-H. Du, C.-W. Lan, Influence of surface structure on the performance of black-silicon solar cell, Phys. Status Solidi. 7 (2010) 2778–2784. doi:10.1002/pssc.200925644.

[96] P. Repo, J. Benick, V. Vähänissi, J. Schön, G. von Gastrow, B. Steinhauser, M.C. Schubert, M. Hermle, H. Savin, N-type Black Silicon Solar Cells, Energy Procedia. 38 (2013) 866–871. doi:10.1016/j.egypro.2013.07.358.

[97] J. Shi, F. Xu, Z. Ma, P. Zhou, L. Zheng, J. Yang, D. Chen, Z. Jiang, Nanoporous black multi-crystalline silicon solar cells: realization of low reflectance and explanation of high recombination loss, Mater. Sci. Semicond. Process. 16 (2013) 441–448. doi:10.1016/j.mssp.2012.08.006.

[98] Y. Su, S. Li, G. Zhao, Z. Wu, Y. Yang, W. Li, Y. Jiang, Optical properties of black silicon prepared by wet etching, J. Mater. Sci. Mater. Electron. 23 (2012) 1558–1561. doi:10.1007/s10854-012-0628-6.

[99] A. Kurek, S.T. Barry, Metal-assisted chemical etching using sputtered gold: a simple route to black silicon, Sci. Technol. Adv. Mater. 12 (2011) 045001. doi:10.1088/1468-6996/12/4/045001.

[100] Y. Dan, K. Seo, K. Takei, J.H. Meza, A. Javey, K.B. Crozier, Dramatic reduction of surface recombination by in situ surface passivation of silicon nanowires., Nano Lett. 11 (2011) 2527–2532.

[101] W.C. Hsu, Y.-S. Lu, J.-Y. Chyan, J.A. Yeh, High-Efficiency 6″ Multicrystalline Black Solar Cells Based on Metal-Nanoparticle-Assisted Chemical Etching, Int. J. Photoenergy. 2012 (2012) 1–7. doi:10.1155/2012/197514.

[102] O. Gunawan, K. Wang, B. Fallahazad, Y. Zhang, E. Tutuc, S. Guha, High performance wire-array silicon solar cells, (2011) 307–312. doi:10.1002/pip.

[103] H. Li, R. Jia, C. Chen, Z. Xing, W. Ding, Y. Meng, D. Wu, X. Liu, T. Ye,

Influence of nanowires length on performance of crystalline silicon solar cell, Appl. Phys. Lett. 98 (2011) 151116. doi:10.1063/1.3574904.

[104] R. Li, S. Chuwongin, S. Wang, N. Technology, O. Technology, Ag-Assisted Electrochemical Etching of Silicon for Antireflection in Large Area Crystalline Thin Film Photovoltaics, 2 (2011) 2563–2565.

[105] F.J. Beck, S. Mokkapati, K.R. Catchpole, Plasmonic light-trapping for Si solar cells using self-assembled, Ag nanoparticles, Prog. Photovoltaics Res. Appl. 18 (2010) 500–504. doi:10.1002/pip.1006.

[106] R.B. Wehrspohn, J. Üpping, 3D photonic crystals for photon management in solar cells, J. Opt. 14 (2012) 024003. doi:10.1088/2040-8978/14/2/024003.

[107] M. Moreno, D. Murias, J. Martínez, C. Reyes-Betanzo, A. Torres, R. Ambrosio, P. Rosales, P. Roca i Cabarrocas, M. Escobar, A comparative study of wet and dry texturing processes of c-Si wafers for the fabrication of solar cells, Sol. Energy. 101 (2014) 182–191. doi:10.1016/j.solener.2014.01.004.

[108] H.S. Cells, Optical and Electrical Properties of Laser Texturing for High-efficiency Solar Cells, (2006) 225–235. doi:10.1002/pip.

[109] F.M.M. Souren, J. Rentsch, M.C.M. Van De Sanden, Relation between light trapping and surface topography of plasma textured crystalline silicon wafers, (2015) 352–366. doi:10.1002/pip.

[110] M. Gaudig, J. Hirsch, T. Schneider, A.N. Sprafke, J. Ziegler, N. Bernhard, R.B. Wehrspohn, J. Hirsch, T. Schneider, A.N. Sprafke, J. Ziegler, Properties of black silicon obtained at room-temperature by different plasma modes Properties of black silicon obtained at room-temperature by different plasma modes, J. Vac. Sci. Technol. 132 (2015). doi:10.1116/1.4929540.

[111] Z.P. Huang, N. Geyer, L.F. Liu, M.Y. Li, P. Zhong, Metal-assisted electrochemical etching of silicon., Nanotechnology. 21 (2010) 465301. doi:10.1088/0957-4484/21/46/465301.

[112] H.-J. Choi, S. Baek, H.S. Jang, S.B. Kim, B.-Y. Oh, J.H. Kim, Optimization of

metal-assisted chemical etching process in fabrication of p-type silicon wire arrays, Curr. Appl. Phys. 11 (2011) S25–S29. doi:10.1016/j.cap.2010.11.047.

[113] J. Kim, Y.H. Kim, S.-H. Choi, W. Lee, Curved silicon nanowires with ribbon-like cross sections by metal-assisted chemical etching., ACS Nano. 5 (2011) 5242–5248.

[114] Z. Huang, N. Geyer, P. Werner, J. de Boor, U. Gösele, Metal-assisted chemical etching of silicon: a review., Adv. Mater. 23 (2011) 285–308. doi:10.1002/adma.201001784.

[115] C. Chartier, S. Bastide, C. Lévy-Clément, Metal-assisted chemical etching of silicon in HF–H2O2, Electrochim. Acta. 53 (2008) 5509–5516. doi:10.1016/j.electacta.2008.03.009.

[116] X. Li, Metal assisted chemical etching for high aspect ratio nanostructures: A review of characteristics and applications in photovoltaics, Curr. Opin. Solid State Mater. Sci. 16 (2012) 71–81. doi:10.1016/j.cossms.2011.11.002.

[117] B. Ozdemir, M. Kulakci, R. Turan, H.E. Unalan, Effect of electroless etching parameters on the growth and reflection properties of silicon nanowires., Nanotechnology. 22 (2011) 155606. doi:10.1088/0957-4484/22/15/155606.

[118] K.W. Kolasinski, Silicon nanostructures from electroless electrochemical etching, Curr. Opin. Solid State Mater. Sci. 9 (2005) 73–83. doi:10.1016/j.cossms.2006.03.004.

[119] K. Peng, Y. Yan, S. Gao, J. Zhu, Dendrite-Assisted Growth of Silicon Nanowires in Electroless Metal Deposition, Adv. Funct. Mater. 13 (2003) 127–132. http://doi.wiley.com/10.1002/adfm.200390018.

[120] K. Liu, S. Qu, F. Tan, Y. Bi, S. Lu, Z. Wang, Ordered silicon nanowires prepared by template-assisted morphological design and metal-assisted chemical etching, Mater. Lett. 101 (2013) 96–98. doi:10.1016/j.matlet.2013.03.086.

[121] L. Boarino, D. Imbraguglio, E. Enrico, N. De Leo, F. Celegato, P. Tiberto, N.

Pugno, G. Amato, Fabrication of ordered silicon nanopillars and nanowires by self-assembly and metal-assisted etching, Phys. Status Solidi. 208 (2011) 1412–1416. doi:10.1002/pssa.201000182.

[122] H.S. Jang, H.-J. Choi, B.-Y. Oh, J.H. Kim, Combinational Approach of Electrochemical Etching and Metal-Assisted Chemical Etching for p-Type Silicon Wire Formation, Electrochem. Solid-State Lett. 14 (2011) D5. doi:10.1149/1.3504127.

[123] K. Liu, S. Qu, X. Zhang, Z. Wang, Anisotropic characteristics and morphological control of silicon nanowires fabricated by metal-assisted chemical etching, J. Mater. Sci. 48 (2012) 1755–1762. doi:10.1007/s10853-012-6936-7.

[124] Z. Huang, X. Zhang, M. Reiche, L. Liu, W. Lee, T. Shimizu, S. Senz, U. Gösele, Extended arrays of vertically aligned sub-10 nm diameter [100] Si nanowires by metal-assisted chemical etching., Nano Lett. 8 (2008) 3046–3051.

[125] M. Zhang, K. Peng, X. Fan, J. Jie, R. Zhang, S. Lee, N. Wong, Preparation of Large-Area Uniform Silicon Nanowires Arrays through Metal-Assisted Chemical Etching, (2008) 4444–4450.

[126] J. de Boor, N. Geyer, J. V Wittemann, U. Gösele, V. Schmidt, Sub-100 nm silicon nanowires by laser interference lithography and metal-assisted etching., Nanotechnology. 21 (2010) 095302. doi:10.1088/0957-4484/21/9/095302.

[127] A. Chiou, T. Chien, C. Su, J. Lin, C. Hsu, The effect of differently sized Ag catalysts on the fabrication of a silicon nanowire array using Ag-assisted electroless etching, Curr. Appl. Phys. 13 (2013) 717–724. doi:10.1016/j.cap.2012.11.011.

[128] H. Asoh, F. Arai, S. Ono, Effect of noble metal catalyst species on the morphology of macroporous silicon formed by metal-assisted chemical etching, Electrochim. Acta. 54 (2009) 5142–5148. doi:10.1016/j.electacta.2009.01.050.

[129] M. Zahedinejad, S.D. Farimani, M. Khaje, H. Mehrara, A. Erfanian, F. Zeinali, Deep and vertical silicon bulk micromachining using metal assisted chemical

etching, J. Micromechanics Microengineering. 23 (2013) 055015. doi:10.1088/0960-1317/23/5/055015.

[130] D. Li, L. Wang, D. Li, N. Zhou, Z. Feng, X. Zhong, D. Yang, Formation of nanostructured emitter for silicon solar cells using catalytic silver nanoparticles, Appl. Surf. Sci. 264 (2013) 621–624. doi:10.1016/j.apsusc.2012.10.079.

[131] D.H. Wan, H.L. Chen, S.Y. Chuang, C.C. Yu, Y.C. Lee, Using Self-Assembled Nanoparticles to Fabricate and Optimize Subwavelength Textured Structures in Solar Cells, (2008) 20567–20573.

[132] S. Bastide, N. Le Quang, R. Monna, C. Lévy-Clément, Chemical etching of Si by Ag nanocatalysts in HF-H_2O_2 : application to multicrystalline Si solar cell texturisation, Phys. Status Solidi. 6 (2009) 1536–1540. doi:10.1002/pssc.200881016.

[133] K. Tsujino, M. Matsumura, Y. Nishimoto, Texturization of multicrystalline silicon wafers for solar cells by chemical treatment using metallic catalyst, 90 (2006) 100–110. doi:10.1016/j.solmat.2005.02.019.

[134] J. Cichoszewski, M. Reuter, J.H. Werner, +0.4% Efficiency gain by novel texture for String Ribbon solar cells, Sol. Energy Mater. Sol. Cells. 101 (2012) 1–4. doi:10.1016/j.solmat.2012.01.031.

[135] S.-H. Baek, H.S. Jang, J.H. Kim, Characterization of optical absorption and photovoltaic properties of silicon wire solar cells with different aspect ratio, Curr. Appl. Phys. 11 (2011) S30–S33. doi:10.1016/j.cap.2010.11.040.

[136] F. Es, O. Demircioglu, M. Kulakci, H.E. Unalan, R. Turan, Light management on industrial size c-Si solar cells by Si nanowires fabricated by metal-assisted etching, 8373 (2012) 837312–837312–5. doi:10.1117/12.918884.

[137] N. Geyer, B. Fuhrmann, H.S. Leipner, P. Werner, Ag-mediated charge transport during metal-assisted chemical etching of silicon nanowires., ACS Appl. Mater. Interfaces. 5 (2013) 4302–8. http://www.ncbi.nlm.nih.gov/pubmed/23635321.

[138] Z.R. Smith, R.L. Smith, S.D. Collins, Mechanism of nanowire formation in

metal assisted chemical etching, Electrochim. Acta. 92 (2013) 139–147. doi:10.1016/j.electacta.2012.12.075.

[139] C.Q. Lai, H. Cheng, W.K. Choi, C. V Thompson, Mechanics of Catalyst Motion during Metal Assisted Chemical Etching of Silicon, (2013).

[140] N. Megouda, T. Hadjersi, S. Szunerits, R. Boukherroub, Electroless chemical etching of silicon in aqueous $NH_4F/AgNO_3/HNO_3$ solution, Appl. Surf. Sci. 284 (2013) 894–899. doi:10.1016/j.apsusc.2013.08.033.

[141] R. Douani, K. Si-Larbi, T. Hadjersi, N. Megouda, a. Manseri, Silver-assisted electroless etching mechanism of silicon, Phys. Status Solidi. 205 (2008) 225–230. doi:10.1002/pssa.200723159.

[142] K. Peng, A. Lu, R. Zhang, S.-T. Lee, Motility of Metal Nanoparticles in Silicon and Induced Anisotropic Silicon Etching, Adv. Funct. Mater. 18 (2008) 3026–3035. doi:10.1002/adfm.200800371.

[143] Z. Huang, T. Shimizu, S. Senz, Z. Zhang, N. Geyer, U. Gösele, Oxidation Rate Effect on the Direction of Metal-Assisted Chemical and Electrochemical Etching of Silicon, J. Phys. Chem. C. 114 (2010) 10683–10690. http://pubs.acs.org/doi/abs/10.1021/jp911121q.

[144] K. Peng, A. Lu, R. Zhang, S.-T. Lee, Motility of Metal Nanoparticles in Silicon and Induced Anisotropic Silicon Etching, Adv. Funct. Mater. 18 (2008) 3026–3035. doi:10.1002/adfm.200800371.

[145] N. Megouda, T. Hadjersi, G. Piret, R. Boukherroub, O. Elkechai, Au-assisted electroless etching of silicon in aqueous HF/H_2O_2 solution, Appl. Surf. Sci. 255 (2009) 6210–6216. doi:10.1016/j.apsusc.2009.01.075.

[146] Z. Yue, H. Shen, Y. Jiang, W. Wang, J. Jin, Novel and low reflective silicon surface fabricated by Ni-assisted electroless etching and coated with atomic layer deposited Al2O3 film, Appl. Phys. A. 114 (2014) 813–817. doi:10.1007/s00339-013-7670-y.

[147] Y. Cao, Y. Zhou, F. Liu, Y. Zhou, Y. Zhang, Y. Liu, Y. Guo, Progress and

Mechanism of Cu Assisted Chemical Etching of Silicon in a Low Cu^{2+} Concentration Region, ECS J. Solid State Sci. Technol. 4 (2015) P331–P336. doi:10.1149/2.0191508jss.

[148] F. Es, M. Kulakci, R. Turan, An Alternative Metal-Assisted Etching Route for Texturing Silicon Wafers for Solar Cell Applications, IEEE J. Photovoltaics. (2016) 1–7.

[149] C. Trompoukis, I. Abdo, R. Cariou, I. Cosme, W. Chen, O. Deparis, A. Dmitriev, E. Drouard, M. Foldyna, E.G.- Caurel, I. Gordon, B. Heidari, A. Herman, L. Lalouat, K.-D. Lee, J. Liu, K. Lodewijks, F. Mandorlo, I. Massiot, A. Mayer, V. Mijkovic, J. Muller, R. Orobtchouk, G. Poulain, P. Prod'Homme, P.R.I. Cabarrocas, C. Seassal, J. Poortmans, R. Mertens, O. El Daif, V. Depauw, Photonic nanostructures for advanced light trapping in thin crystalline silicon solar cells, Phys. Status Solidi. 212 (2015) 140–155. doi:10.1002/pssa.201431180.

[150] S. Kato, Y. Kurokawa, Y. Watanabe, Y. Yamada, A. Yamada, Y. Ohta, Y. Niwa, M. Hirota, Optical assessment of silicon nanowire arrays fabricated by metal-assisted chemical etching., Nanoscale Res. Lett. 8 (2013) 216. doi:10.1186/1556-276X-8-216.

[151] R.A. Sinton, A. Cuevas, M. Stuckings, Quasi-steady-state photoconductance, a new method for solar cell material and device characterization, in: Conf. Rec. Twenty Fifth IEEE Photovolt. Spec. Conf. - 1996, IEEE, 1996: pp. 457–460. doi:10.1109/PVSC.1996.564042.

[152] ASTM G173-03(2012), Standard Tables for Reference Solar Spectral Irradiances: Direct Normal and Hemispherical on 37° Tilted Surface, Astm. 03 (2013) 1–21. doi:10.1520/G0173-03R12.2.

[153] P. Repo, J. Benick, V. Vähänissi, J. Schön, G. von Gastrow, B. Steinhauser, M.C. Schubert, M. Hermle, H. Savin, N-type Black Silicon Solar Cells, Energy Procedia. 38 (2013) 866–871. doi:10.1016/j.egypro.2013.07.358.

[154] X. Liu, P.R. Coxon, M. Peters, B. Hoex, J.M. Cole, D.J. Fray, Black silicon:

fabrication methods, properties and solar energy applications, Energy Environ. Sci. 7 (2014) 3223–3263. doi:10.1039/C4EE01152J.

[155] A. Cuevas, R.A. Sinton, Prediction of the open-circuit voltage of solar cells from the steady-state photoconductance, Prog. Photovoltaics Res. Appl. 5 (1997) 79–90. doi:10.1002/(SICI)1099-159X(199703/04)5:2<79::AID-PIP155>3.0.CO;2-J.

[156] X. Liu, P.R. Coxon, M. Peters, B. Hoex, J.M. Cole, D.J. Fray, Black silicon: fabrication methods, properties and solar energy applications, Energy Environ. Sci. 7 (2014) 3223–3263. doi:10.1039/C4EE01152J.

[157] R. Einhaus, E. Vazsonyi, J. Szlufcik, J. Nijs, R. Mertens, Isotropic texturing of multicrystalline silicon wafers with acidic texturing solutions [solar cell manufacture], in: Conf. Rec. Twenty Sixth IEEE Photovolt. Spec. Conf. - 1997, IEEE, 1997: pp. 167–170. doi:10.1109/PVSC.1997.654055.

[158] N. Borojevic, Y. Li, A. Lennon, S. Wenham, Optical performance analysis of inkjet-textured multicrystalline silicon solar cells using angular distribution matrices, Sol. Energy. 118 (2015) 295–302. doi:10.1016/j.solener.2015.05.030.

[159] Y. Liu, G. Ji, J. Wang, X. Liang, Z. Zuo, Y. Shi, Fabrication and photocatalytic properties of silicon nanowires by metal-assisted chemical etching: effect of H2O2 concentration., Nanoscale Res. Lett. 7 (2012) 663. doi:10.1186/1556-276X-7-663.

[160] D. Dimova-Malinovska, M. Sendova-Vassileva, N. Tzenov, M. Kamenova, Preparation of thin porous silicon layers by stain etching, Thin Solid Films. 297 (1997) 9–12. doi:10.1016/S0040-6090(96)09434-5.

[161] M.S. Wafers, B.Y. Chemical, T. Using, M. Catalyst, Multicrystalline silicon wafers by chemical treatment using metallic catalyst, (2003) 1507–1510.

[162] Y. Jiang, R. Qing, H. Yang, C. Chen, H. Ma, F. Chang, Alkali-treated Si nanowire array for improving solar cell performance, Appl. Phys. A. 113 (2013) 13–17. doi:10.1007/s00339-013-7846-5.

[163] VLSI Fabrication and Principles: Silicon and Gallium Arsenide (H S. K. Ghandi Wiley & Sons, 2. Auflage (1994). 834 S., 58 £, Vak. Forsch. Und Prax. 7 (1995) 72–72. doi:10.1002/vipr.19950070116.

[164] H. Park, S. Kwon, J.S. Lee, H.J. Lim, S. Yoon, D. Kim, Improvement on surface texturing of single crystalline silicon for solar cells by saw-damage etching using an acidic solution, Sol. Energy Mater. Sol. Cells. 93 (2009) 1773–1778. doi:10.1016/j.solmat.2009.06.012.

[165] S. Rühle, Tabulated values of the Shockley–Queisser limit for single junction solar cells, Sol. Energy. 130 (2016) 139–147. doi:10.1016/j.solener.2016.02.015.

[166] A.K. Katiyar, S. Mukherjee, M. Zeeshan, S.K. Ray, A.K. Raychaudhuri, Enhancement of Efficiency of a Solar Cell Fabricated on Black Si Made by Inductively Coupled Plasma-Reactive Ion Etching Process: A Case Study of a n-CdS/p-Si Heterojunction Cell, ACS Appl. Mater. Interfaces. 7 (2015) 23445–23453. doi:10.1021/acsami.5b04978.

[167] D.A. Clugston, P.A. Basore, PC1D version 5: 32-bit solar cell modeling on personal computers, Conf. Rec. Twenty Sixth IEEE Photovolt. Spec. Conf. - 1997. (1997) 207–210. doi:10.1109/PVSC.1997.654065.

[168] C.W. Lan, Y.M. Yang, A. Yu, Y.C. Wu, B. Hsu, W.C. Hsu, A. Yang, Recent Progress of Crystal Growth Technology for Multi-Crystalline Silicon Solar Ingot, Solid State Phenom. 242 (2015) 21–29. doi:10.4028/www.scientific.net/SSP.242.21.

[169] Y.M. Yang, A. Yu, B. Hsu, W.C. Hsu, A. Yang, C.W. Lan, Development of high-performance multicrystalline silicon for photovoltaic industry, Prog. Photovoltaics Res. Appl. 23 (2015) 340–351. doi:10.1002/pip.2437.

[170] C.B. Bidiville, A., K. Wasmer , R. Kraft, Diamond Wire-Sawn Silicon Wafers – From The Lab To The Cell Production, in: 24th Eur. Photovolt. Sol. Energy Conf. Exhib., 2009: pp. 1400–1405.

[171] K. Chen, Y. Liu, X. Wang, L. Zhang, X. Su, Novel texturing process for

diamond-wire-sawn single-crystalline silicon solar cell, Sol. Energy Mater. Sol. Cells. 133 (2015) 148–155. doi:10.1016/j.solmat.2014.11.016.

[172] A. Kumagai, Texturization using metal catalyst wet chemical etching for multicrystalline diamond wire sawn wafer, Sol. Energy Mater. Sol. Cells. 133 (2015) 216–222. doi:10.1016/j.solmat.2014.11.008.

[173] F. Cao, K. Chen, J. Zhang, X. Ye, J. Li, S. Zou, X. Su, Next-generation multi-crystalline silicon solar cells: Diamond-wire sawing, nano-texture and high efficiency, Sol. Energy Mater. Sol. Cells. 141 (2015) 132–138. doi:10.1016/j.solmat.2015.05.030.

[174] V. Blattmann, D. Trusheim, Hybrid Laser-Etching-Process for Wafer Texturing, Energy Procedia. 77 (2015) 766–773. doi:10.1016/j.egypro.2015.07.108.

[175] L. Xiao-mei, C. Wen-hao, L. Miao, Z. Lang, Texture for Diamond Wire Sawn Multicrystalline Silicon Wafers by a Vapor Etching Method, Acta Photonica Sin. 44 (2015) 116002. doi:10.3788/gzxb20154401.0116002.

[176] X. Ye, S. Zou, K. Chen, J. Li, J. Huang, F. Cao, X. Wang, L. Zhang, X.-F. Wang, M. Shen, X. Su, 18.45%-Efficient Multi-Crystalline Silicon Solar Cells with Novel Nanoscale Pseudo-Pyramid Texture, Adv. Funct. Mater. 24 (2014) 6708–6716. doi:10.1002/adfm.201401589.

CURRICULUM VITAE

PERSONAL INFORMATION

Surname, Name : Es, Fırat

Nationality : Turkish

Date and Place of Birth : 1 June 1985, Ankara

Work Adress: Center for Solar Energy Research and Applications, Department of Physics, Middle East Technical University, Ankara/TURKEY

Phone: +90 535 207 06 85

e-mail: esfirat@metu.edu.tr

EDUCATION

Degree	Institution	Year of Graduation
MS	METU Physics	2010
BS	METU Physics	2008
High School	Yıldırım Bayezid Anadolu	2003

WORK EXPERIENCE

Year	Place	Enrollment
2013- Present	GUNAM, METU	Research Assistant
2011-2013	GUNAM, METU	Scientific Project Expert
2009-2011	GUNAM, METU	Project Scholar
2009-2011	MEMS, METU	Researcher
2010-2011	TUBİTAK Space Tech. Inst.	Part Time Engineer
2009-2013	Turkish Standards Inst.	ISO Standards Translation

AWARDS AND SCHOLARSHIPS

2004-2005: High Honor Degree

2005-2006: Honor Degree

2006-2007: Honor Degree

2007-2008: High Honor Degree

2008-2010: TUBİTAK Scholarship for prosperous M.Sc. students

2010-2016: TUBİTAK Scholarship for prosperous Ph.D. students

FOREIGN LANGUAGES

Advanced English – TOEFL IBT Score: 107/120

PUBLICATIONS

Journal Articles

1. **Fırat Es**, Gülsen Baytemir, Mustafa Kulakci, and Raşit Turan, "Multi-c silicon solar cells with metal assisted nano-texturing using HNO_3 as hole injection agent", (PSS-RRL submitted)

2. **Fırat ES**, Gülsen BAYTEMİR, Mustafa KULAKCI, and Raşit TURAN, "Metal Assisted Nano Textured Solar Cells with SiO_2/Si_3N_4 Passivation", (SOLMAT submitted)

3. Sedat Bilgen, **Firat Es**, and Rasit Turan, "Comparison of mechanical and ultrasonic agitation methods for mono c-Si texturing", Phys. Status Solidi A., 1-6, (2016)

4. **Firat Es**, Mustafa Kulakci, Rasit Turan, "An Alternative Metal-Assisted Etching Route for Texturing Silicon Wafers for Solar Cell Applications", IEEE Journal of Photovoltaics, 1-7, (2016)

5. **Firat Es**, Emine Hande Ciftpinar, Olgu Demircioglu, Mete Gunoven, Mustafa Kulakci, Rasit Turan, "Performance of solar cells fabricated on black multicrystalline Si by nanowire decoration", Applied Surface Science, Volume 332, 266-271, (2015)

6. Mona Zolfaghari Borra, Seda Kayra Güllü, **Fırat Es**, Olgu Demircioğlu, Mete Günöven, Raşit Turan, Alpan Bek, "A Feasibility Study for Controlling Self-Organized Production of Plasmonic Enhancement Interfaces for Solar Cells", Applied Surface Science, 318, 43–50, (2014)

7. Irem Tanyeli, Hisham Nasser, **Firat Es**, Alpan Bek, Raşit Turan, "Effect of surface type on structural and optical properties of Ag nanoparticles formed by dewetting", Optics Express, Vol. 21, Issue S5, A798-A807 (2013)

8. Pantea Aurang, Olgu Demircioglu, **Fırat Es**, Raşit Turan, Hüsnü Emrah Unalan, "ZnO Nanorods as Antireflective Coatings for Industrial-Scale Single-Crystalline Silicon Solar Cells." Journal of the American Ceramic Society, 1-5, (2013)

9. Kulakci, M.; Es, F.; Ozdemir, B.; Unalan, H. E.; Turan, R.; , "Application of Si Nanowires Fabricated by Metal-Assisted Etching to Crystalline Si Solar Cells," Photovoltaics, IEEE Journal of , vol.3, no.1, 548-553, (2013)

133

Conference Proceedings

1. Olgu Demircioğlu, **Fırat Es**, Hande Çiftpınar, Akın Zeybek, Cahit Tuncer, and Raşit Turan,"Optimisation and design of PV modules for the application on bus roof-top and system integration for solar cooling." Phys. Status Solidi C., No:4, 159-162 (2016)

2. Yigit Ozan Aydin, **Firat Es**, Mona Zolfaghari, Alpan Bek "Solar Cell Processing by Nanosecond Pulsed Fiber Laser Amplifier", Science and Applications of Thin Films, Conference & Exhibition (SATF 2014), 93, (2015)

3. **Fırat Es**, Olgu Demircioglu, Mete Gunoven, Mustafa Kulakci, Husnu Emrah Unalan, Rasit Turan, "Performance of nanowire decorated mono- and multi-crystalline Si solar cells", Physica E: Low-dimensional Systems and Nanostructures, 51, 71-74 (2013)

4. **Firat Es**, Olgu Demircioglu, Mustafa Kulakci, Husnu Emrah Unalan and Rasit Turan, "Light management on industrial size c-Si solar cells by Si nanowires fabricated by metal-assisted etching", Proc. SPIE 8373, 837312 (2012)

Conference Presentations

1. Pantea Aurang, Doga Doganay, Sahin Coskun, **Firat Es**, Rasit Turan, Husnu Emrah Unalan, "Silver Nanowire Networks As Transparent Top Electrodes For Single Crystalline Silicon Solar Cells", EMRS Spring (2016)

2. Ior Pavlov, Tahir Çolakoğlu, **Fırat Es**, I. Gnilitskyi, Omer Ilday, Raşit Turan, Alpan Bek, "Periodic Surface Texturing by Nonlinear Laser Lithography for Enhanced Si Solar Cell Performance", EMRS Spring (2016)

3. Wisnu Hadibrata, **Firat Es**, Emine Hande Ciftpinar, Arman Ayan, Rasit Turan, Selcuk Yerci, "Thin Crystalline Silicon Solar Cells for Flexible Photovoltaics", EMRS Spring (2016)

4. Pantea Aurang, **Firat Es**, Rasit Turan, Husnu Emrah Unalan, "Nanowire Decorated Ultrathin Silicon Solar Cells", MRS (2015)

5. Hande Ciftpinar, **Fırat Es**, Olgu Demircioğlu, Mete Gunoven, and Rasit Turan, "Selective Emitter Solar Cell Fabrication via Single Step Doping", SiliconPV (2015)

6. **Fırat Es**, Emine Hande Çiftpınar, Gülsen Baytemir, Engin Özkol, Olgu Demircioğlu, Mete Günöven, Mustafa Kulakcı, and Raşit Turan, "Nano-Hole Texturing of Multi - Crystalline Silicon Solar Cells", 29th PVSEC (2014)

7. Olgu Demircioğlu, **Fırat Es**, Mustafa Kulakcı, Raşit Turan, "Electroless Nickel Plating For Buried Contact Solar Cells", SolarTR2 (2012)

8. **Fırat ES**, Mustafa Kulakcı, Mete Günöven, Raşit Turan, "Metal Assisted Texturing for Mono and Multi Crystalline Si Solar Cells" SiliconPV (2013)

9. Hande Çiftpınar, **Fırat Es**, İldar Salakhutdinov, Alpan Bek, Raşit Turan, "Plasmonic enhancement of solar cells by self-assembled silver nanoparticles" Nano TR9 (2013)

10. **Fırat Es**, Mustafa Kulakcı, Mete Günöven, Raşit Turan, "Optimization of Metal Assisted Texturing for Multi Crystalline Si Solar Cells" Solar Energy for World Peace conference, (2013)

11. Emine Hande Çiftpınar, **Fırat Es**, Mete Günöven, Raşit Turan, "Single Step Doping for Selective Emitter Crystalline Si Solar Cells" Solar Energy for World Peace conference, (2013)

12. Hisham Nasser, Engin Ozkol, Mete Gunoven, Fırat Es, Alpan Bek and Raşit Turan, "Influence of SiO_2 Underlying Spacer Layer on the Properties of Silver Nanoparticles for Potential Use in c-Si Solar Cells" 28th PVSEC (2013)

13. Pantea Aurang, Olgu Demircioglu, **Firat Es**, Caner Durucan, Rasit Turan, Husnu E. Unalan, "ZnO Nanorods as Antireflective Coatings for Industrial Scale Single Crystalline Silicon Solar Cells" MRS Fall (2013)

14. Mustafa Kulakcı, Fırat Es, Hande Çiftpınar, ''Metal Assisted Etching for Multi Crystalline Si Solar Cells' 27th PVSEC, (2012)

15. **Fırat Es**, Mustafa Kulakcı, Raşit Turan "Application of Si Nanowires to Mono and Multicrystalline Solar Cells", SolarTR-2 (2012)

16. Alpan Bek, İrem Tanyeli, Hisham Nasser, **Fırat Es**, Raşit Turan "Structural and optical properties of Ag nanoparticles formed by de-wetting on various substrates", SolarTR2 (2012)

17. Makbule Bilgen, **Fırat Es**, Mete Günöven, Raşit Turan, "Effect of Ag Nanoparticles Embedded in ZnO on the Performance of the n-type Solar Cells", SolarTR2 (2012)

18. Emine Hande Çiftpınar, Fırat Es, Olgu Demircioğlu, Raşit Turan, "A New Selective Emitter Technique Based On Single Step Doping For High Efficiency Crystalline Si Solar Cell", SolarTR2 (2012)

19. Irem Tanyeli, Hisham Nasser, **Firat Es**, Alpan Bek, Rasit Turan; 'Formation of and Light Scattering from Plasmonic Ag Nanoparticles on Solar Cell Thin Film Materials', EMRS, Spring (2012)

20. Hisham Nasser, Irem Tanyeli, **Fırat Es**, Alpan Bek, Raşit Turan, 'Plasmonic light scattering from Ag nanoparticles fabricated on ITO and ZnO thin films', Photovoltaic Technical Conference (2012)

21. Irem Tanyeli, **Fırat Es**, R. Turan "Effects of Dielectric Environment of Metal Nanoparticles on Plasmonic Scattering for Light Trapping In Solar Cells" NanoTR VII - 7th Nanoscience and Nanotechnology Conference (2011)

22. **Fırat Es**, Erdem Katı, Banu Kosif, Raşit Turan; 'Improvements of Surface Treatment for Multi Crystalline Si Solar Cells', 26th PVSEC (2011)

23. Mustafa Kulakcı, **Fırat Es**, Barış Özdemir, Emrah Ünalan, Raşit Turan, 'Application Si Nanowires Prepared by a Novel Etching Techniques to Standard Crystalline Silicon Solar Cells', 26th PVSEC (2011)

24. Olgu Demircioğlu, Fırat Es, Mustafa Kulakcı, Raşit Turan; 'Effects of Groove Geometry to the Efficiency of Buried Contact Crystalline Silicon Solar Cells' 26th PVSEC (2011)

25. İrem Tanyeli, **Fırat Es**, Raşit Turan; 'Effects of Dielectric environment of Metal Nanoparticles on Plasmonic Scattering for Light trapping in Silicon Solar Cells' 26th PVSEC (2011)

26. **Fırat ES**, Raşit Turan, Bilim Teknik, "Kristal Silisyum Güneş Gözeleri", June, 523, 52-53 (2011)

27. **Fırat ES**, "Fabrication And Characterization Of Single Crystalline Silicon Solar Cells", MS. Thesis, (2010)

Standards Translated and Published

1- TS EN ISO 11137-3 : Sterilization of health care products - Radiation - Part 1: Requirements for development, validation and routine control of a sterilization process for medical devices (ISO 11137-1:2006)

2- TS EN ISO 11137-3 : Sterilization of health care products - Radiation - Part 2: Establishing the sterilization dose (ISO 11137-2:2013)

3- TS EN ISO 11137-3 : Sterilization of health care products - Radiation - Part 3: Guidance on dosimetric aspects (ISO 11137-1:2006)

4- TS EN 60601-2-20 : Medical electrical equipment -Part 2-20: Particular requirements for the basic safety and essential performance of infant transport incubators (EN 60601-2-20)

5- TS EN ISO 9999 : Assistive products for persons with disability - Classification and terminology (EN ISO 9999:2011)